

**NASA  
Technical  
Paper  
3314**

June 1993

# Evaluation of Four Advanced Nozzle Concepts for Short Takeoff and Landing Performance

P. Frank Quinto,  
Guy T. Kemmerly,  
and John W. Paulson, Jr.

**NASA**

**NASA**  
**Technical**  
**Paper**  
**3314**

1993

**Evaluation of Four  
Advanced Nozzle Concepts  
for Short Takeoff and  
Landing Performance**

P. Frank Quinto,  
Guy T. Kemmerly,  
and John W. Paulson, Jr.  
*Langley Research Center*  
*Hampton, Virginia*

**NASA**

National Aeronautics and  
Space Administration  
Office of Management  
Scientific and Technical  
Information Program

## Abstract

*Four advanced nozzle concepts were tested on a canard-wing fighter in the Langley 14- by 22-Foot Subsonic Tunnel. The four vectoring-nozzle concepts were (1) an axisymmetric nozzle (AXI), (2) an asymmetric, load-balanced exhaust nozzle (ALBEN), (3) a low aspect ratio, single expansion ramp nozzle (LASERN), and (4) a high aspect ratio, single expansion ramp nozzle (HASERN). The investigation was conducted to determine the most suitable nozzle concept for short takeoff and landing (STOL) performance. The criterion for the best STOL performance was a takeoff ground roll of less than 1000 ft. At approach, the criteria were high lift and sufficient drag to maintain a glide slope of  $-3^\circ$  to  $-6^\circ$  with enough pitching-moment control from the canards. The test was performed at a dynamic pressure of 45 lb/ft<sup>2</sup> and an angle-of-attack range of  $0^\circ$  to  $20^\circ$ . The nozzle pressure ratio was varied from 1.0 to 4.3 at both dry power and afterburning nozzle configurations with nozzle vectoring to  $60^\circ$ . In addition, the model was tested in and out of ground effects. The ALBEN concept was the best of the four nozzle concepts tested for STOL performance.*

## Introduction

To counter the threats that the next generation of fighter airplanes will face, advanced technologies must be incorporated into new designs. One of these technologies will be advanced vectorable axisymmetric or asymmetric exhaust nozzles. In addition, these new technologies will increase survivability through enhanced fighter maneuverability and will facilitate short takeoff and landing (STOL) operations. STOL operations will be needed because bomb damage or other runway denial tactics by enemy forces could render sections of runway useless. Aircraft with STOL capability will have a distinct advantage because they can operate from sections of usable runway.

Government agencies (NASA and DoD) and industry (Grumman Aerospace Corp., Pratt & Whitney, and the GE Company) joined to conduct studies to define these advanced nozzle concepts. Several nozzle concepts have been developed, including axisymmetric and asymmetric arrangements. The nozzles were designed to meet a defined tactical mission profile and to integrate into an airplane configuration (refs. 1 and 2). From these proposed nozzle concepts, four were selected for wind-tunnel testing at high and low speeds. The results of the high-speed wind-tunnel testing on these nozzle concepts are presented in references 3 and 4, and the results of the low-speed wind-tunnel test are presented in this paper. The four vectoring-nozzle concepts were (1) an

axisymmetric nozzle (AXI), (2) an asymmetric, load-balanced exhaust nozzle (ALBEN), (3) a low aspect ratio, single expansion ramp nozzle (LASERN), and (4) a high aspect ratio, single expansion ramp nozzle (HASERN). The LASERN concept was developed by Pratt & Whitney; the other three concepts were developed by the GE Company.

These four nozzle concepts were tested on a common baseline fighter configuration developed by Grumman Aerospace Corp. under the Configuration Development of Advanced Fighters (CDAF) program, sponsored by the Air Force Wright Aeronautical Laboratories (AFWAL) as discussed in reference 5. The analysis of these designs at high speed indicated that asymmetric nozzles provide a better blend with the airframe than axisymmetric nozzles and exhibit favorable thrust-induced effects (ref. 3).

The low-speed wind-tunnel test was conducted in the Langley 14- by 22-Foot Subsonic Tunnel to evaluate which nozzle concepts would give the reference fighter configuration the best STOL performance. The objective for takeoff performance was to use the shortest runway distance within control limits. The longitudinal aerodynamic performance goals for the approach conditions were as follows: lift coefficients greater than or equal to 1.5, pitching-moment coefficient not to exceed  $-0.3$ , and lift and drag values necessary to maintain a glide slope of  $-3^\circ$  to  $-6^\circ$  (a lift-to-drag ratio of 19.081 to 9.514). The investigation used the 12.5-percent-scale fighter configuration

described in references 4 and 6. The nozzles were tested at both takeoff and landing conditions, at a nozzle pressure ratio of 1.0 to 4.3, and at vector angles from 0° to 60°. The angle of attack  $\alpha$  of the model was varied from 0° to 20° at a dynamic pressure of 45 lb/ft<sup>2</sup> with flap deflections of 0° and 20°. In addition, ground effects on longitudinal aerodynamics were evaluated at  $\alpha = 11^\circ$  with a model height to span ratio ranging from 0.12 to 1.44.

## Symbols

$a$	acceleration, ft/sec <sup>2</sup>
AFPO	ratio of static-thrust axial force to ambient pressure during nozzle calibration, $F_{A,s}/p_a$ , ft <sup>-2</sup>
$A_t/A_e$	ratio of nozzle throat area and nozzle exit area
$B$	model wing span, 55.112 in.
$\bar{c}$	mean aerodynamic chord, 21.125 in.
$C_A$	axial-force coefficient, $F_A/q_\infty S$
$C_{A,T}$	static-thrust axial-force coefficient, $[(F_{A,s}/p_a)p_\infty]/q_\infty S$
$C_{A,TR}$	thrust-removed axial-force coefficient, $C_A - C_{A,T}$
$C_D$	drag coefficient, $C_A \cos \alpha + C_N \sin \alpha$
$C_{D,TR}$	thrust-removed drag coefficient, $C_{A,TR} \cos \alpha + C_{N,TR} \sin \alpha$
$C_L$	lift coefficient, $C_N \cos \alpha - C_A \sin \alpha$
$C_{L,TR}$	thrust-removed lift coefficient, $C_{N,TR} \cos \alpha - C_{A,TR} \sin \alpha$
$C_m$	pitching-moment coefficient, $M_Y/q_\infty S \bar{c}$
$C_{m,T}$	static-thrust pitching-moment coefficient, $[(M_{Y,s}/p_a)p_\infty]/q_\infty S \bar{c}$
$C_{m,TR}$	thrust-removed pitching-moment coefficient, $C_m - C_{m,T}$
$C_N$	normal-force coefficient, $F_N/q_\infty S$
$C_{N,T}$	static-thrust normal-force coefficient, $[(F_{N,s}/p_a)p_\infty]/q_\infty S$
$C_{N,TR}$	thrust-removed normal-force coefficient, $C_N - C_{N,T}$
$C_T$	thrust coefficient, $F/q_\infty S$
$C_\mu$	ideal thrust coefficient, $F_I/q_\infty S$

$d$	ground-roll distance, ft
$F$	measured thrust, $\sqrt{(F_{A,s})^2 + (F_{N,s})^2}$ , lbf
$F_A$	axial force, lbf
$F_{A,s}$	static-thrust axial force, lbf
$F_I$	ideal thrust, $(wf/g)\sqrt{5\gamma_a RT_R(1 - NPR)^{(\gamma_a - 1)/\gamma_a}}$ , lbf
$F_N$	normal force, lbf
$F_{N,s}$	static-thrust normal force, lbf
$g$	acceleration due to gravity, 32.2 ft/sec <sup>2</sup>
$H/B$	ratio of model height to wing span
JANG	nozzle jet angle, $-\tan^{-1}(F_{N,s}/F_{A,s})$ , deg
$L/D$	lift-to-drag ratio, $C_L/C_D$
$M_Y$	pitching moment, ft-lb
$M_{Y,s}$	static-thrust pitching moment, ft-lb
NFPO	ratio of static-thrust normal force to ambient pressure during nozzle calibration, $F_{N,s}/p_a$ , ft <sup>-2</sup>
NPR	nozzle pressure ratio, $p_t/p_\infty$
$p_a$	ambient pressure, lbf/ft <sup>2</sup>
$p_t$	nozzle total pressure, lbf/ft <sup>2</sup>
$p_\infty$	free-stream static pressure, lbf/ft <sup>2</sup>
PMPO	ratio of static-thrust pitching moment to ambient pressure during nozzle calibration, $M_{Y,s}/p_a$ , ft <sup>-1</sup>
$q_\infty$	free-stream dynamic pressure, lbf/ft <sup>2</sup>
$R$	gas constant, 1716 ft <sup>2</sup> /sec <sup>2</sup> -°R
$S$	wing reference area, 7.03125 ft <sup>2</sup>
$T$	installed thrust, lbf
$T_R$	temperature of model high-pressure air, °R
$V$	velocity, knots
$W$	airplane takeoff weight, lb
$wf$	weight flow of high-pressure air to model, lb/sec
$\alpha$	angle of attack, deg
$\gamma$	flight path on glide slope angle, $-\tan^{-1}(C_L/C_D)$ , deg

$\gamma_a$	specific heat ratio, 1.4 for air
$\delta_f$	wing trailing-edge-flap deflection (positive value for trailing edge down), deg
$\delta_N$	nozzle geometric vector angle (positive value for nozzle vectored down), deg
$\eta$	thrust efficiency, $C_T/C_\mu$
$\eta'$	normalized thrust efficiency to ALBEN nozzle (table III)
$\mu$	friction coefficient
$\rho$	air density, slugs/ft <sup>3</sup>

#### Abbreviations:

AFWAL	Air Force Wright Aeronautical Laboratories
ALBEN	asymmetric load-balanced exhaust nozzle
AXI	axisymmetric nozzle
BL	butt-line station of full-size aircraft, in.
CDAF	Configuration Development of Advanced Fighters
DoD	Department of Defense
FS	fuselage station of full-scale aircraft, in.
HASERN	high aspect ratio, single expansion ramp nozzle
L	landing
LASERN	low aspect ratio, single expansion ramp nozzle
MRC	moment reference center
SERN	single expansion ramp nozzle
STOL	short takeoff and landing
T	takeoff
WL	waterline station of full-scale aircraft, in.

## Model Description

### Baseline Aircraft Configuration

A 12.5-percent-scale, close-coupled, canard-wing fighter model with two underwing, podded engine nacelles was used in the investigation, as shown in

figures 1-3. This fighter configuration was developed by Grumman Aerospace Corp. under the CDAF program, sponsored by AFWAL (ref. 5). The configuration was a fighter/penetrator airplane capable of supersonic flight, transonic maneuvering, and STOL operations. To accomplish these capabilities, the fighter incorporated a mission-adaptive main wing with a sweep angle of 57°, a supercritical airfoil, and variable camber and twist (refs. 1-6). A trailing-edge flap was fitted to the wing and tested at deflections of 0° and 20° (fig. 1).

The engines were in podded nacelles under the wing (figs. 1-3); this location permitted tests of a number of different nozzle concepts without radically changing the original fighter configuration. Also, the nozzle exhaust, near the wing trailing edge, produced beneficial thrust-induced effects (refs. 2 and 5). The wind-tunnel model, including the nozzle concepts, was modular in design for simplicity and interchangeability (fig. 3). Basic model geometry is shown in table I.

### Nozzle Concepts

The four nozzle concepts tested were (1) an axisymmetric nozzle, (2) an asymmetric, load-balanced exhaust nozzle, (3) a low aspect ratio, single expansion ramp nozzle, and (4) a high aspect ratio, single expansion ramp nozzle. Each nozzle concept was tested with an area ratio  $A_t/A_e$  appropriate for dry power and afterburning power. These two settings are referred to as the landing and takeoff nozzles, respectively, in this report. The total nozzle throat areas (left plus right sides) are presented in table II. In the following discussion, the letter after the nozzle vector angle (L or T) denotes either landing or takeoff nozzle setting. Sketches and photographs of the concepts are presented in figures 4 and 5; these concepts are briefly described below.

**Axisymmetric nozzle (AXI).** The axisymmetric nozzle (figs. 4 and 5(a)) was a convergent-divergent nozzle that used both throat area and nozzle area ratio control. During the test, the nozzle was vectored to 20° at either power setting (ref. 6).

**Asymmetric, load-balanced exhaust nozzle (ALBEN).** This configuration was a low aspect ratio, asymmetric nozzle that varied the throat area by rotating the lower ventral ramp. The upper expansion ramp provided area ratio control and thrust vectoring (figs. 4 and 5(b)). At thrust vector angles greater than 20°, the lower ventral ramp rotated with the upper expansion ramp. The ALBEN concept was designed to provide high thrust coefficients at high thrust vector angles. This nozzle concept was

tested with vector angles to  $50^\circ$  at landing and to  $30^\circ$  at takeoff (ref. 6).

**Low aspect ratio, single expansion ramp nozzle (LASERN).** This nozzle concept comprised seven components: two convergent flaps, two divergent flaps, an expansion ramp, and two external flaps (figs. 4 and 5(c)). The nozzle convergent flaps were centrally pivoted to balance pressure forces at all times. The aft portion of the convergent flaps controlled throat area and also acted as the pivot for the divergent flaps. The upper and lower divergent flaps provided high-vectoring performance at different flight conditions by varying the nozzle area ratio at constant vector angles. Subsonic turning was obtained by rotating the upper and lower divergent flaps to provide efficient thrust vectoring to  $60^\circ$  at landing and  $30^\circ$  at takeoff (ref. 6).

**High aspect ratio, single expansion ramp nozzle (HASERN).** For the HASERN concept, the throat area was controlled by rotating the lower ventral surface (figs. 4 and 5(d)). Area ratio control and thrust vectoring were achieved by rotating the upper expansion ramp. At vector angles greater than  $20^\circ$ , the nozzle changes from a single expansion ramp nozzle (SERN) with partial internal expansion to a convergent nozzle with an extended upper ramp. This nozzle concept was designed for efficient thrust vectoring from  $-20^\circ$  to  $55^\circ$  (ref. 6). Vectoring angles for this test were evaluated at both power settings.

#### Model Support and High-Pressure Air System

The model was mounted with a nonmetric vertical tail support connected to an air sting. This mounting arrangement minimized support system interference on the lower surface and aft end of the model, where the greatest thrust-induced effects were expected. The metric to nonmetric interface in the air sting was achieved with a coiled pipe system, which minimized any transfer of mechanical forces from the high-pressure air supply to the model balance. (See fig. 6.) The high-pressure air was used to simulate jet exhaust. High-pressure air was fed to each model nacelle through a common plenum, although no control valve was installed to vary the amount of flow to each nacelle.

#### Model Instrumentation

Forces and moments, including thrust forces, were measured with a Langley six-component strain-gauge balance. The air-line-balance combination was calibrated to determine the effects of bridging the balance with the air line. The accuracy of the balance

alone was 0.5 percent of full scale. When the balance was fully recalibrated with the air sting and plenum system, the accuracy decreased to 1.0 percent of full scale. This decrease in accuracy was due to added structure connected to the balance and the coil of the air sting.

An accelerometer mounted inside the model was used to measure the angle of attack. The nozzle total pressures for each nacelle were measured with total-pressure rakes (fig. 4(b)) joined with a single pressure transducer. In this test, the purpose was to obtain nozzle pressure rather than details of internal performance. The mass flow of high-pressure air was measured by a venturi attached to the air supply line outside the test chamber.

#### Test Conditions

This investigation was conducted in the Langley 14- by 22-Foot Subsonic Tunnel over an angle-of-attack range of  $0^\circ$  to  $20^\circ$  at sideslip and roll angles of  $0^\circ$ . The free-stream dynamic pressure was  $45 \text{ lbf/ft}^2$ , which corresponds to a Mach number of 0.17 and a Reynolds number of  $1.23 \times 10^6$  per foot. During the test, the nozzle pressure ratio was varied from 1.0 (jet off) to 4.3. Ground-effects testing was performed at  $\alpha = 11^\circ$  with an  $H/B$  range from 0.12 to 1.44. The nozzle vector angles were varied during the test.

#### Static Thrust Determination

Before the test, the air-line-balance combination was calibrated. The effects were then included in the balance interaction equations in the data-reduction program. Before the static testing, a sting pressure tare was determined. This tare removed loads imposed by the pressurization of the air supply system under power-on conditions. These loads were caused after the coiled air line inside the sting expanded when pressurized then pushed on the balance. The longitudinal forces and moments were plotted as a function of sting inlet pressure and curve fitted with the method of least squares. Thus, when testing with power, the correction for the pressurized air line was removed because sting inlet pressure was known.

The main goal of the static tests of each nozzle configuration was to obtain the thrust forces and moment to define the wind-on, power-on, thrust-removed aerodynamics. Each nozzle configuration was statically tested to determine the direct thrust forces and moment as a function of NPR. During the wind-on test at a particular NPR, the thrust of each nozzle configuration was determined then removed from the total longitudinal aerodynamic data to obtain thrust-removed data. The following steps present the procedure used:

1. The nozzle static thrust force and moment components ( $F_{A,s}$ ,  $F_{N,s}$ ,  $M_{Y,s}$ ) were divided by ambient barometric pressure  $p_a$  and faired as a function of NPR by a least squares curve fit (figs. 7-10).
2. During the wind-on, power-on test at a given NPR, static thrust force and moment components

could be determined from the curve-fit static data when the static components were scaled to the tunnel static-pressure conditions.

3. The components of direct-thrust force and moment coefficients could then be removed from the wind-on, power-on data to obtain thrust-removed coefficients.

## Presentation of Results

The total longitudinal aerodynamic characteristics, which include thrust effects at various NPR values and nozzle vector angles for all four nozzle concepts, are presented in figures 11-18. Figures 11, 13, 15, and 17 present the data with the wing flaps undeflected; figures 12, 14, 16, and 18 present the data with the wing flaps deflected 20°. In figures 11-18, the canard is undeflected.

	Figure
Effects of NPR on longitudinal aerodynamic characteristics of AXI concept with $\delta_f = 0^\circ$ :	
$\delta_N = 0^\circ\text{L}$ . . . . .	11(a)
$\delta_N = 20^\circ\text{L}$ . . . . .	11(b)
$\delta_N = 0^\circ\text{T}$ . . . . .	11(c)
$\delta_N = 20^\circ\text{T}$ . . . . .	11(d)
Effects of NPR on longitudinal aerodynamic characteristics of AXI concept with $\delta_f = 20^\circ$ :	
$\delta_N = 0^\circ\text{L}$ . . . . .	12(a)
$\delta_N = 20^\circ\text{L}$ . . . . .	12(b)
$\delta_N = 0^\circ\text{T}$ . . . . .	12(c)
$\delta_N = 20^\circ\text{T}$ . . . . .	12(d)
Effects of NPR on longitudinal aerodynamic characteristics of ALBEN concept with $\delta_f = 0^\circ$ :	
$\delta_N = 0^\circ\text{L}$ . . . . .	13(a)
$\delta_N = 20^\circ\text{L}$ . . . . .	13(b)
$\delta_N = 40^\circ\text{L}$ . . . . .	13(c)
$\delta_N = 50^\circ\text{L}$ . . . . .	13(d)
Effects of NPR on longitudinal aerodynamic characteristics of ALBEN concept with $\delta_f = 20^\circ$ :	
$\delta_N = 0^\circ\text{L}$ . . . . .	14(a)
$\delta_N = 20^\circ\text{L}$ . . . . .	14(b)
$\delta_N = 40^\circ\text{L}$ . . . . .	14(c)
$\delta_N = 50^\circ\text{L}$ . . . . .	14(d)
$\delta_N = 0^\circ\text{T}$ . . . . .	14(e)
$\delta_N = 20^\circ\text{T}$ . . . . .	14(f)
$\delta_N = 30^\circ\text{T}$ . . . . .	14(g)
Effects of NPR on longitudinal aerodynamic characteristics of LASERN concept with $\delta_f = 0^\circ$ :	
$\delta_N = 0^\circ\text{L}$ . . . . .	15(a)
$\delta_N = 20^\circ\text{L}$ . . . . .	15(b)
$\delta_N = 40^\circ\text{L}$ . . . . .	15(c)
$\delta_N = 60^\circ\text{L}$ . . . . .	15(d)
Effects of NPR on longitudinal aerodynamic characteristics of LASERN concept with $\delta_f = 20^\circ$ :	
$\delta_N = 0^\circ\text{L}$ . . . . .	16(a)
$\delta_N = 20^\circ\text{L}$ . . . . .	16(b)
$\delta_N = 40^\circ\text{L}$ . . . . .	16(c)

$\delta_N = 60^\circ\text{L}$ . . . . .	16(d)
$\delta_N = 0^\circ\text{T}$ . . . . .	16(e)
$\delta_N = 20^\circ\text{T}$ . . . . .	16(f)
$\delta_N = 30^\circ\text{T}$ . . . . .	16(g)
Effects of NPR on longitudinal aerodynamic characteristics of HASERN concept with $\delta_f = 0^\circ$ :	
$\delta_N = 0^\circ\text{L}$ . . . . .	17(a)
$\delta_N = 20^\circ\text{L}$ . . . . .	17(b)
$\delta_N = 40^\circ\text{L}$ . . . . .	17(c)
$\delta_N = 50^\circ\text{L}$ . . . . .	17(d)
Effects of NPR on longitudinal aerodynamic characteristics of HASERN concept with $\delta_f = 20^\circ$ :	
$\delta_N = 0^\circ\text{L}$ . . . . .	18(a)
$\delta_N = 20^\circ\text{L}$ . . . . .	18(b)
$\delta_N = 40^\circ\text{L}$ . . . . .	18(c)
$\delta_N = 50^\circ\text{L}$ . . . . .	18(d)
$\delta_N = 0^\circ\text{T}$ . . . . .	18(e)
$\delta_N = 20^\circ\text{T}$ . . . . .	18(f)
Thrust-removed, longitudinal aerodynamic characteristics at $\alpha = 14^\circ$ for various nozzle deflections as a function of NPR:	
AXI $\delta_f = 0^\circ$ . . . . .	19(a)
AXI $\delta_f = 20^\circ$ . . . . .	19(b)
ALBEN $\delta_f = 0^\circ$ . . . . .	20(a)
ALBEN $\delta_f = 20^\circ$ . . . . .	20(b)
LASERN $\delta_f = 0^\circ$ . . . . .	21(a)
LASERN $\delta_f = 20^\circ$ . . . . .	21(b)
HASERN $\delta_f = 0^\circ$ . . . . .	22(a)
HASERN $\delta_f = 20^\circ$ . . . . .	22(b)
Effects of nozzle vector concepts on longitudinal aerodynamic characteristics. NPR = 2.5, $\delta_N = 20^\circ\text{L}$ , and $\delta_f = 20^\circ$ :	
Takeoff power setting . . . . .	23(a)
Landing power setting . . . . .	23(b)
Typical control surface time history . . . . .	24
Takeoff distance for four nozzle concepts for 34 200-lb aircraft . . . . .	25
Takeoff distance for optimized profile at overweight conditions . . . . .	26
Suitable STOL approach candidates at $\delta_f = 20^\circ$ :	
AXI . . . . .	27
ALBEN . . . . .	28
LASERN . . . . .	29
HASERN . . . . .	30
Suitable STOL approach candidates at $\delta_f = 0^\circ$ . . . . .	
Best STOL approach nozzle candidates . . . . .	32
Longitudinal aerodynamic characteristics in ground effects for ALBEN concept at NPR = 1.0 and 3.5, and $\delta_N = 0^\circ\text{L}$ and $40^\circ\text{L}$ :	
$\delta_f = 0^\circ$ . . . . .	33
$\delta_f = 20^\circ$ . . . . .	34

## Discussion of Results

### Unpowered Aerodynamic Characteristics

The unvectored, unpowered, and undeflected wing-flap data are presented in figures 11(a), 13(a), 15(a), and 17(a). For all the nozzle concepts, the lift-curve slope shows an increase at an angle of attack of  $6^\circ$ . This increase in lift may be due to vortex lift on the wing upper surface. The drag data for all the concepts are very similar, as expected. However, with the HASERN concept the drag increases because of the slight cant in the nacelles to accommodate the nozzle concept into the aircraft. (See figs. 1 and 4(b).) Due to relaxed static stability, the pitching-moment curve shows the expected unstable slope. Figures 12(a), 14(a), 16(a), and 18(a) present the four nozzle concepts with a wing trailing-edge flap deflection of  $20^\circ$ . Throughout the angle-of-attack range, the expected lift and drag increase due to the wing flap deflection. Also, an additional lift increase due to the vortex on the wing upper surface starts at an angle of attack of about  $4^\circ$ . The earlier start of the lift increase may be due to the increased circulation caused by the deflected wing flap. Also, the pitching-moment values show the expected decrease due to trailing-edge flap deflection; this decrease is probably caused by the aft shift of the lift center past the moment reference center.

The unpowered, vectored nozzle functioned as a small deflected flap in all the vectored nozzle concepts, which caused a slight lift and drag increase as well as a slight pitching-moment decrease. These effects were similar to those for trailing-edge flaps when the nozzles were vectored.

### Powered Aerodynamic Characteristics

The effects of NPR for all the nozzle concepts are also presented in figures 11–18. As NPR is increased, the lift increases and the total drag decreases due to the increased thrust. The controls for the high-pressure air were coarse; at times a specific thrust value was hard to maintain. In some of the drag data (especially  $C_L$  versus  $C_D$ ), the data curves were not "smooth" because of the constant adjustment of the air station controls. The pitching-moment value increases as NPR is increased when the nozzle concepts are unvectored. When the nozzles are vectored, the pitching-moment values decrease with increased NPR. When the nozzle is vectored at  $20^\circ$ , the thrust vector passes near or through the moment reference center. The pitching-moment data for  $\delta_N = 20^\circ$  show very little change for AXI and ALBEN concepts. At vector angles greater than  $20^\circ$ , the ALBEN data show a substantial decrease in pitching moment with

increased NPR. The two SERN concepts (LASERN and HASERN) show a large decrease in the pitching moment from power off to power on. Only a slight decrease occurs as NPR is increased, an indication that the thrust vector passes near the reference center. The decrease in pitching moment at vector angles greater than  $20^\circ$  was larger than the decrease at  $20^\circ$ ; however, this decrease was never as large as that due to the change from power off to power on. Vectoring the nozzles causes a lift increase and a slight drag increase due to the altered direction of the thrust; this action increases the thrust in the normal direction and decreases it in the axial direction.

### Thrust-Induced Effects

In this report, the thrust-removed data are used to determine any thrust-induced effects from the four nozzle concepts. The main emphasis is on the thrust-induced lift from the effects of jet sheet and flow entrainment, with the associated induced pitching moment. Changes in the thrust-removed data from jet off (NPR = 1.0) to jet on (NPR > 1.0) indicate thrust-induced effects. An indication of thrust-induced lift is the increase in  $C_{L,TR}$  as the values of NPR become larger (ref. 7). Figures 19–22 present the thrust-removed lift and pitching-moment coefficients at an angle of attack of  $14^\circ$  for the four nozzle concepts at the landing power setting, with vectored and unvectored nozzles and with deflected and undeflected flaps. In figure 19, the values of  $C_{L,TR}$  are nearly constant as NPR increases, indicating little induced lift for the unvectored and vectored AXI nozzles. A slight increase in lift occurs from jet off to jet on, as shown in figure 19, particularly with the flap deflected and nozzles vectored. The unvectored, asymmetric nozzle concept shows a slight increase in thrust-removed lift from jet off to jet on. (See figs. 20–22.) The thrust-induced-lift increase from jet off to jet on is greater, but not at all NPR values. As the nozzle vector angle increases, thrust-induced lift becomes greater. Of the three asymmetric nozzle concepts, the HASERN concept shows the largest increase in thrust-induced lift because the higher aspect ratio nozzle (wider exit) influences a larger portion of the aircraft wing. This increase may also be due to flow entrainment near the nozzle. The data from reference 7 show that as NPR (or thrust coefficient) becomes larger, any further increase in  $C_{L,TR}$  is due to flow entrainment and additional circulation lift from the jet effect, which produce a substantial nose-down pitching moment. This effect is not as pronounced in the other two asymmetric concepts; for the ALBEN and LASERN concepts, only a slight nose-down pitching moment from jet off to jet on occurs.

## Comparison of Nozzle Concepts

Figure 23 presents the longitudinal aerodynamic characteristics of the four nozzle concepts at  $\delta_N = 20^\circ$ ,  $\delta_f = 20^\circ$ , and  $\text{NPR} = 2.5$  for both takeoff and landing nozzle settings. The difference in the longitudinal aerodynamic data among the four nozzle concepts is small; the AXI nozzle has the lowest lift of the four concepts at both power settings. When the nozzle concepts are at the takeoff power setting, the LASERN produces the highest thrust values because the throat area is much larger than the other nozzles at takeoff power. (See table II.) The lift does not produce noticeable nose-down pitching moment because of the  $\delta_N$  value ( $\delta_N = 20^\circ$ ). The HASERN concept produces more noticeable nose-down pitching moment because of higher aft loading on the wing from the jet entrainment effects discussed previously. This flow entrainment also produces the higher lift at the landing power setting than the other nozzle concepts. Excluding the larger thrust differential for the LASERN, the four concepts show little difference in drag.

## STOL Performance Comparisons

To evaluate whether the four nozzle concepts improve the takeoff and landing performance of an advanced fighter aircraft, the data from this investigation are used to predict takeoff ground rolls and approach flight conditions. These results are then compared in order to determine the best airframe and nozzle configuration, based on minimum takeoff length and a trimmed, high-lift approach condition. In the takeoff evaluation, the nozzle is set at takeoff power; for the approach evaluation, the nozzle is set at landing power. The following discussion describes the takeoff comparison first, then addresses the approach comparison.

### Takeoff Comparison

**Suitability for takeoff.** The fighter aircraft configuration has an estimated design takeoff gross weight of 34 200 lb, a wing loading of 76 lbf/ft<sup>2</sup>, and a thrust-to-weight ratio of 0.85. This thrust level (29 000 lb) is derived from reference 5 for installed engines with an undeflected ALBEN. The installed thrust  $T$  is scaled for the other nozzle types and deflections, based on the relative efficiencies determined during the static investigations of the nozzle, as indicated in table III. The thrust efficiency  $\eta$  in table III is based on the ratio of wind-on ideal thrust and static-thrust coefficients at  $\text{NPR} = 2.5$  at the takeoff power setting. The ideal thrust coefficient is based on weight flow to the nozzles and flow temperature,

and the static-thrust coefficient is based on the static-thrust data.

The data from this investigation are used to predict the takeoff performance of an advanced fighter configuration equipped with each of the four nozzle concepts. Criteria for a successful takeoff are as follows: at liftoff, the lift must be greater than the weight; the acceleration must be sufficient to continue flying; and the pitching moment must be small enough to be trimmed ( $C_m$  not to exceed  $-0.3$ ) with the high-lift blown canard discussed in references 8 and 9. This canard concept uses a Krueger leading-edge flap and a trailing-edge flap equipped with boundary-layer blowing. This analysis uses the thrust-removed data from the wind-tunnel investigation, which included any induced aerodynamics created by the nozzle exhaust. Longitudinal aerodynamic coefficients for certain configurations not actually tested (such as nozzle vector angles) are computed by linear interpolation between the available data, based on angle of attack, nozzle deflection angle, and flap deflection angle. Control actuation rates are not defined for this fighter aircraft, so they are assumed; the values are  $10^\circ/\text{sec}$  pitch rate of the aircraft,  $10^\circ/\text{sec}$  flap deflection rate, and  $30^\circ/\text{sec}$  nozzle deflection rate.

A computer program incorporated all these data in a stepwise integration in which velocity was incremented by 0.2 knot until lift was greater than weight. The governing equation for acceleration of the aircraft is presented below:

$$\text{Acceleration} = \text{Thrust} - \text{Drag} - \frac{\text{Friction}}{\text{Mass}}$$

$$a = \frac{g}{W} \left\{ T\eta' \cos(\alpha + \delta_N) - \frac{1}{2} C_{D,TR} \rho V^2 S - \mu \right. \\ \left. \times \left[ W - \frac{1}{2} C_{L,TR} \rho V^2 S - T\eta' \sin(\alpha + \delta_N) \right] \right\}$$

From the acceleration and the known velocity, computations were made of the incremental distances and times required to change the aircraft airspeed by 0.2 knot. These increments were then summed to compute ground-roll distance and time. At all angles of attack greater than  $0^\circ$ , pitching moment was checked to assure that the value was within the control power of the high-lift blown canard (refs. 8 and 9). When lift exceeded the aircraft weight, takeoff was assumed at that point; then acceleration was checked to assure that the aircraft could continue to climb.

The following takeoff profiles were investigated:

**Conventional profile:** The flaps were deflected before the ground roll began. The aircraft accelerated to the precomputed minimum takeoff velocity, began rotation (to a maximum of  $11^\circ$ , based on the takeoff angle of a conventional fighter), and lifted off at some velocity greater than minimum takeoff velocity. No nozzle deflection was used in this profile, as shown in figure 24(a).

**Optimized profile:** All control deflections were initiated such that ground roll was minimal. Ideally, the aircraft would begin control deflections such that all reached the maximum deflection at the same time the aircraft reached the precomputed minimum takeoff velocity. In this case, the aircraft would actually lift off at minimum takeoff velocity. A typical control time history is presented in figure 24(b).

**Best nozzle concept.** Figure 25 shows the four nozzle concepts with the two takeoff profile cases at a full-scale aircraft gross weight of 34 200 lb. The conventional takeoff distances are between 910 and 1030 ft. In the optimized-takeoff profile, the takeoff distances are reduced by 50 to 60 percent (380 to 470 ft) of the conventional profile. The asymmetric nozzles that vectored to  $30^\circ$  (ALBEN and LASERN) have the shortest takeoff distances: less than 400 ft in the optimized profile. The ALBEN concept has the shortest takeoff distance (381 ft) with the optimized profile.

Ground rolls were also predicted for a number of overload cases to 50 000 lb gross weight. The predictions were normalized to the ALBEN configuration because it was determined to be the best nozzle at design gross weight. (See fig. 26.) At all takeoff gross weights, the LASERN and ALBEN configurations differ by a constant percentage because of the increased  $\eta'$  value of the ALBEN over that of the LASERN configurations. The HASERN and AXI configurations have similar trends; both are worse than the other two nozzles at low weights because both can vector only  $20^\circ$  rather than  $30^\circ$ .

The HASERN and AXI configurations are closer to that of the ALBEN at higher takeoff gross weights because a larger percentage of the ground roll is used to accelerate to the higher required takeoff velocities; therefore, nozzle vector capability and control sequencing become less significant. These occurrences are most apparent in the maximum overload cases in which the HASERN ( $20^\circ$  max) outperforms the ALBEN configuration ( $30^\circ$  max) because at  $\delta_N = 0^\circ$  the  $\eta'$  value for the HASERN is 1 percent higher than that for the ALBEN concept.

From this analysis, integration of the ALBEN configuration into the advanced fighter aircraft would give the best takeoff performance at all but the highest gross weight conditions.

### Approach Comparison

**Suitability for approach.** To maintain a stabilized flight path for a STOL approach, a configuration must generate high lift at slow speeds with sufficient drag to provide the required glide slope, in this case about  $-3^\circ$  to  $-6^\circ$  ( $L/D = 19.081$  to  $9.514$ ) with an angle of attack of about  $14^\circ$  (ref. 8). Because thrust reversing will be required at or near touchdown for minimum ground rolls, the engines are assumed to be at landing power settings during approach to eliminate spool-up time when reverse thrust is selected on the ground; thus, thrust vectoring or spoiling will be necessary to achieve the proper  $L/D$ . However, spoiling does not generate high lift, and vectoring while generating high lift can drive a configuration out of trim. In a previous investigation (refs. 8 and 9), a high-lift blown canard was used to trim a similar fighter configuration with  $\delta_N = 40^\circ$  and landing power setting. From these results, the minimum pitching-moment coefficient when the aircraft is trimmed is about  $-0.3$ . In the following discussion, therefore, any configuration that generated  $C_m \leq -0.3$  was not considered viable. Note that this analysis is for approach flight condition, not for the landing ground roll. Because these nozzle concepts were not tested with reverse thrust, the ground-roll predictions would not indicate relative performance in reducing ground-roll distances for each nozzle.

To assess the STOL approach capabilities of the four nozzle configurations on the advanced fighter, the longitudinal aerodynamics for several nozzle vector angles with  $\delta_f = 20^\circ$  and at the landing power setting ( $NPR = 2.5$ ) are presented in figures 27-30; figure 31 shows nozzle configurations at  $\delta_f = 0^\circ$ . Lines of constant glide slope of  $-3^\circ$  to  $-6^\circ$  are included in figures 27-31. Also in these figures, the longitudinal aerodynamic data points at an angle of attack of  $14^\circ$  are presented as solid symbols to indicate STOL approach angle of attack. The data in figures 27-30 indicate that the axisymmetric nozzle configuration as well as the other nozzles at  $\delta_N = 20^\circ$  has excessive thrust (when the angle of attack is  $14^\circ$ , the solid symbols are not within the glide slope lines). Because the axisymmetric nozzle vectoring is limited to  $20^\circ$ , the axisymmetric configuration is not a viable STOL nozzle concept.

Because the vectoring angle is increased, the asymmetric nozzle concept generates a configuration  $L/D$  such that a reasonable approach glide slope is

possible at about an angle of attack of  $14^\circ$ . Therefore, the ALBEN, LASERN, and HASERN configurations are all possible candidates for STOL operations. With the combination of nozzle vectoring and trailing-edge flap deflection, each concept has at least one configuration that nearly meets the STOL requirements. Two nozzle configurations meet the STOL approach glide slope angle at  $\alpha \approx 14^\circ$  and  $\delta_f = 20^\circ$ : the ALBEN with  $\delta_N = 50^\circ$  and the HASERN with  $\delta_N = 40^\circ$ . In addition, two configurations at  $\delta_f = 0^\circ$  are possible candidates, as shown in figure 31: the LASERN with  $\delta_N = 60^\circ$  and the HASERN with  $\delta_N = 40^\circ$ . (The LASERN configuration is not as desirable because it has a slightly steeper glide slope angle than required.)

**Best candidates.** The longitudinal aerodynamic data for the six candidate nozzle configurations at NPR = 2.5 are presented in figure 32. The two configurations that had undeflected trailing-edge flaps (LASERN with  $\delta_N = 60^\circ$  and HASERN with  $\delta_N = 40^\circ$ ) demonstrated the lowest lift values of the six configurations, as expected. The LASERN configuration, with  $\delta_N = 60^\circ$ , had the highest total drag because of a higher vector angle that reduced the thrust component in the axial direction. The high drag and low lift caused this configuration to have a slightly steeper glide slope angle than the other configurations as well as a higher approach speed. The HASERN configuration at  $\delta_N = 40^\circ$  and  $\delta_f = 20^\circ$  had the largest nose-down pitching moment because the wing trailing edge was highly loaded. At an angle of attack of about  $14^\circ$ , the pitching-moment coefficient is near  $-0.3$ , the limit of the blown high-lift canard to trim the aircraft.

The nozzle concepts that produced the highest lift ( $C_L \approx 1.95$ ) and appropriate  $L/D$  for approach glide slopes were the ALBEN at  $\delta_N = 50^\circ$  with  $\delta_f = 20^\circ$  and the HASERN at  $\delta_N = 40^\circ$  with  $\delta_f = 20^\circ$ . All the asymmetric configurations generated high lift ( $C_L > 1.5$ ) and at  $\alpha = 14^\circ$  were basically within the limit of  $C_m > -0.3$ , so that trim could be achieved. However, the ALBEN configuration demonstrated the smallest pitching-moment value ( $C_m = -0.2$ ) and did not use all the available control power from the canard to maintain trim. This control margin is needed to flare the aircraft before touchdown. Because this nozzle generated high lift with a good margin of  $C_m$  remaining after trim, the ALBEN appears to be the best nozzle and airframe configuration for approach. This result, coupled with the takeoff results, indicated that the best nozzle for STOL performance for this fighter concept would be the ALBEN configuration.

**Ground effects.** As an airplane approaches the runway, ground effects can change its aerodynamic characteristics. To assess whether ground effects might adversely affect the approach aerodynamics, tests were conducted for the ALBEN concept at  $\alpha = 11^\circ$  for  $\delta_N = 0^\circ$  and  $40^\circ$  with  $\delta_f = 0^\circ$  (fig. 33) and  $20^\circ$  (fig. 34). Due to the model support restrictions,  $\alpha = 11^\circ$  was used instead of  $14^\circ$  to give satisfactory variation in  $H/B$  values. At touchdown, the  $H/B$  value is 0.19 for  $\alpha = 11^\circ$  and 0.18 for  $\alpha = 0^\circ$ . With the wing trailing-edge flap undeflected, the lift coefficient has a slight increase of about 0.1 to 0.2 with decreasing  $H/B$  when the nozzle changes from unpowered to powered (NPR = 1.0 and 3.5), regardless of nozzle vector angle (fig. 33). The lift increase is less when  $\delta_f = 20^\circ$  (fig. 34) for both NPR values and both nozzle vector angles. The drag in figures 33 and 34 shows little change as the model approaches the ground, and the pitching moment changes little at NPR = 1.0 for vectored and unvectored nozzles as  $H/B$  values decrease (fig. 33). With NPR = 3.5,  $\delta_f = 0^\circ$ , and at both nozzle vector angles,  $C_m$  (nose-down moment) decreases as the model descends toward the ground. At  $\delta_f = 20^\circ$  and NPR = 3.5, the opposite occurs; as  $H/B$  values decrease, the  $C_m$  values increase (nose-up moment). The slight change in longitudinal aerodynamic values when the trailing-edge flap is deflected is not considered significant during approach. This change in values does not alter the conclusion that the ALBEN concept offers the best STOL performance.

## Conclusions

A wind-tunnel investigation was conducted in the 14- by 22-Foot Subsonic Tunnel to determine the most suitable advanced nozzle concept for short takeoff and landing (STOL) performance. Four vectoring-nozzle concepts were tested: (1) an axisymmetric nozzle (AXI), (2) an asymmetric, load-balanced exhaust nozzle (ALBEN), (3) a low aspect ratio, single expansion ramp nozzle (LASERN) and (4) a high aspect ratio, single expansion ramp nozzle (HASERN). The nozzles were mounted on an advanced canard-wing fighter with underwing nacelles. The nozzles were tested at nozzle pressure ratios (NPR) of 1.0 to 4.3 at both takeoff power and landing power nozzle configurations. These tests were conducted at a dynamic pressure of 45 lbf/ft<sup>2</sup> over an angle-of-attack range from  $0^\circ$  to  $20^\circ$ . The nozzles were vectored to  $60^\circ$  with the wing trailing-edge flap either undeflected or at  $20^\circ$ . The results of the investigation yielded the following conclusions:

1. For the shortest takeoff distance, the best deflection schedule of the trailing-edge flap and nozzle

vector is when both reach maximum deflection at the same time. The ALBEN concept attained the shortest takeoff distances even with overload conditions.

2. The HASERN concept developed the highest thrust-induced effects of the four concepts because the high aspect ratio nozzle affected a larger portion of the wing.
3. The best concept for a STOL approach was the ALBEN. This concept generated high lift and proper lift-to-drag ratio  $L/D$  for a glide slope angle of  $-3^\circ$  to  $-6^\circ$  without exceeding the pitching-moment guideline.
4. The HASERN concept was suitable for STOL approaches and in some parameters better than the ALBEN concept. The only drawback was the large nose-down moment generated when the nozzle was vectored past  $20^\circ$ .
5. As the model approached the ground, there was a slight increase in lift and a change in pitching-moment coefficient  $C_m$  from nose-down to nose-up moment as the trailing-edge flap was deflected. These changes were not considered detrimental during approach for a STOL landing.

NASA Langley Research Center  
Hampton, VA 23681-0001  
March 30, 1993

## References

1. Doonan, J. G.; and Schnell, W. C.: *Test Report, Phase I—Wind Tunnel Program, Advanced Exhaust Nozzle Concepts for Short Takeoff and Landing (STOL) and Survivability*. PXP-001-60 (Contract F33615-79-C-3009), Grumman Aerospace Corp., June 15, 1982.
2. Grumman Aerospace Corp.: *Phase I Interim Report, Volume I—STOL, Advanced Exhaust Nozzle Concepts for Short Takeoff and Landing (STOL) and Survivability*. PXP-001-64 (Contract F33615-79-C-3009), May 1983.
3. Doonan, J. G.; Callahan, C. J.; and Bowers, D. L.: *A High Speed Wind Tunnel Test Evaluation of STOL Dedicated Advanced Exhaust Nozzle Concepts*. AIAA-83-1225, June 1983.
4. Doonan, J. G.; and Suapengo, J. R.: *Test Report, Phase II—Wind Tunnel Program High Speed Test Reports, Advanced Exhaust Nozzle Concepts for Short Takeoff and Landing (STOL) and Survivability*. Grumman Aerospace Corp., Dec. 1983.
5. Bavitz, P. C.; et al.: *Configuration Development of Advanced Fighters—Volume 1, Executive Summary*. AFWAL-TR-80-3142, Vol. 1, U.S. Air Force, Nov. 1980.
6. Doonan, J. G.: *Test Report, Phase II—Wind Tunnel Program Low Speed Test Results, Advanced Exhaust Nozzle Concepts for Short Takeoff and Landing (STOL) and Survivability*. PXP-001-72 (Contract F33615-79-C-3009), Grumman Aerospace Corp., July 1984.
7. Quinto, P. Frank; and Paulson, John W., Jr.: *Thrust-Induced Effects on Subsonic Longitudinal Aerodynamic Characteristics of a Vectored-Engine-Over-Wing Configuration*. NASA TP-2228, 1983.
8. Quinto, P. Frank; Paulson, John W., Jr.; and Gatlin, Gregory M.: *Investigation of a High-Lift Blown Canard for Longitudinal Trim on a Thrust-Vectoring Fighter Configuration*. NASA TP-2775, 1987.
9. Paulson, J. W., Jr.; Gatlin, G. M.; Quinto, P. F.; and Banks, D. W.: *Trimming High Lift for STOL Fighters*. AIAA-83-0168, Jan. 1983.

Table I. Basic Model Geometry

Wing:	
Area, ft <sup>2</sup> . . . . .	7.031
Span, in. . . . .	55.112
Reference chord, in. . . . .	21.125
Aspect ratio . . . . .	3.000
Root chord, in. . . . .	30.625
Tip chord, in. . . . .	6.125
Leading-edge sweep, deg . . . . .	57.000
Trailing-edge sweep, deg:	
Inboard (BL 0.0 to 120.0) . . . . .	11.367
Outboard (BL 120 to 220.448) . . . . .	31.050
Moment reference center, in. . . . .	FS 570
Airfoil section . . . . .	Supercritical
Canard:	
Exposed area, ft <sup>2</sup> . . . . .	0.624
Semispan (exposed), in. . . . .	11.136
Aspect ratio (exposed) . . . . .	1.38
Root chord, in. . . . .	13.000
Tip chord, in. . . . .	3.125
Leading-edge sweep, deg . . . . .	52.895
Airfoil section . . . . .	4-percent biconvex

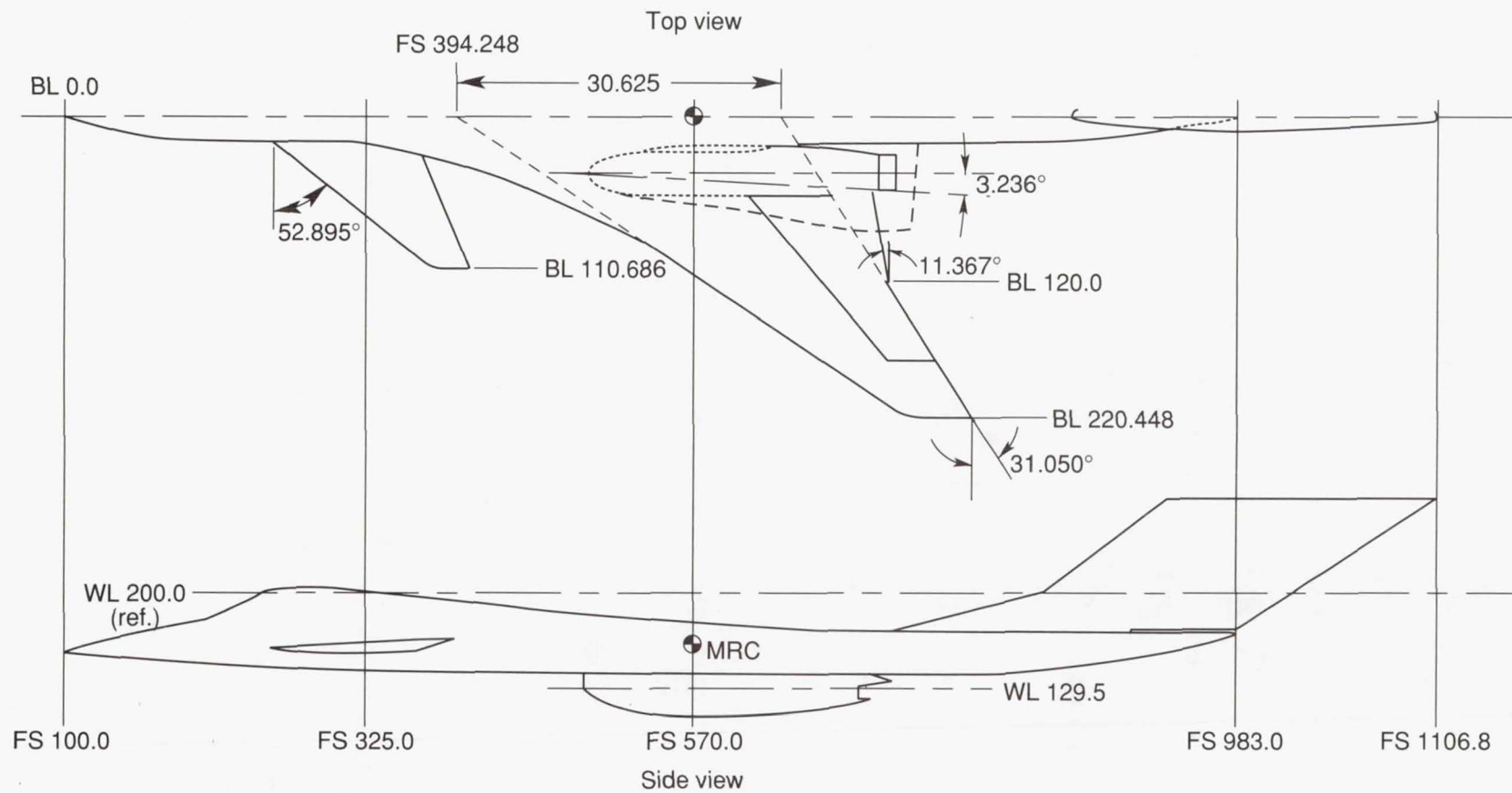
Table II. Total Nozzle Throat Areas for Four Nozzle Concepts

Nozzle vector angle	Nozzle throat area, in <sup>2</sup>			
	AXI	ALBEN	LASERN	HASERN
0°L	6.306	6.302	6.404	5.776
20°L	6.296	6.302	6.313	5.513
40°L		6.302	6.425	5.878
50°L		6.302		5.988
60°L			6.400	
0°T	8.472	8.44	11.086	7.911
20°T	8.464	8.44	11.260	7.787
30°T		8.44	11.277	

Table III. Installed Scaled-Thrust Values at NPR = 2.5 for Takeoff Performance Evaluation

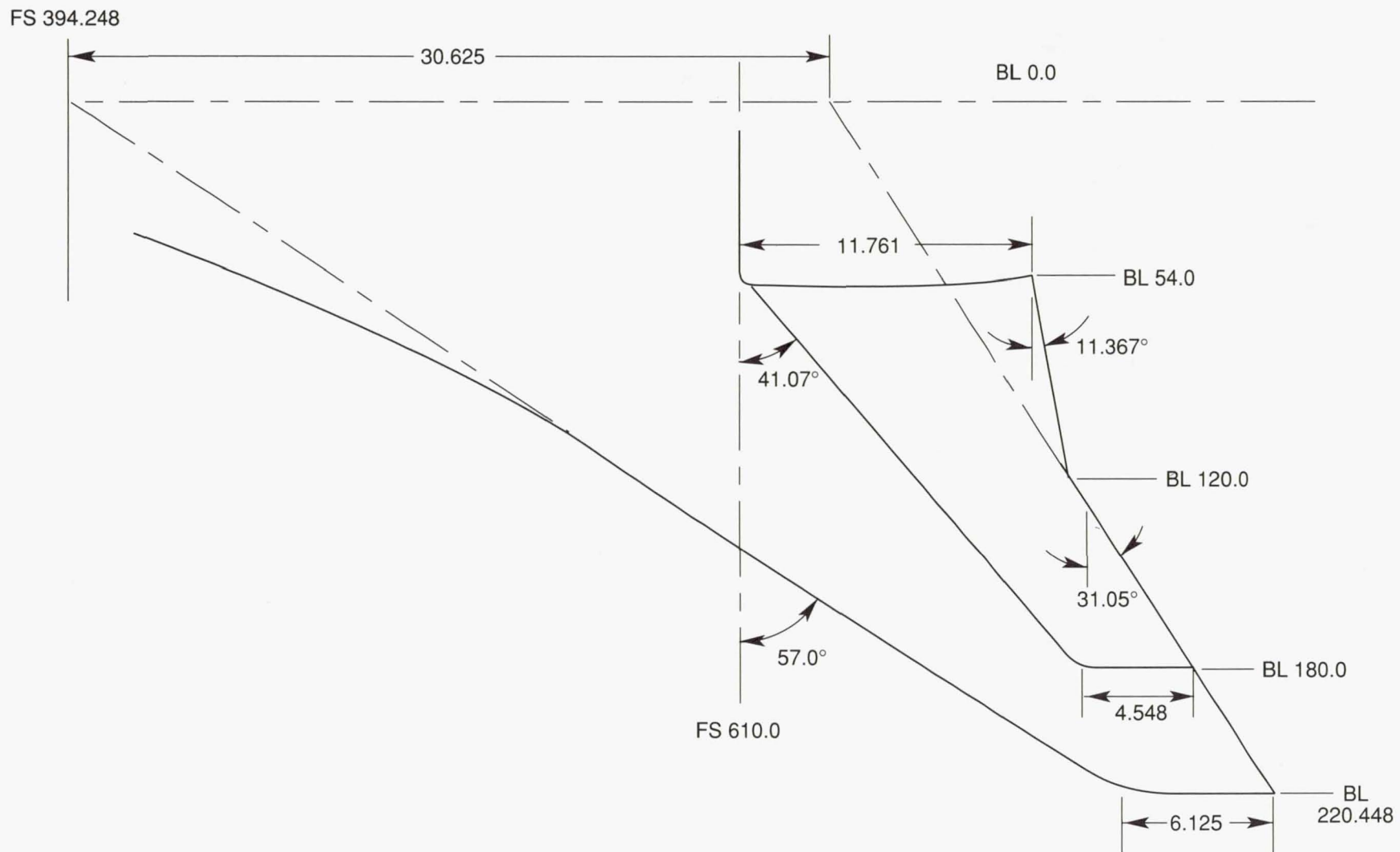
Nozzle type	$\eta$	$\eta'$	Scaled-thrust value
AXI			
0°T	0.98	1.0208	29 603
20°T	.98	1.0208	29 603
ALBEN			
0°T	0.96	<sup>a</sup> 1.0000	29 000
20°T	.98	1.0208	29 603
30°T	.96	1.0000	29 000
LASERN			
0°T	0.94	0.9792	28 396
20°T	.95	.9896	28 698
30°T	.95	.9896	28 678
HASERN			
0°T	0.97	1.0104	29 302
20°T	.95	.9896	28 679

<sup>a</sup>Thrust efficiencies  $\eta$  were normalized to unvectored ALBEN takeoff nozzle.



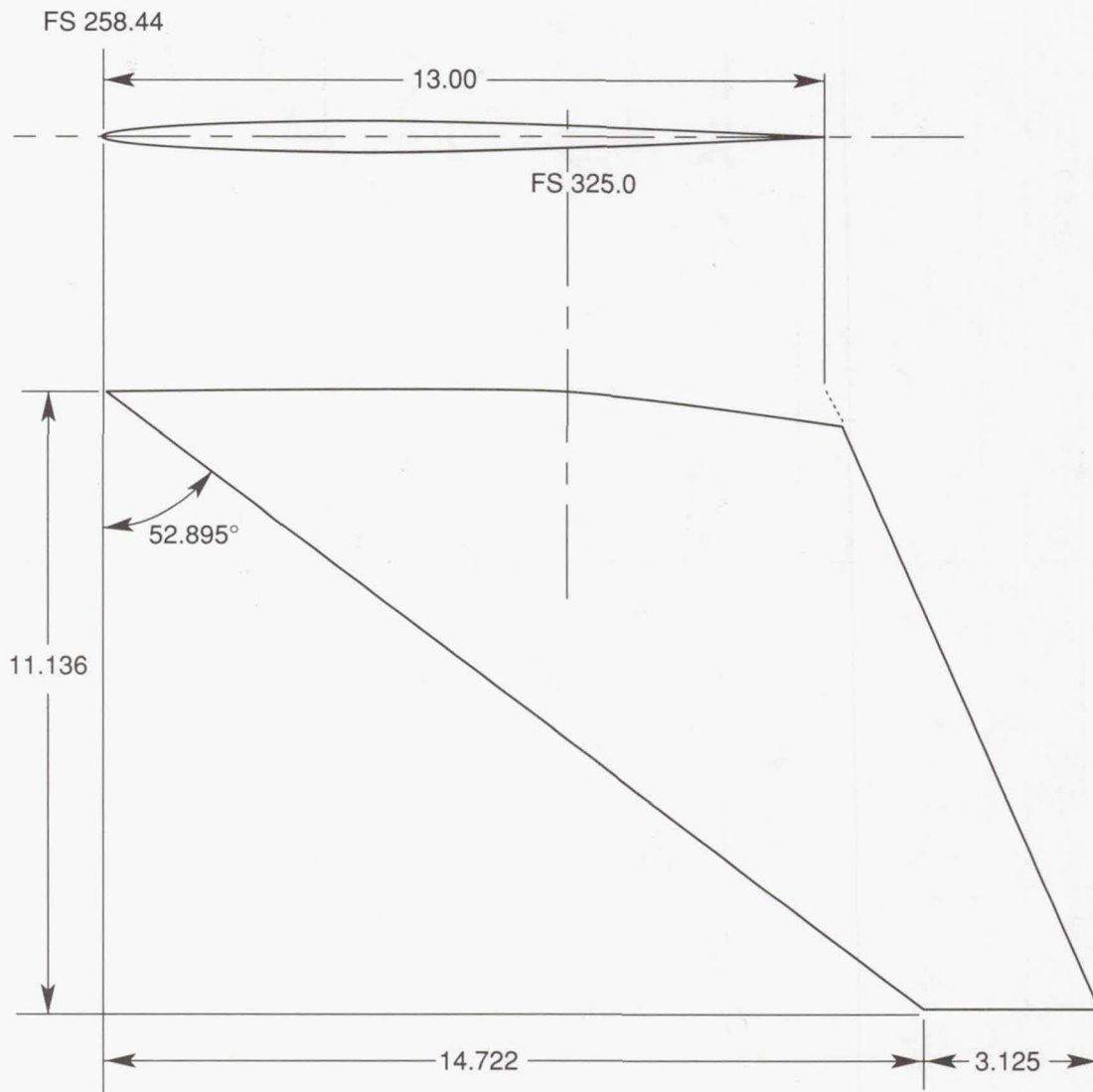
(a) Geometry of wind-tunnel model.

Figure 1. Model geometry for tests in 14- by 22-Foot Subsonic Tunnel. All linear dimensions are in inches.



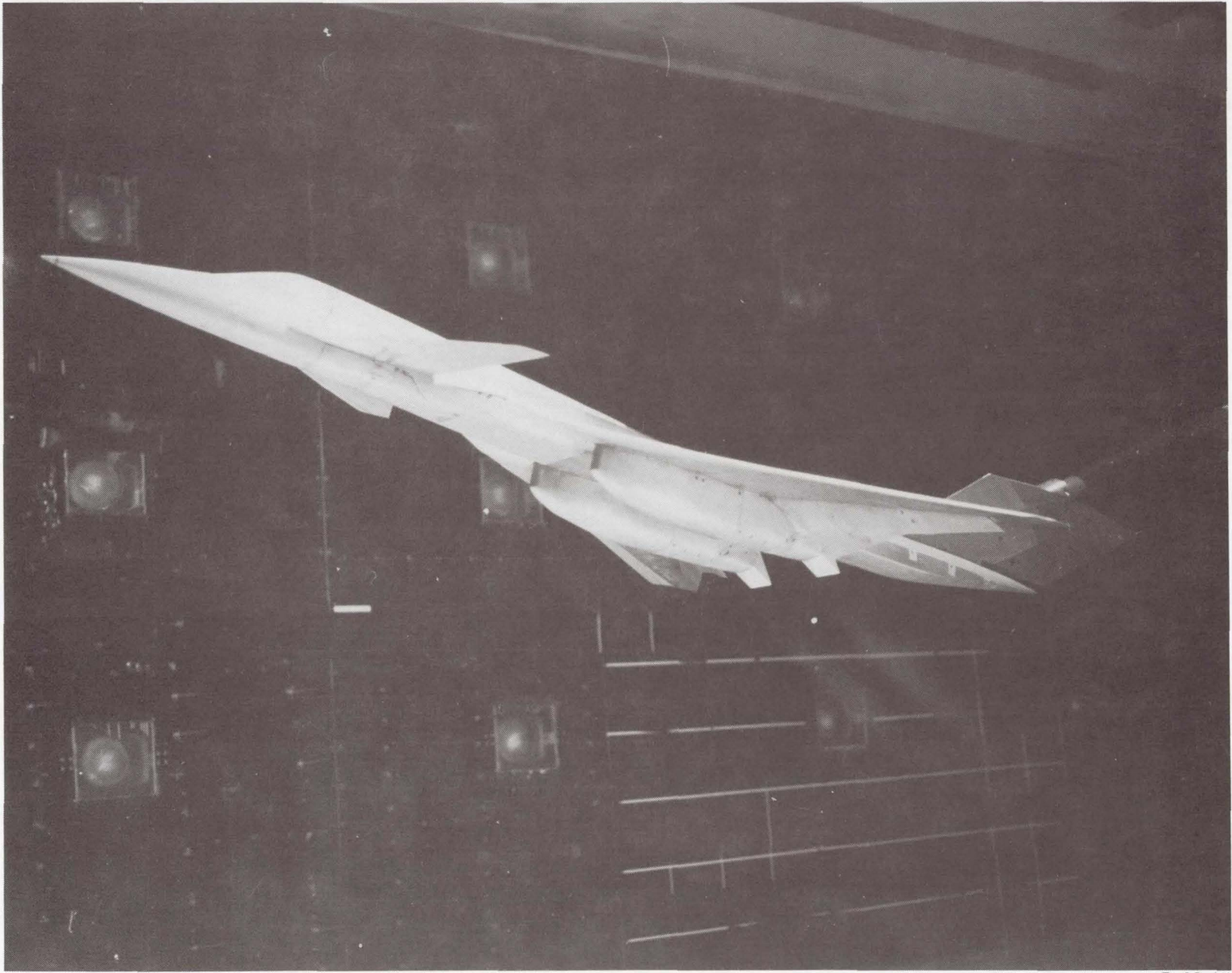
(b) Wing geometry.

Figure 1. Continued.



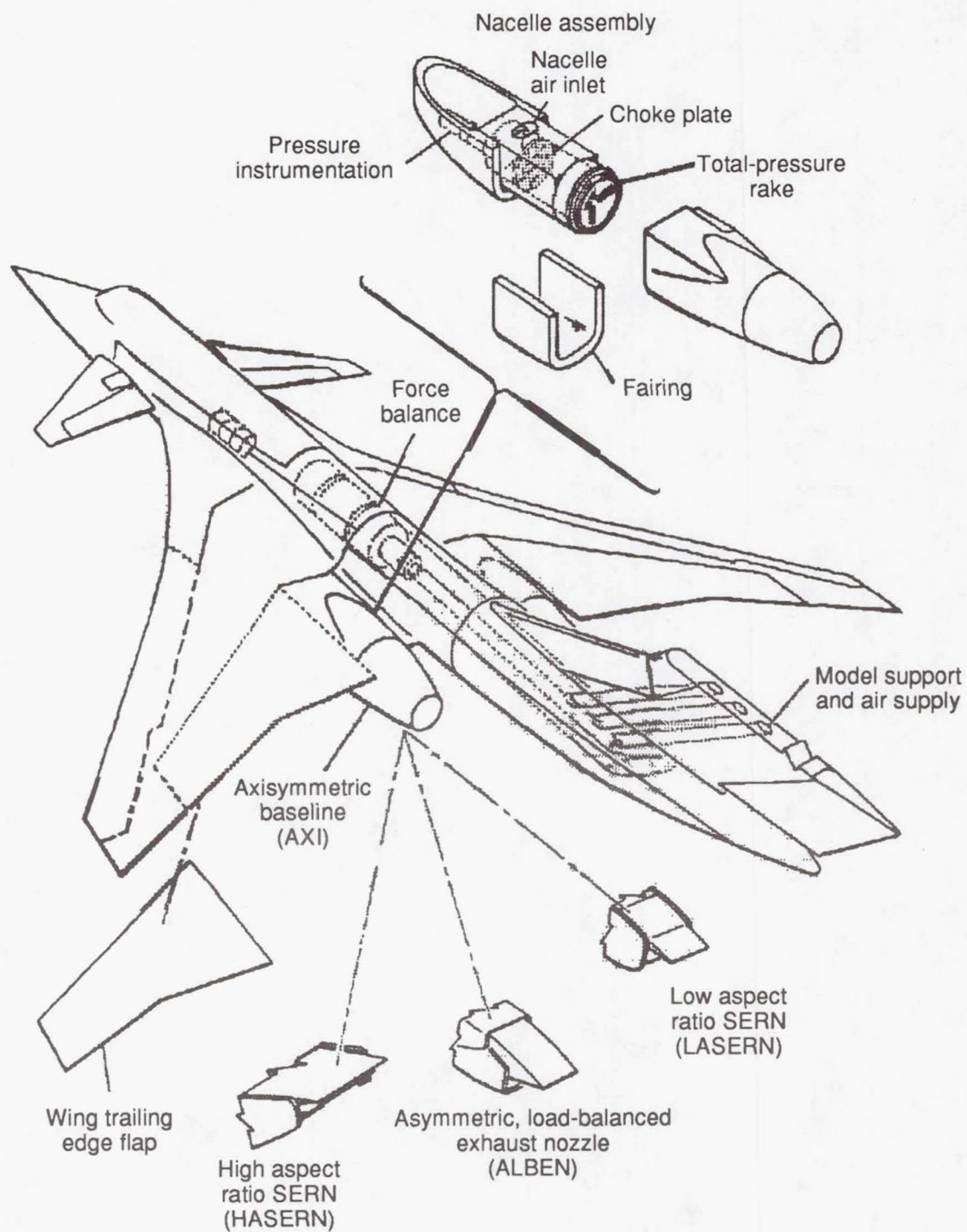
(c) Canard geometry.

Figure 1. Concluded.



L-93-15

Figure 2. Canard-wing fighter model in 14- by 22-Foot Subsonic Tunnel.



(a) Sketch of model components.

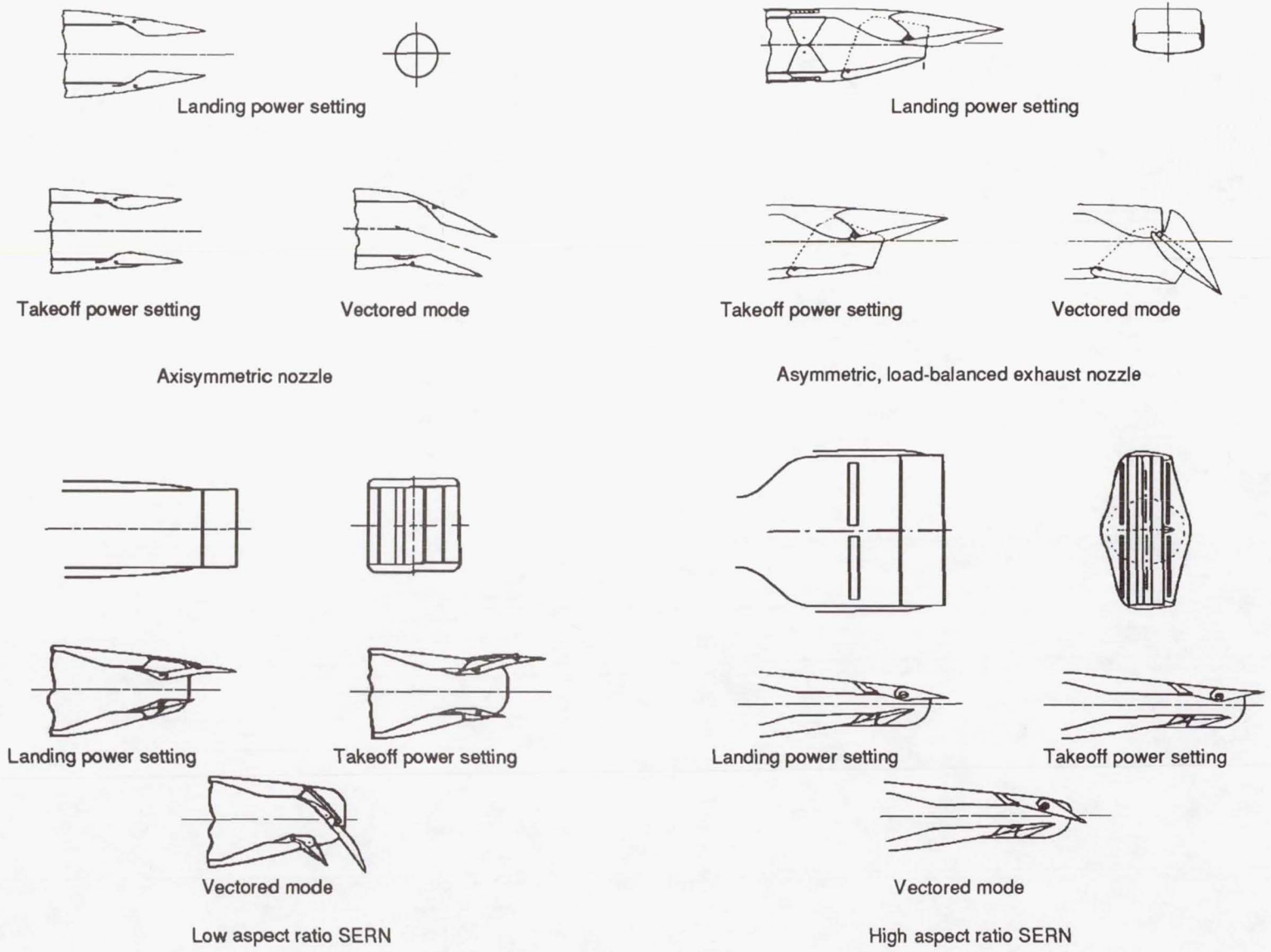
Figure 3. Wind-tunnel model of canard-wing fighter.



L-93-16

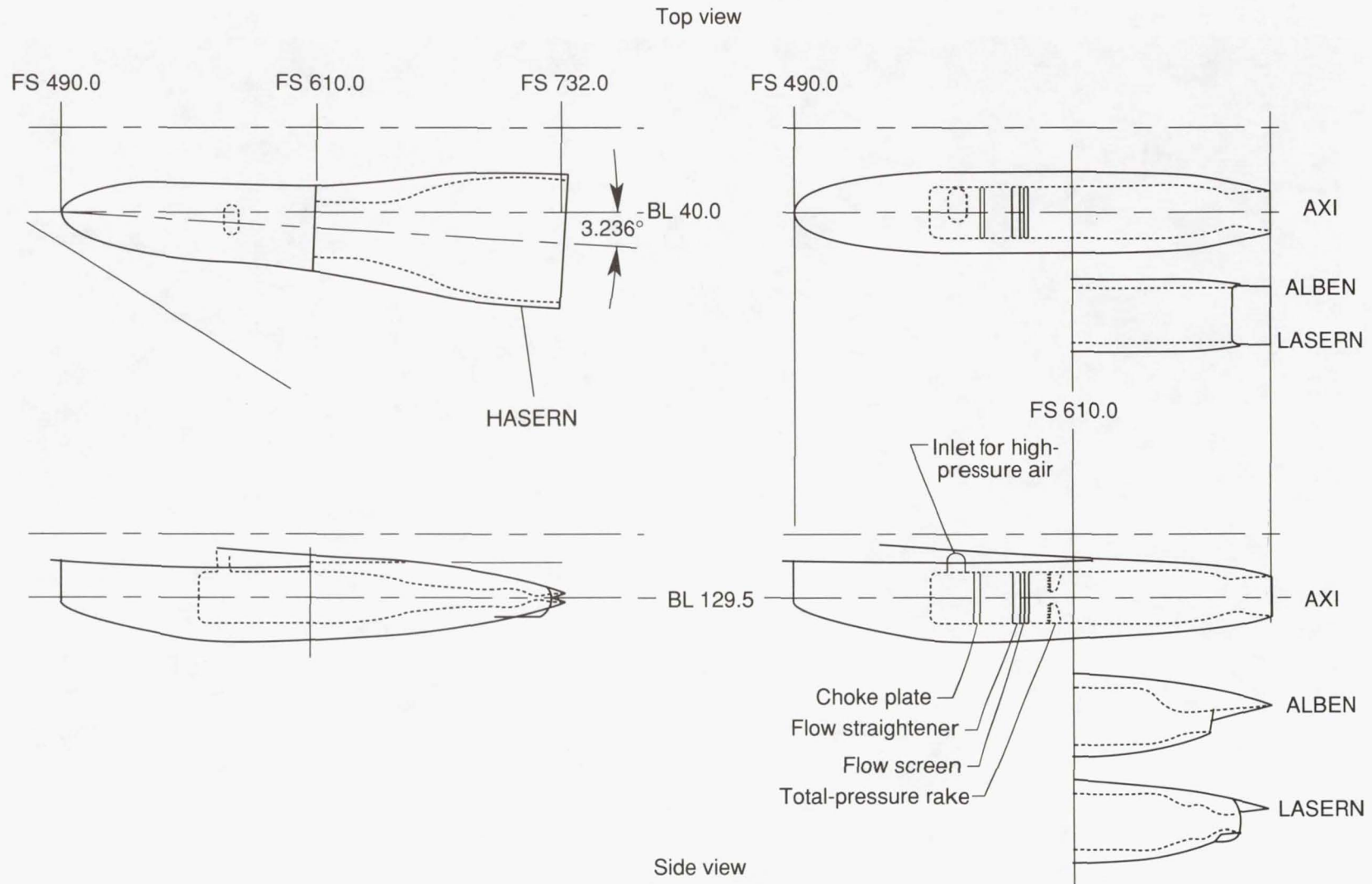
(b) Model components.

Figure 3. Concluded.



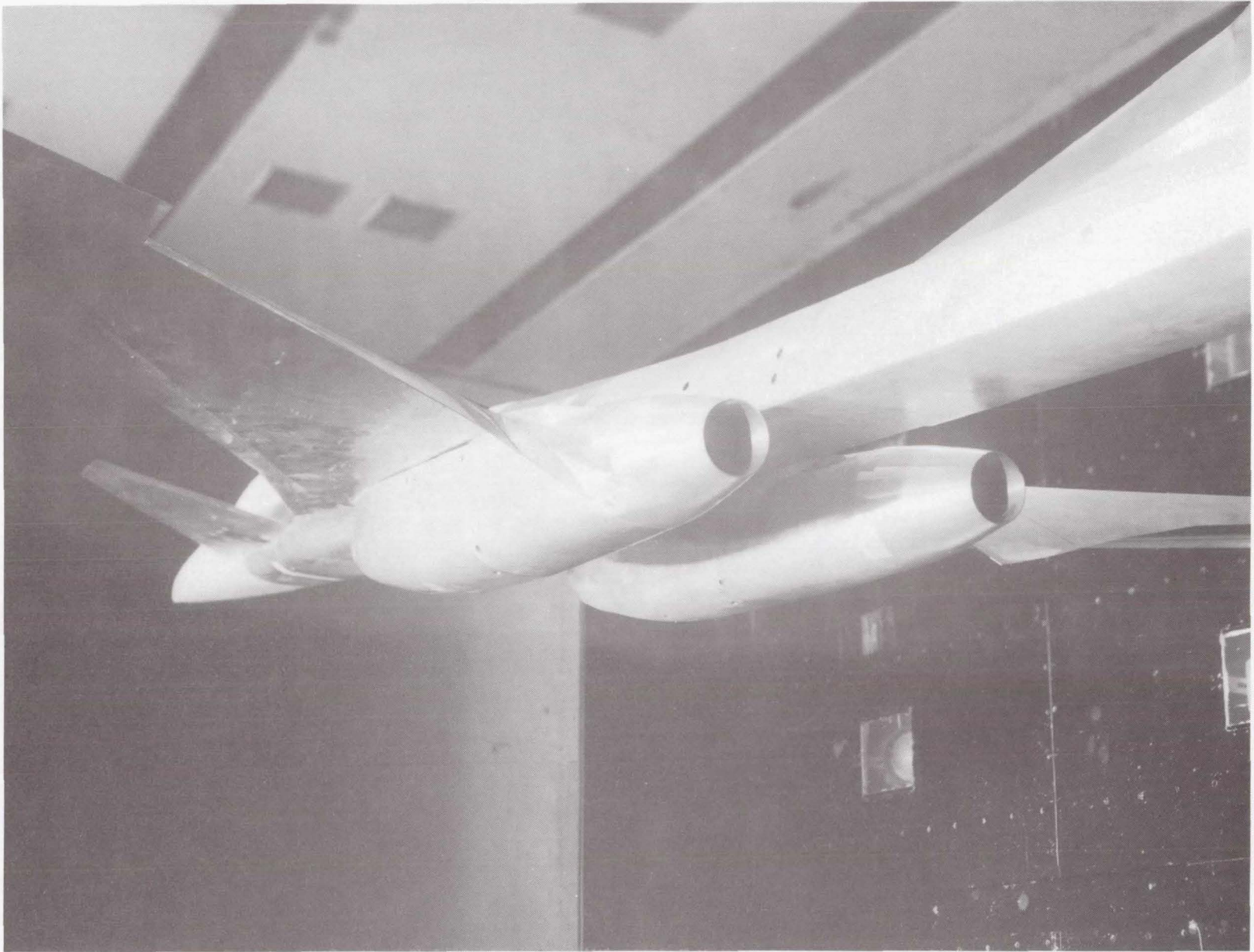
(a) Nozzles at various settings.

Figure 4. Four nozzle test concepts.



(b) Nacelle-nozzle installation. All linear dimensions are in inches.

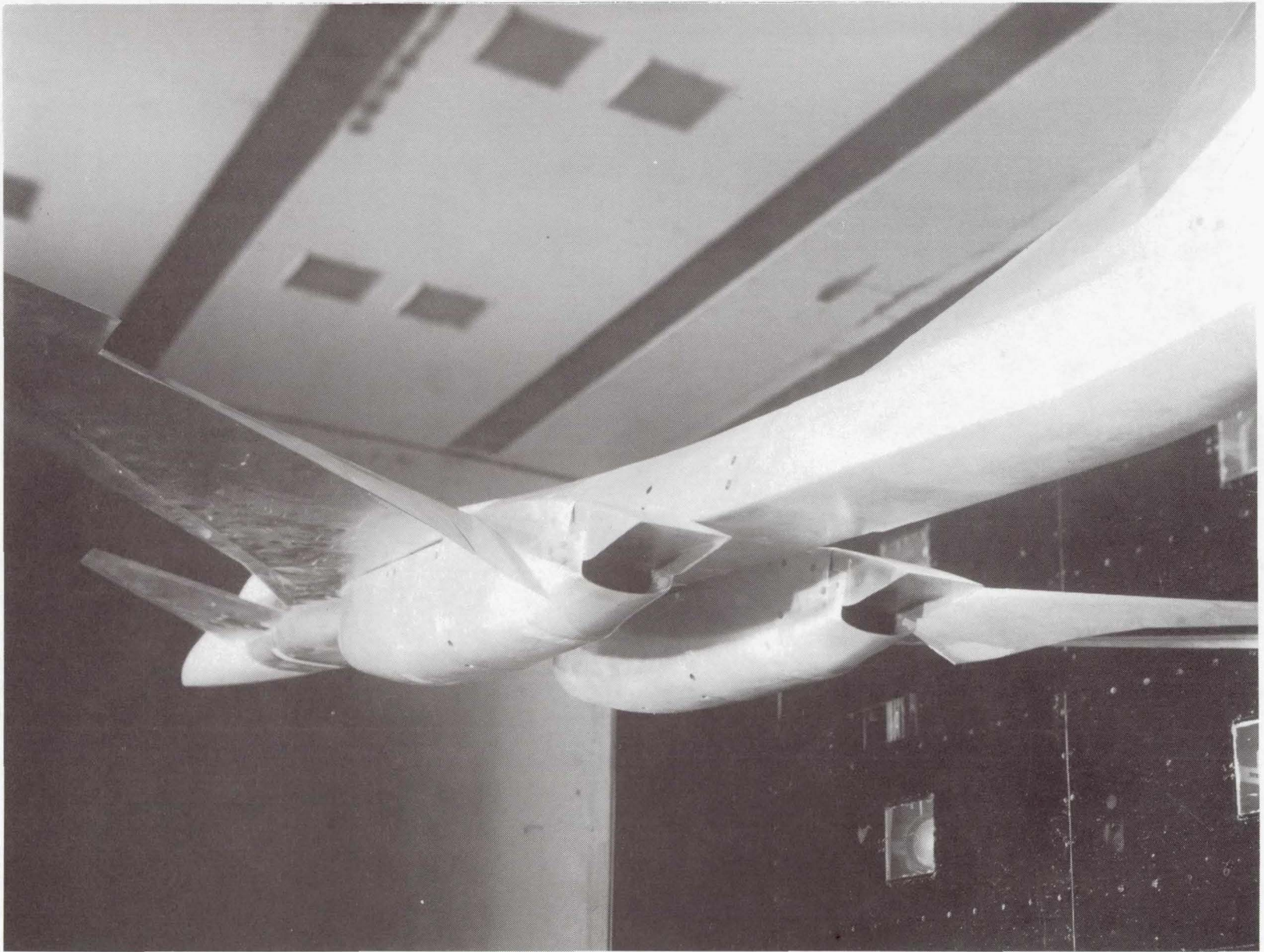
Figure 4. Concluded.



L-83-5,983

(a) Axisymmetric nozzle.

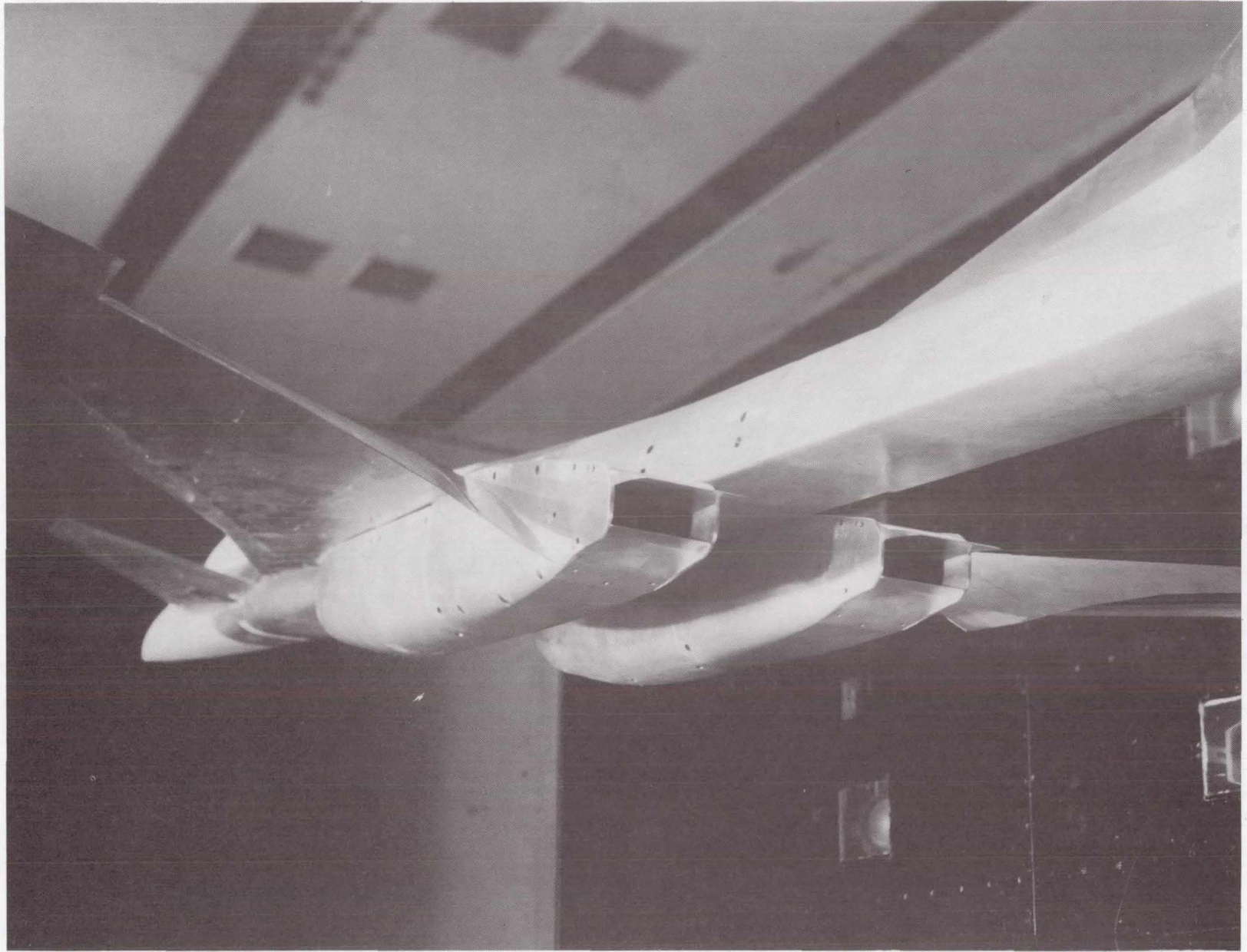
Figure 5. Rear view of four nozzle concepts.



L-83-5,988

(b) Asymmetric, load-balanced exhaust nozzle.

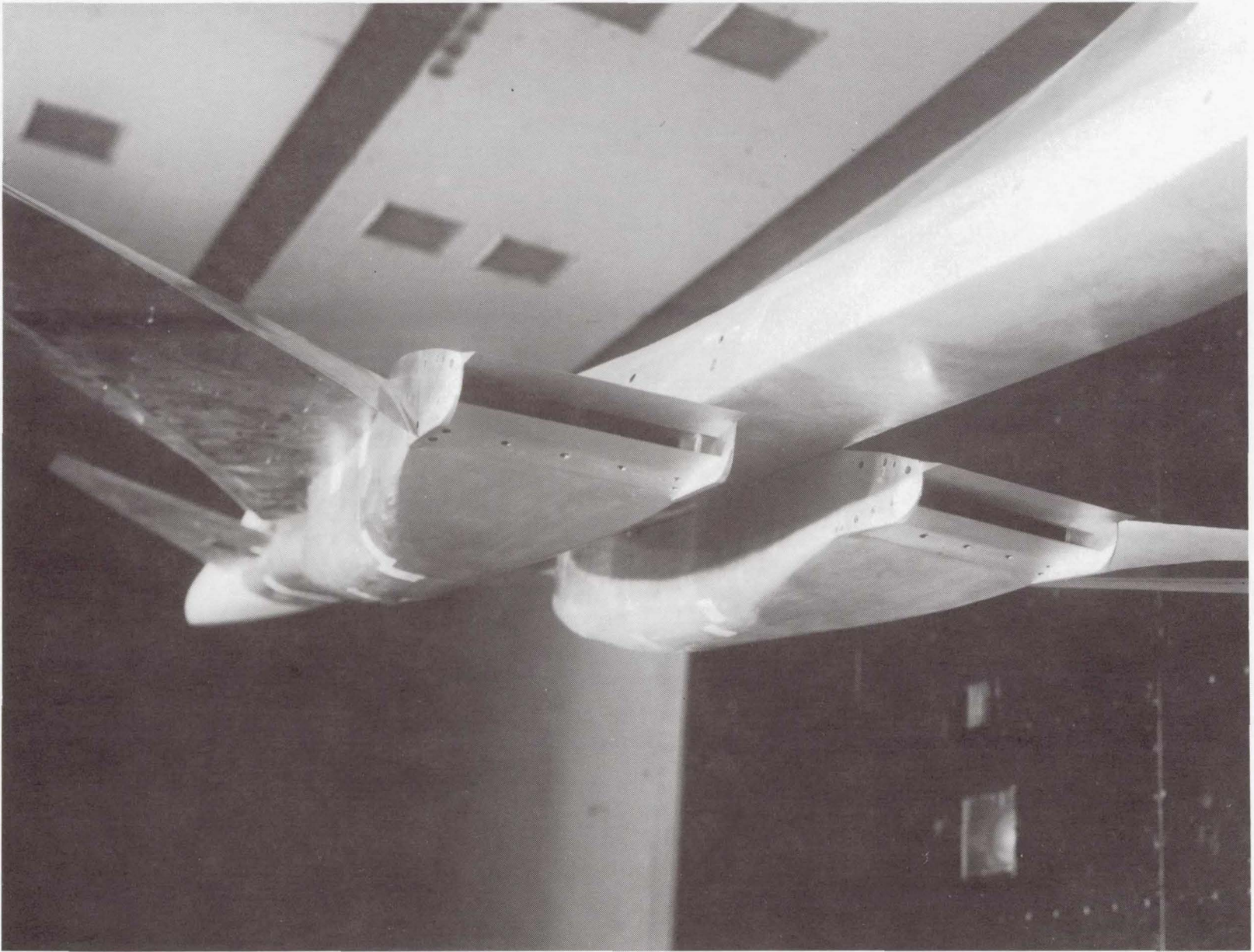
Figure 5. Continued.



L-83-5,985

(c) Low aspect ratio, single expansion ramp nozzle.

Figure 5. Continued.



(d) High aspect ratio, single expansion ramp nozzle.

L-83-5,982

Figure 5. Concluded.

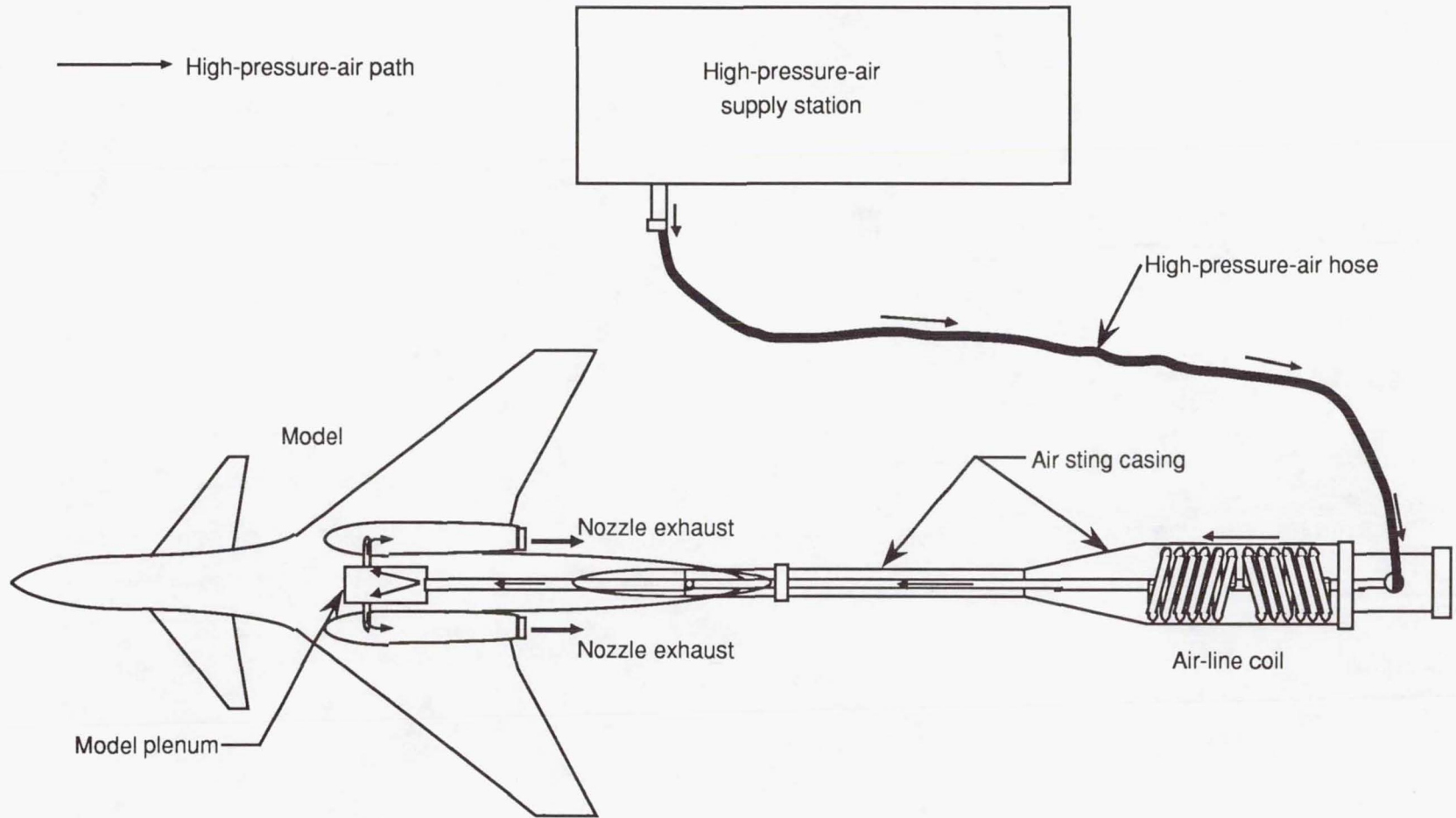
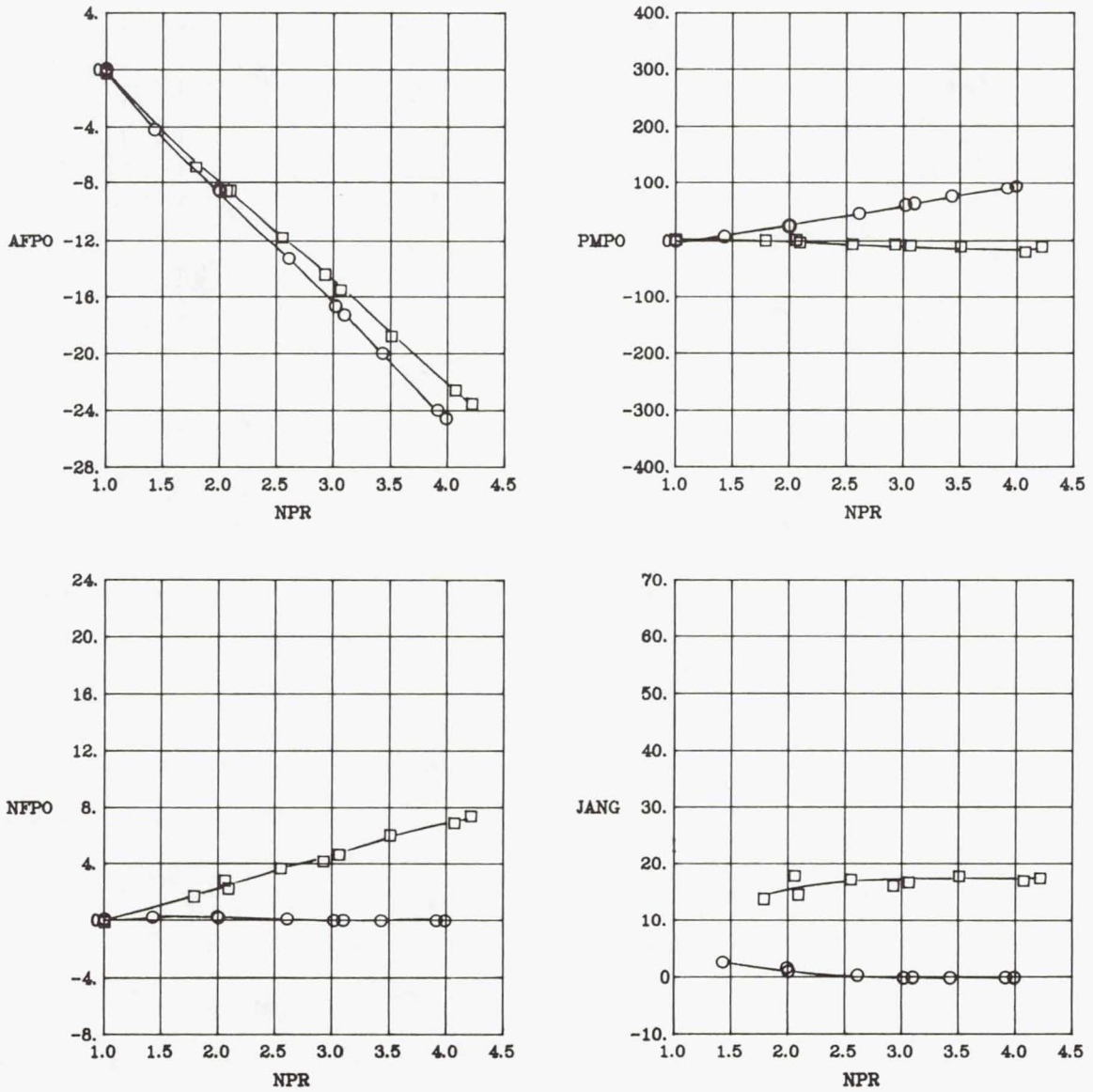


Figure 6. High-pressure-air supply to model.

$\delta_N$ , deg

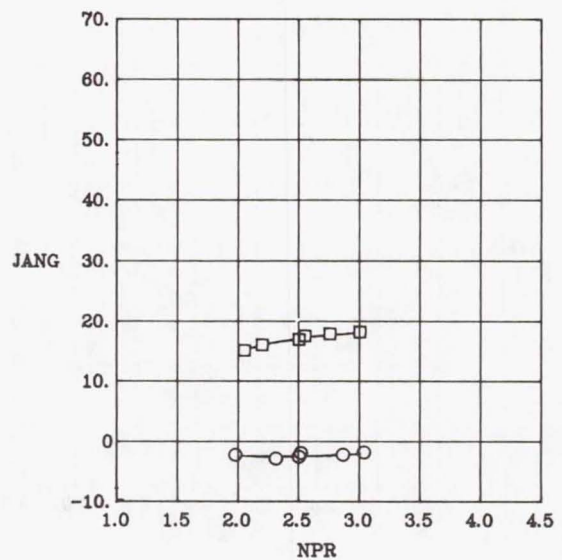
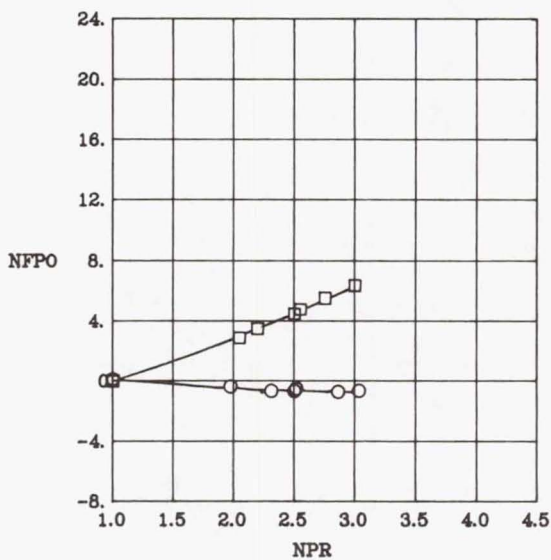
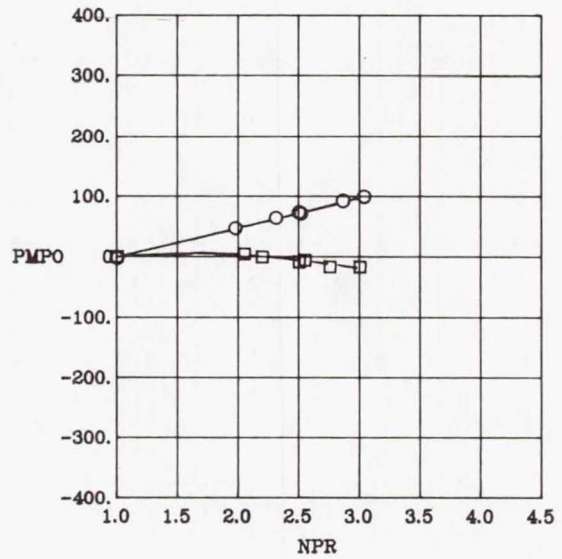
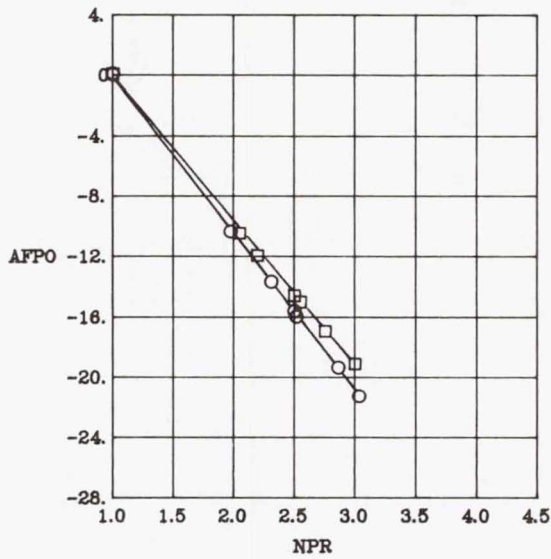
○ 0  
□ 20



(a) Landing power setting.

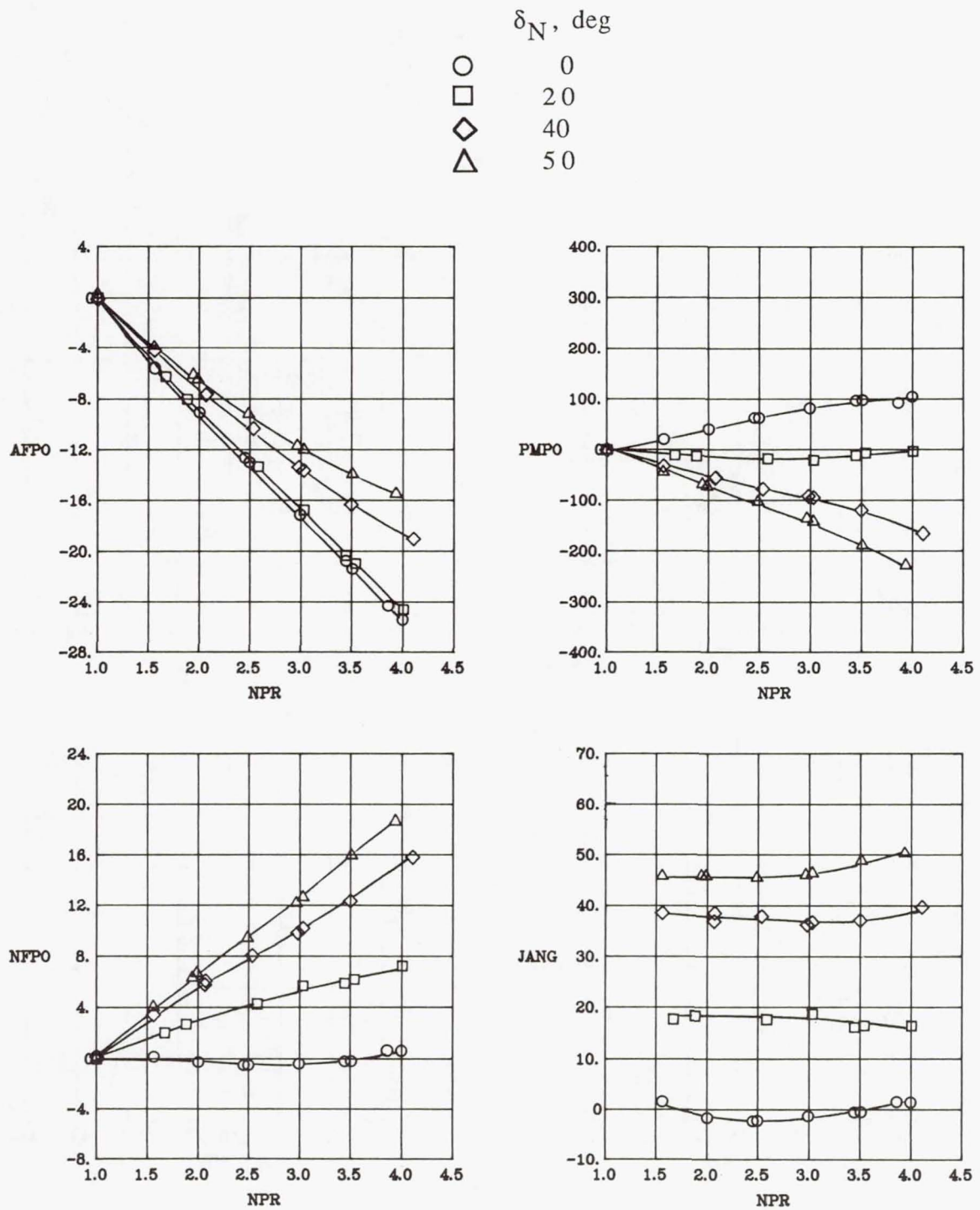
Figure 7. Longitudinal and jet angle static data for axisymmetric nozzle concept.

$\delta_N$ , deg  
 ○ 0  
 □ 20



(b) Takeoff power setting.

Figure 7. Concluded.

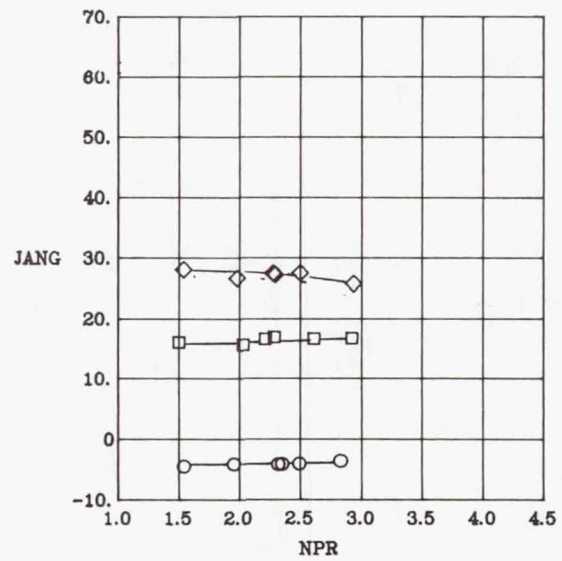
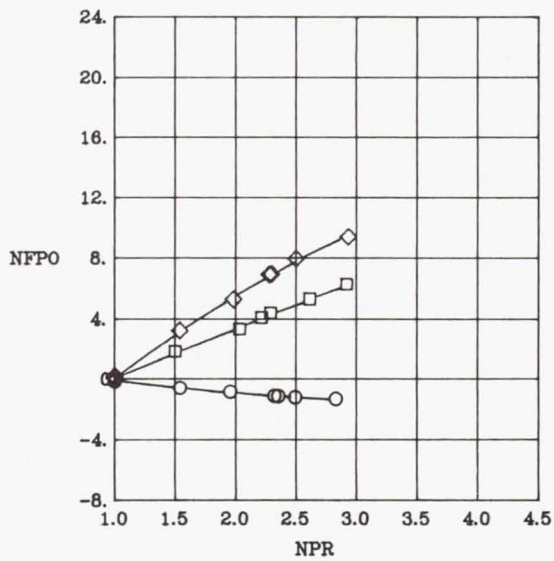
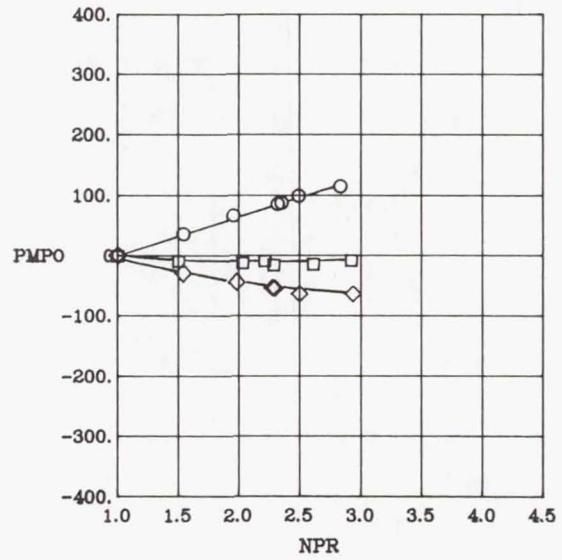
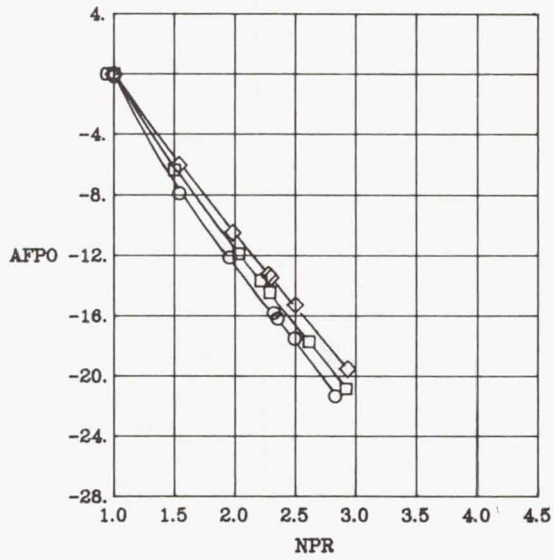


(a) Landing power setting.

Figure 8. Longitudinal and jet angle static data for asymmetric, load-balanced exhaust nozzle concept.

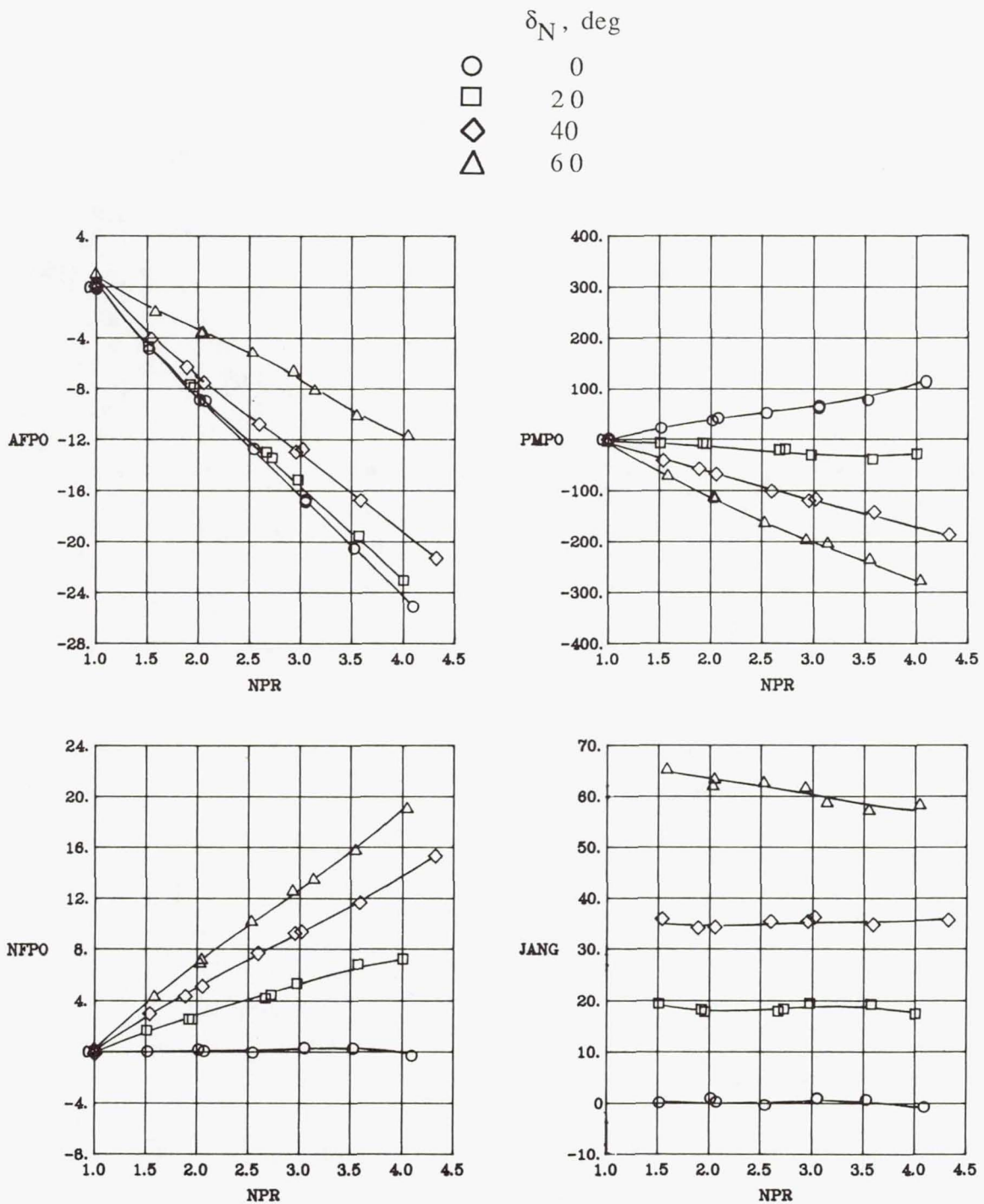
$\delta_N$ , deg

○ 0  
 □ 20  
 ◇ 30



(b) Takeoff power setting.

Figure 8. Concluded.

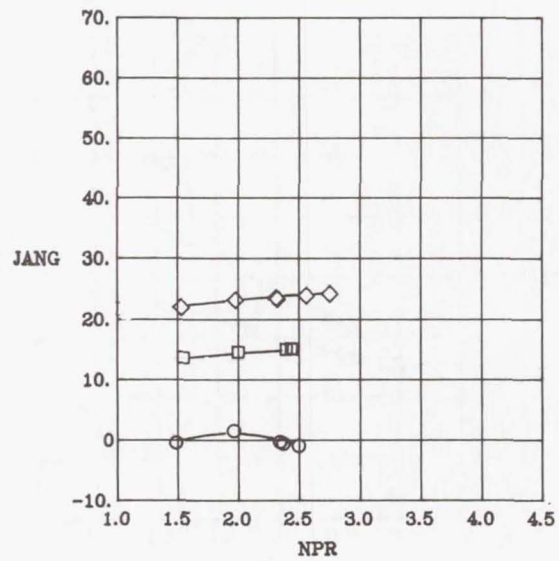
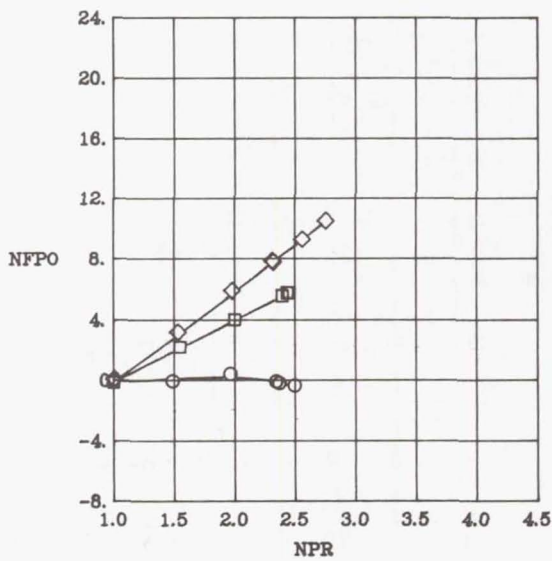
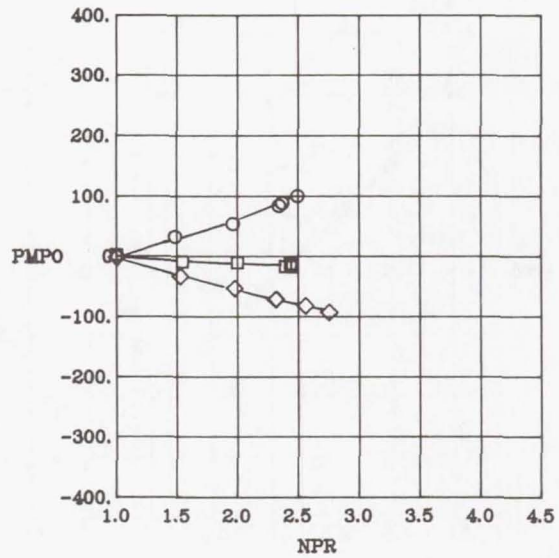
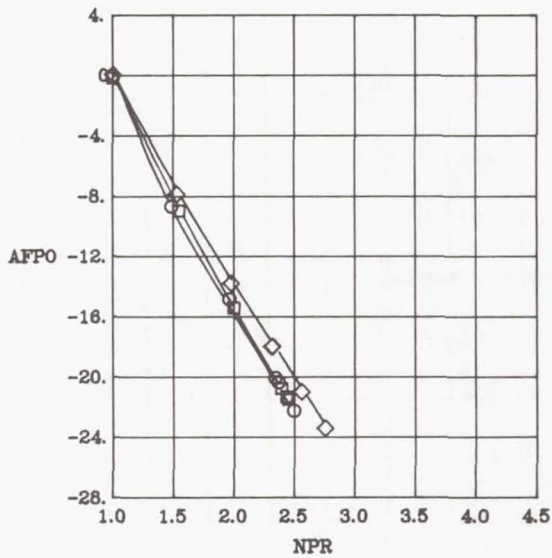


(a) Landing power setting.

Figure 9. Longitudinal and jet angle static data for low aspect ratio SERN concept.

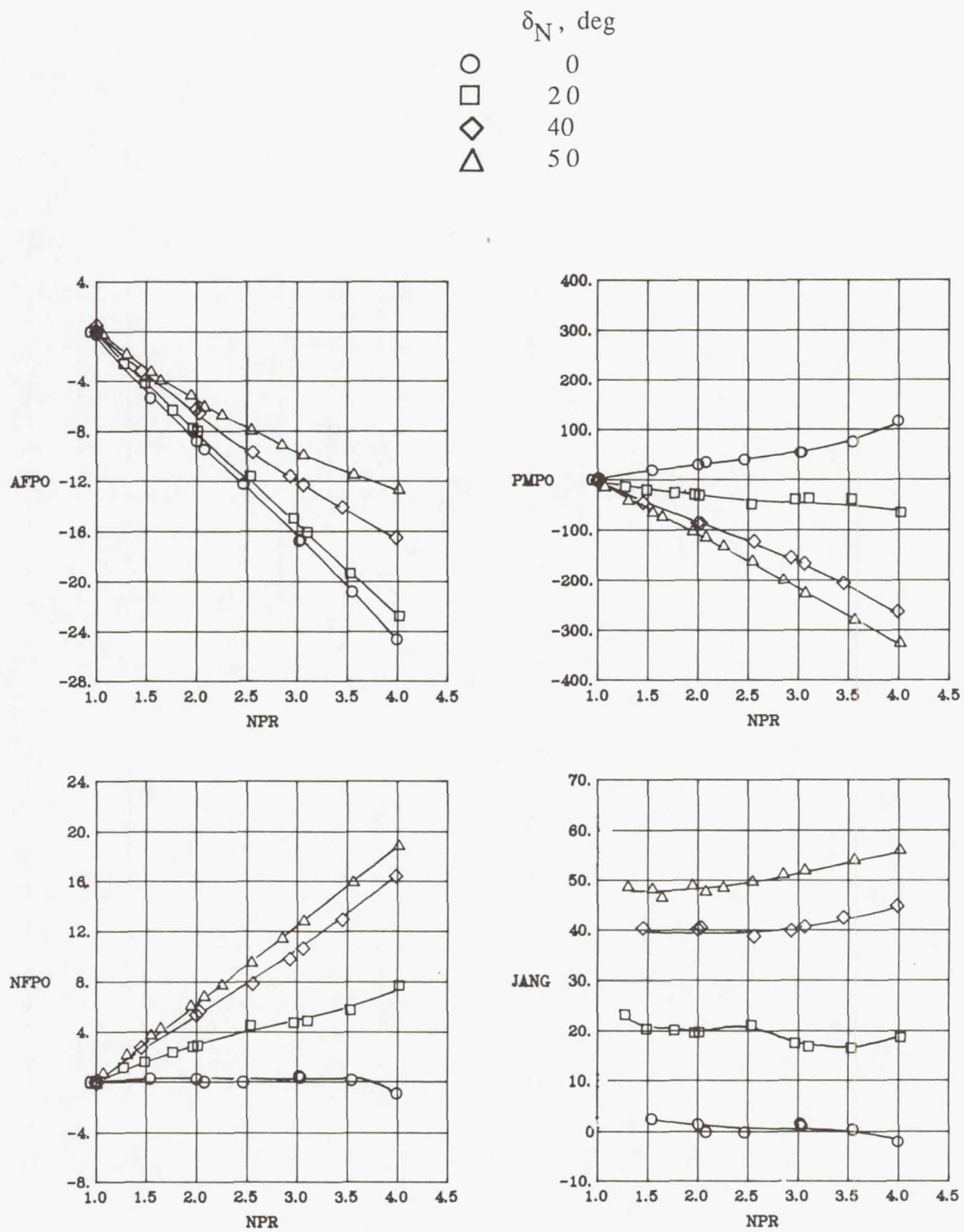
$\delta_N$ , deg

○ 0  
 □ 20  
 ◇ 30



(b) Takeoff power setting.

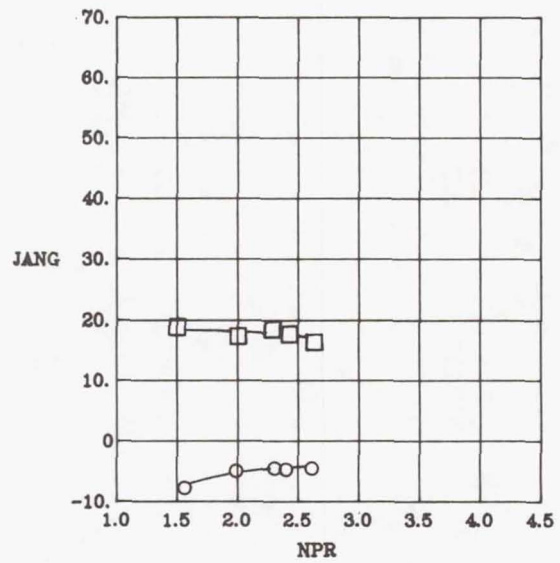
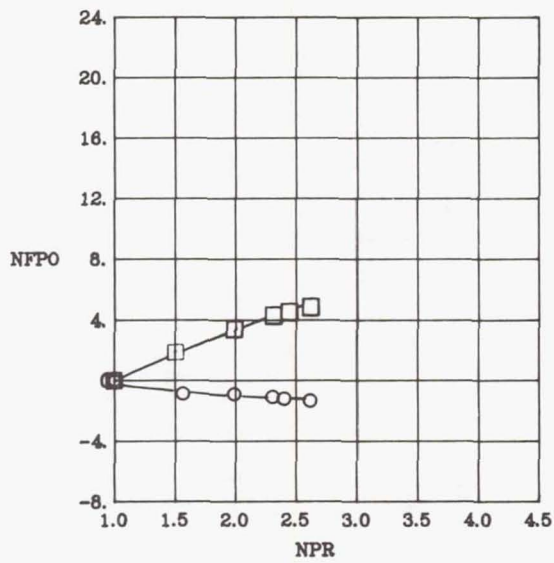
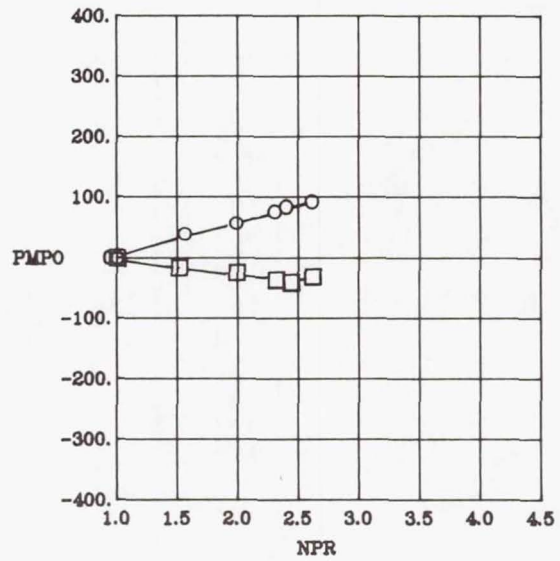
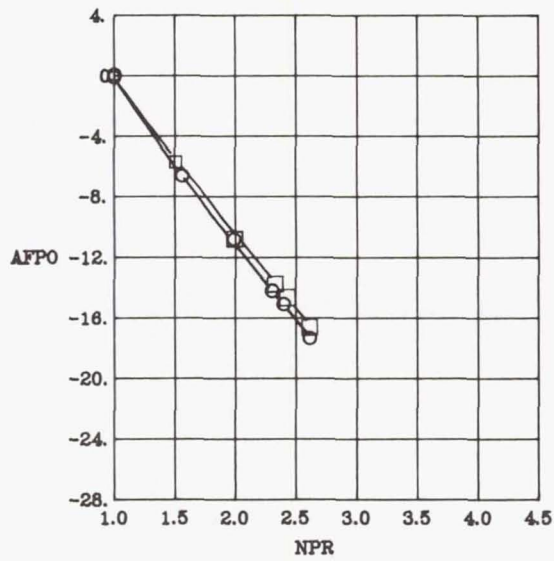
Figure 9. Concluded.



(a) Landing power setting.

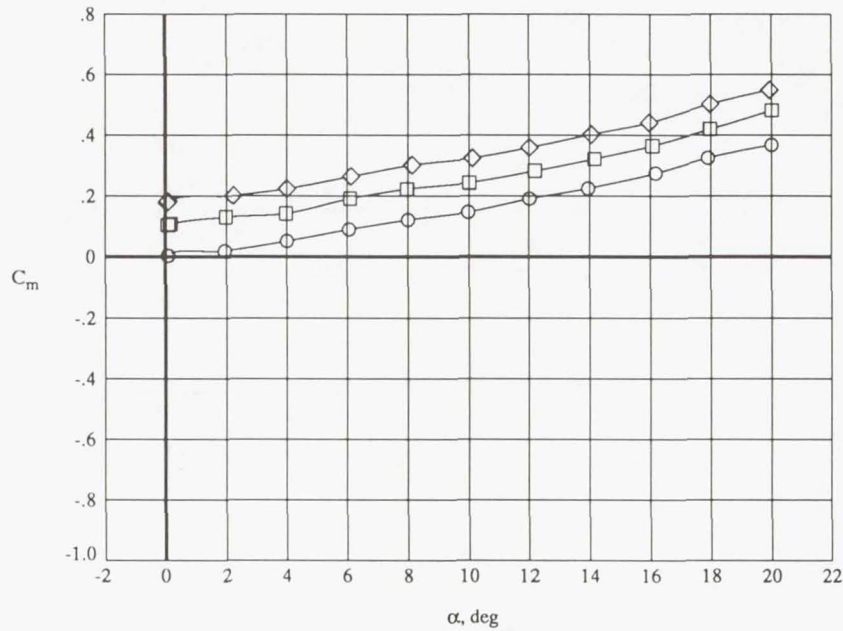
Figure 10. Longitudinal and jet angle static data for high aspect ratio SERN concept.

$\delta_N$ , deg  
 ○ 0  
 □ 20



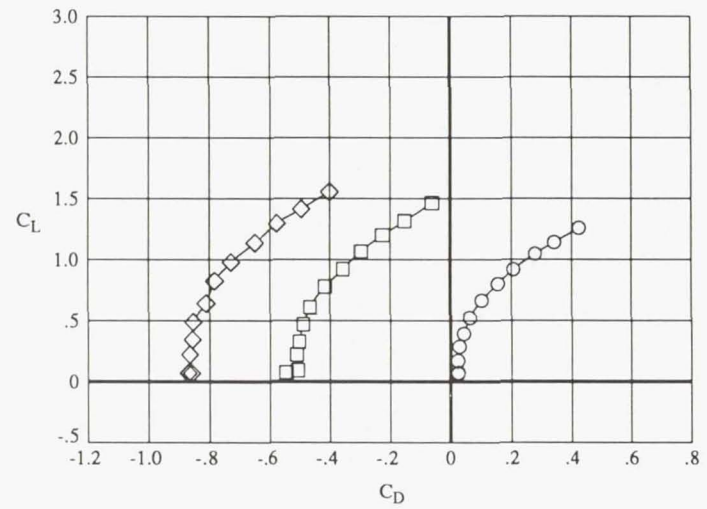
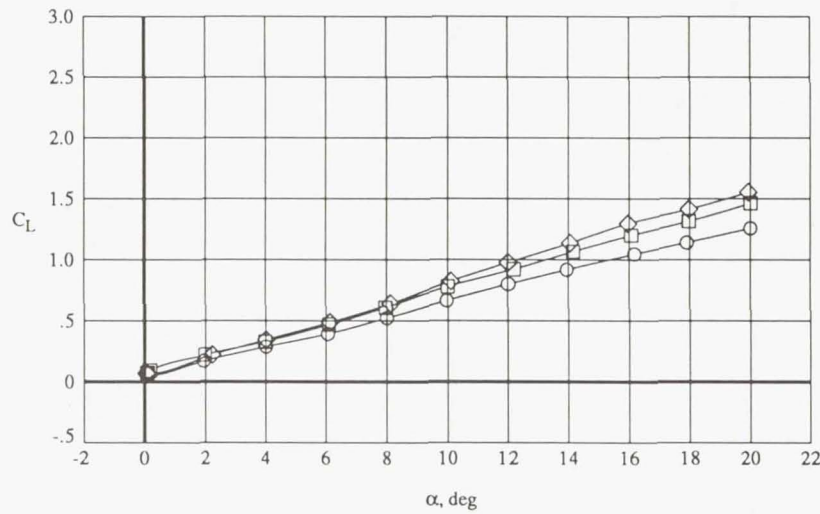
(b) Takeoff power setting.

Figure 10. Concluded.



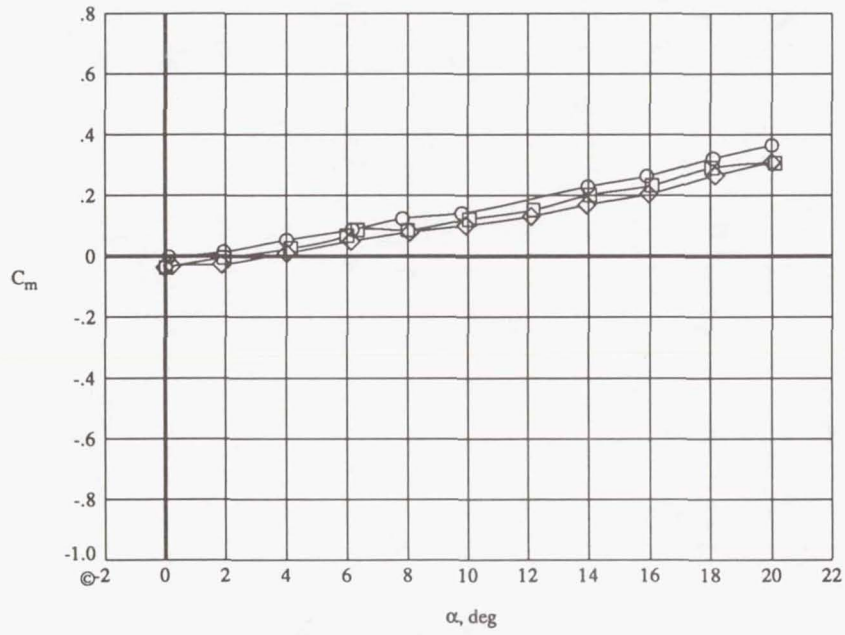
NPR

- 1.0
- 2.5
- ◇ 3.5



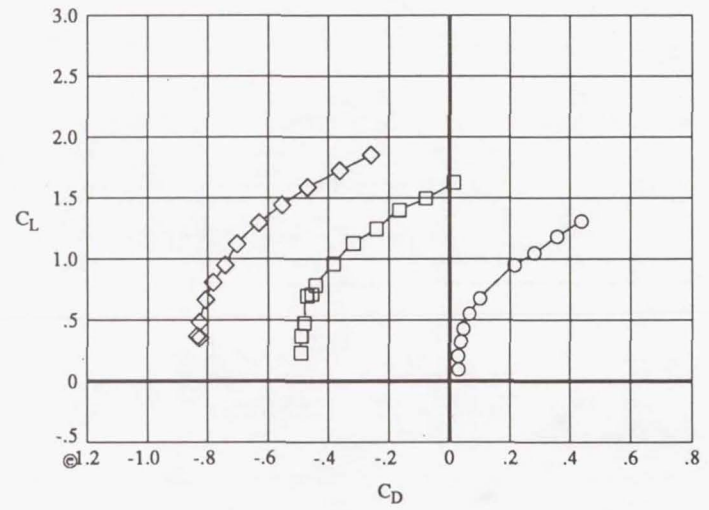
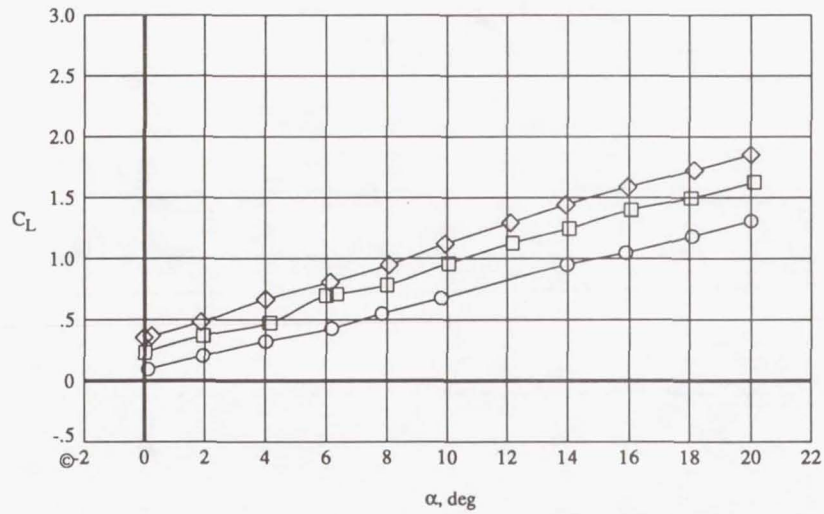
(a)  $\delta_N = 0^\circ L$ .

Figure 11. Effects of NPR on longitudinal aerodynamic characteristics of AXI concept with  $\delta_f = 0^\circ$ .



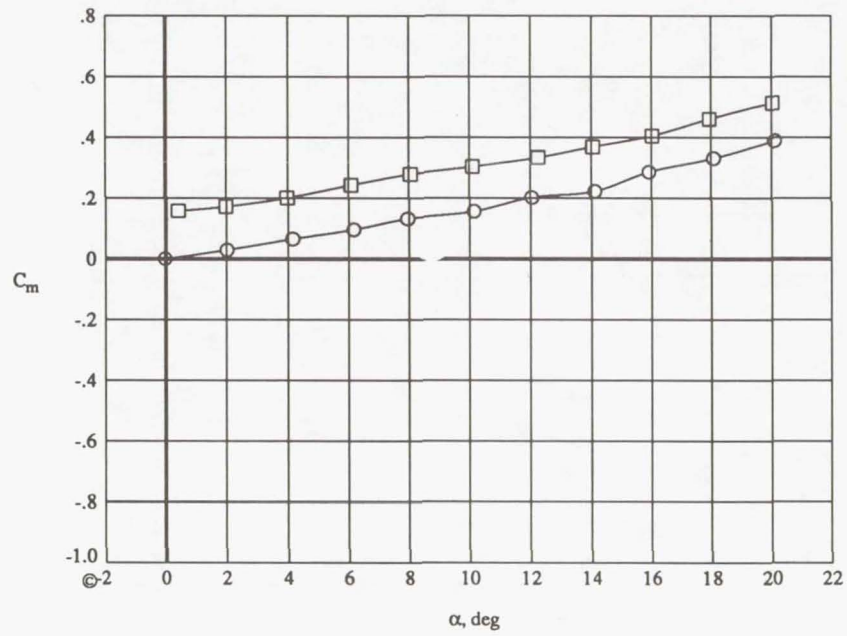
NPR

○ 1.0  
 □ 2.5  
 ◇ 3.5

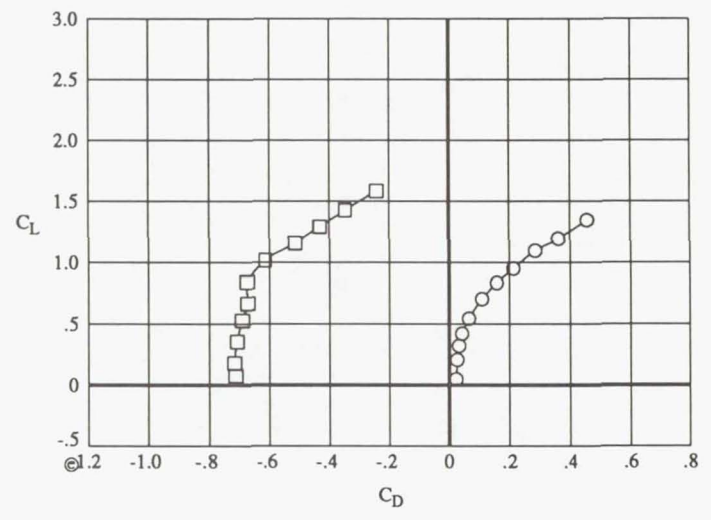
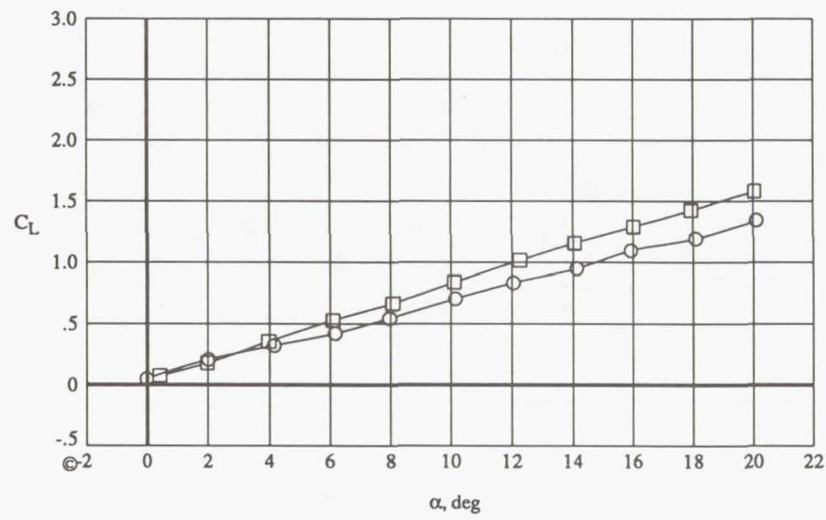


(b)  $\delta_N = 20^\circ L$ .

Figure 11. Continued.

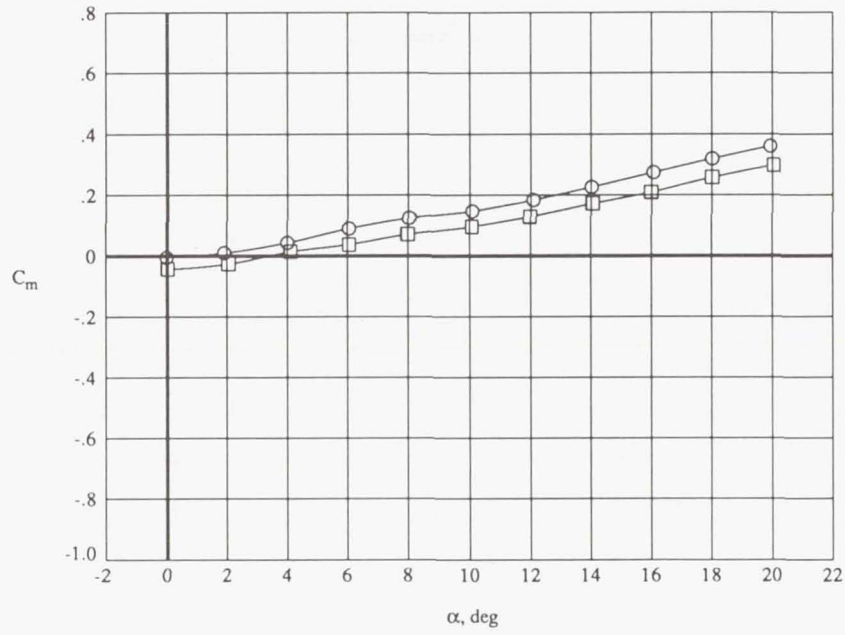


NPR  
 ○ 1.0  
 □ 2.5



(c)  $\delta_N = 0^\circ T$ .

Figure 11. Continued.



NPR

○ 1.0  
 □ 2.5

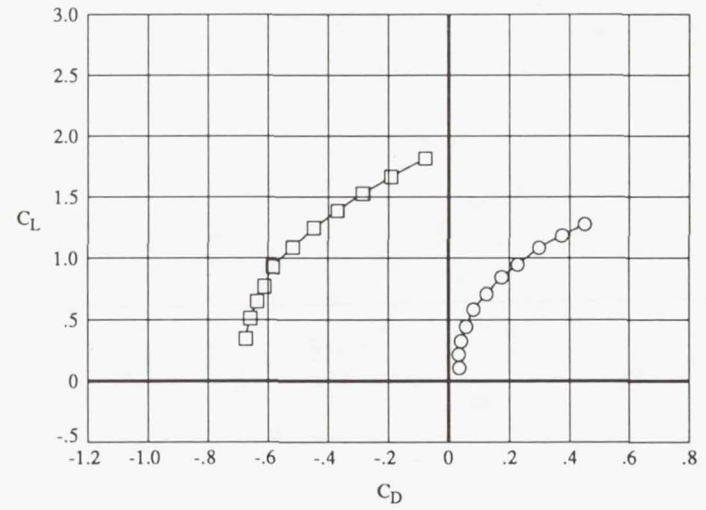
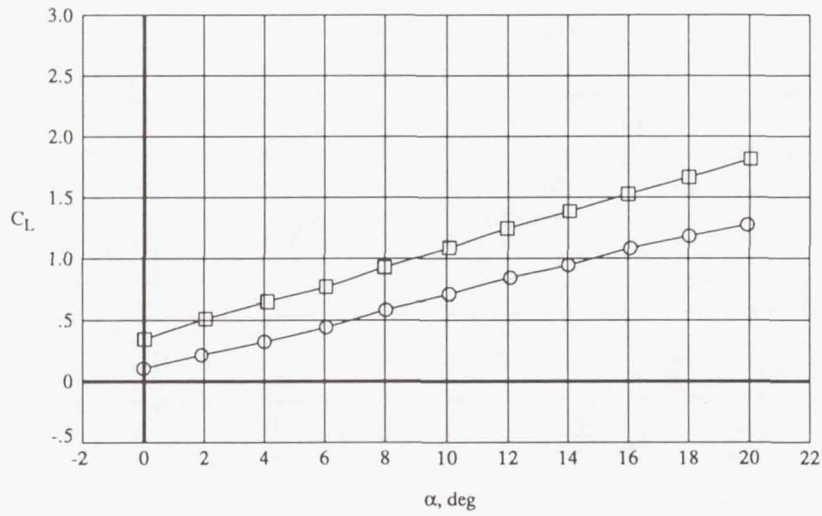
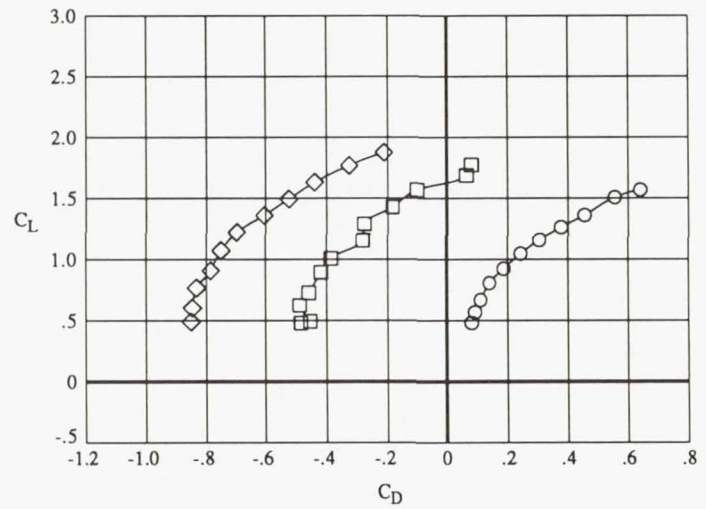
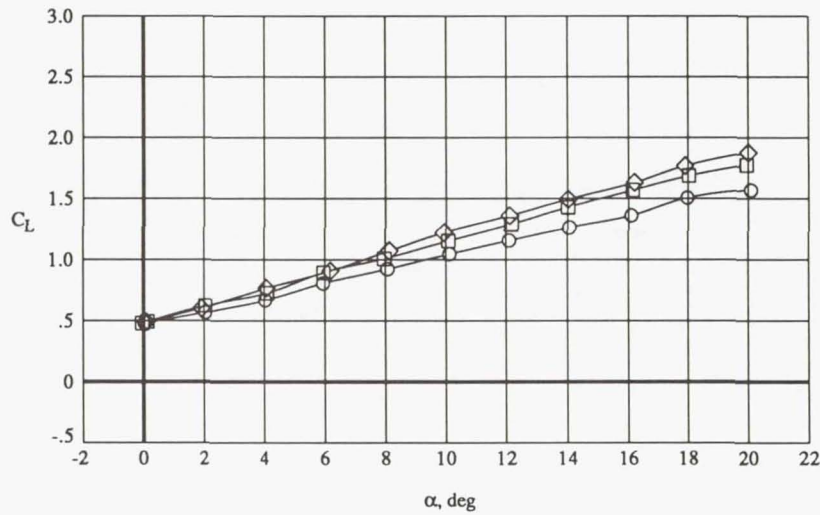
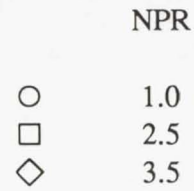
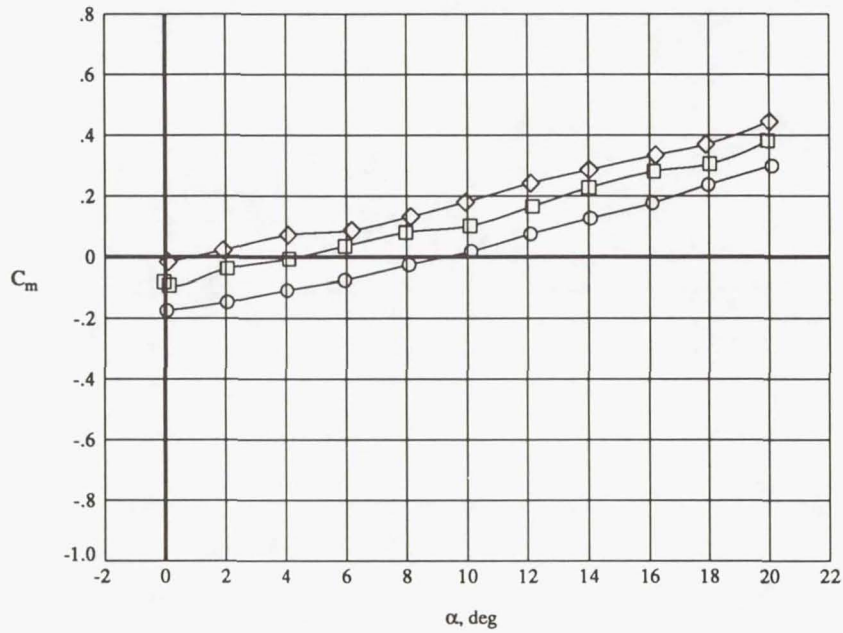
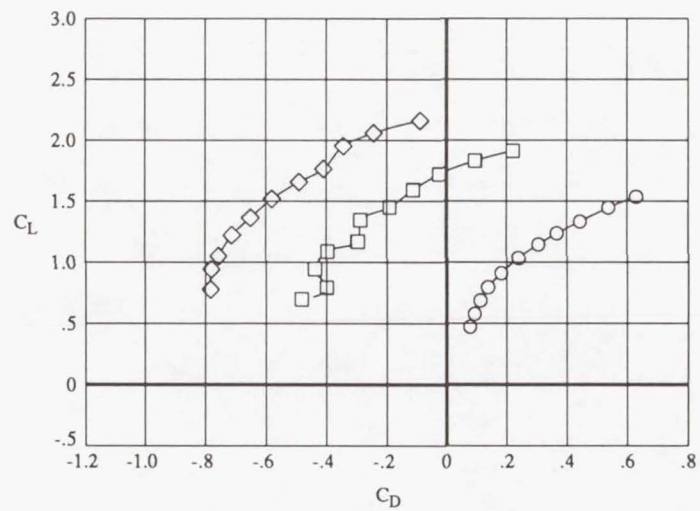
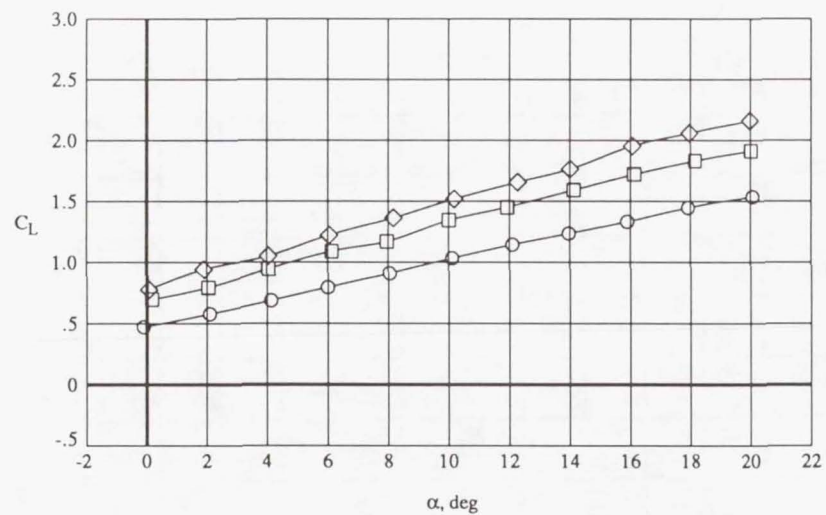
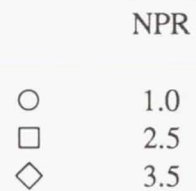
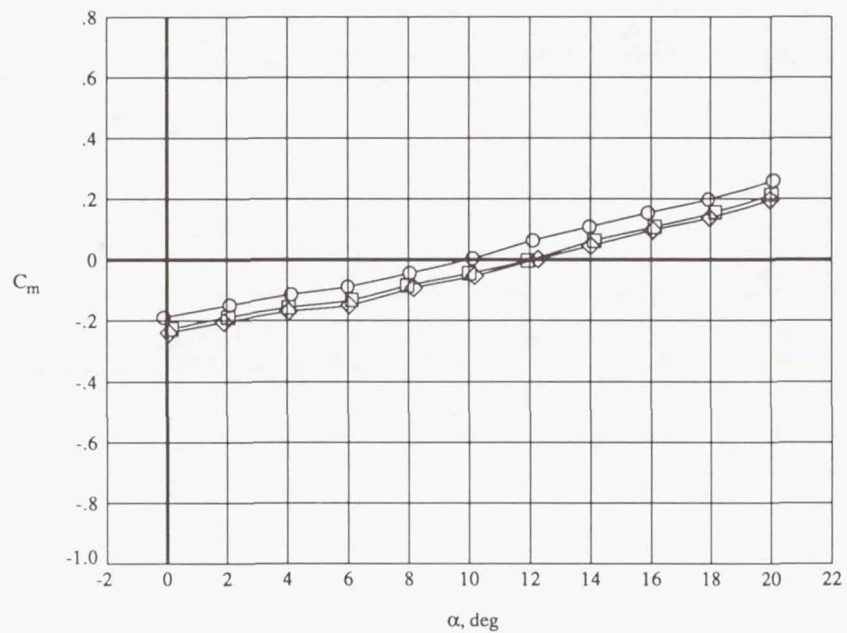
(d)  $\delta_N = 20^\circ T$ .

Figure 11. Concluded.



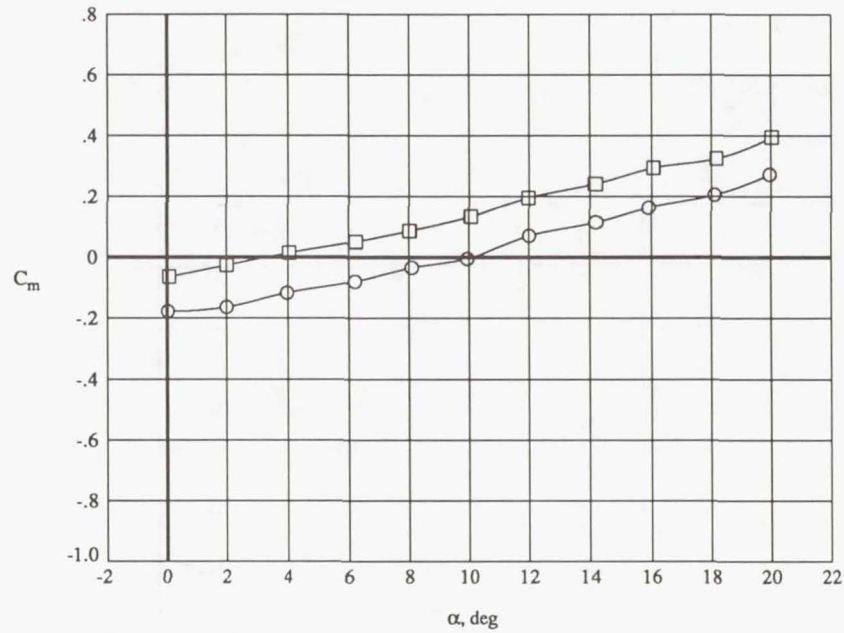
(a)  $\delta_N = 0^\circ L$ .

Figure 12. Effects of NPR on longitudinal aerodynamic characteristics of AXI concept with  $\delta_f = 20^\circ$ .

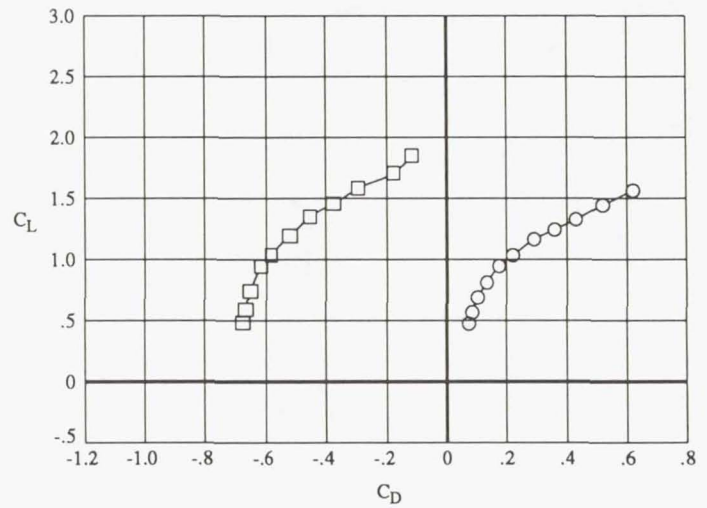
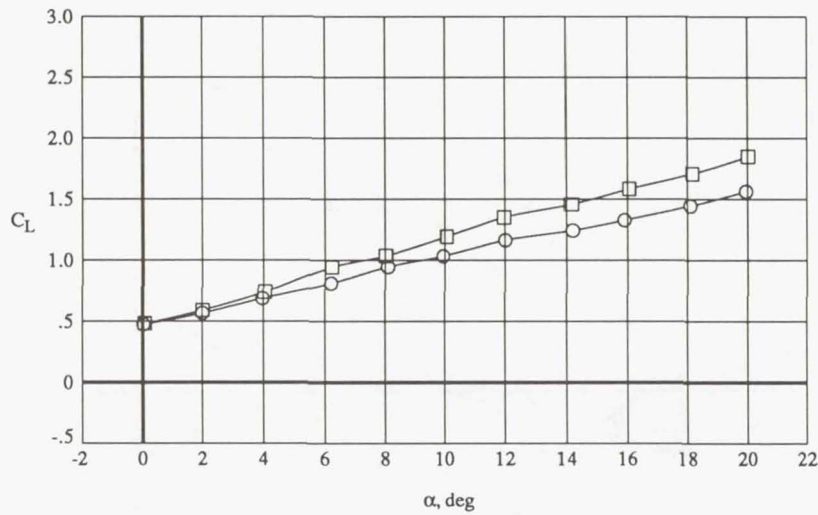


(b)  $\delta_N = 20^\circ L$ .

Figure 12. Continued.

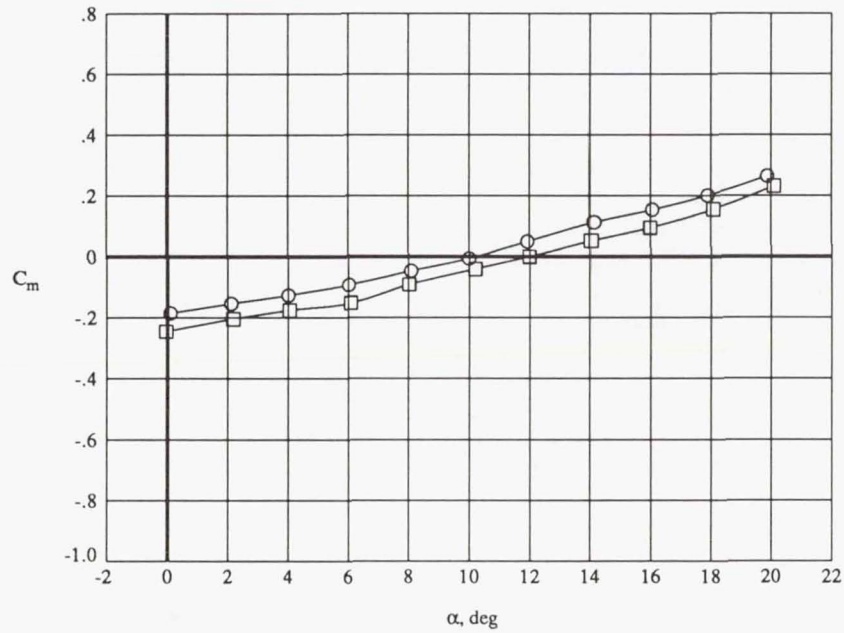


NPR  
 ○ 1.0  
 □ 2.5

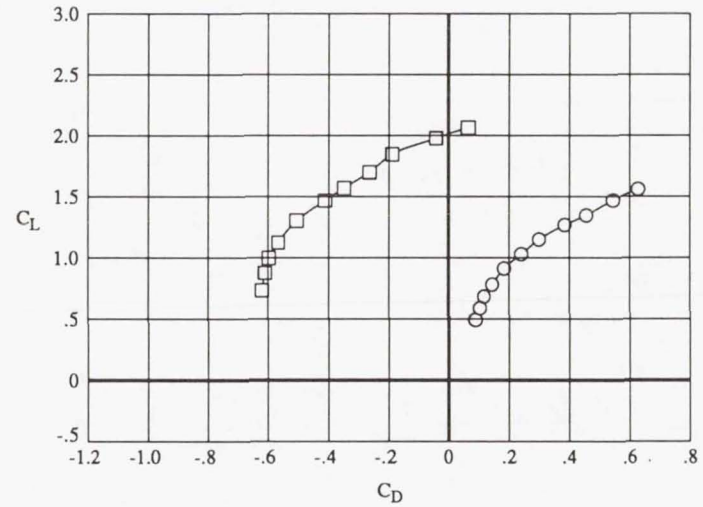
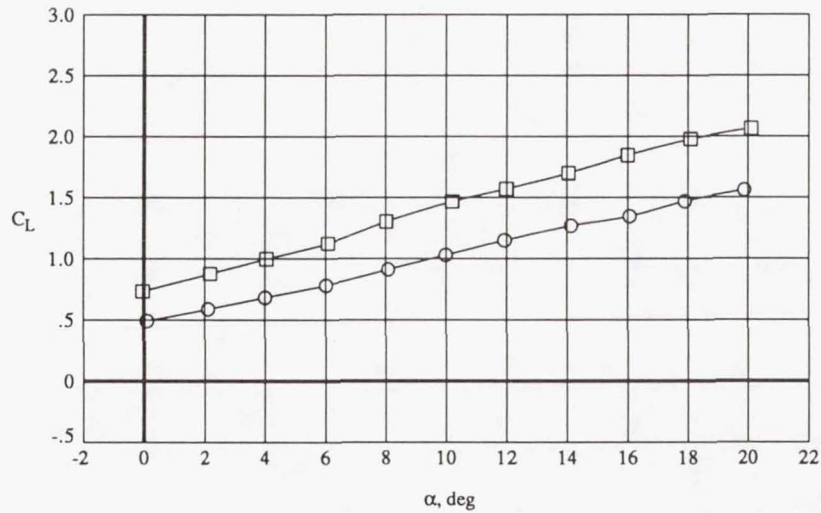


(c)  $\delta_N = 0^\circ T$ .

Figure 12. Continued.

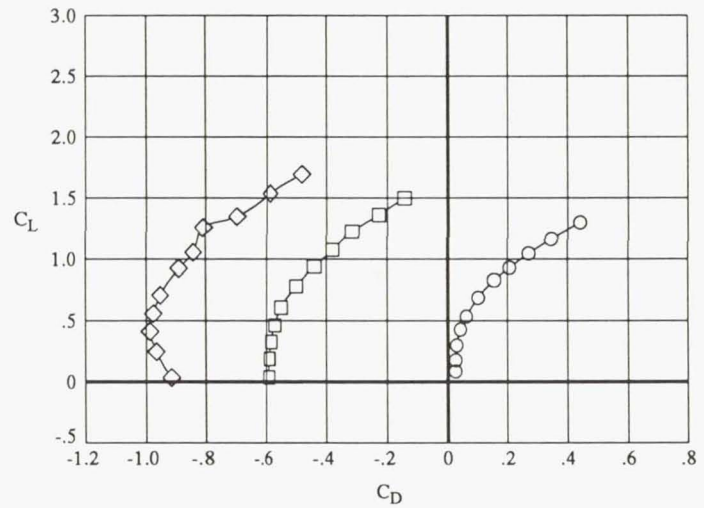
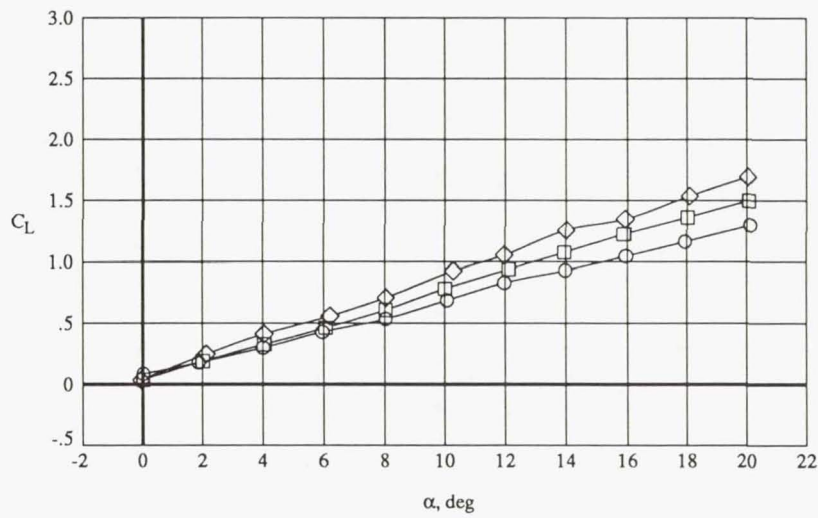
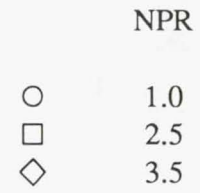
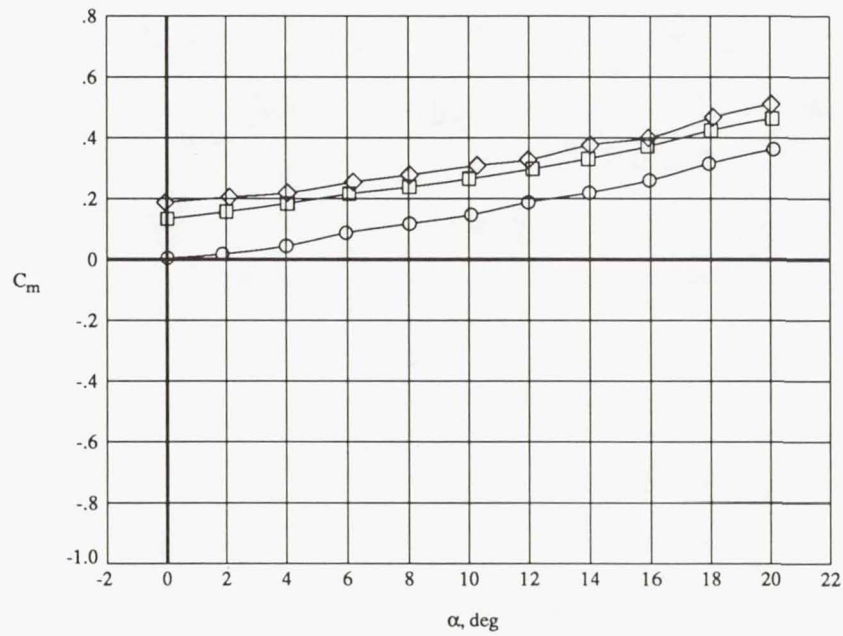


NPR  
 ○ 1.0  
 □ 2.5



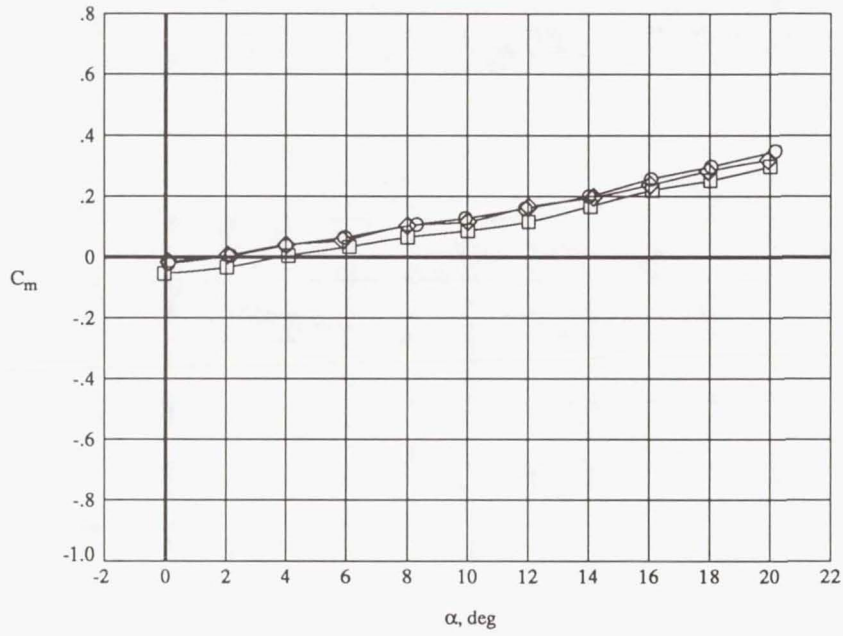
(d)  $\delta_N = 20^\circ T$ .

Figure 12. Concluded.



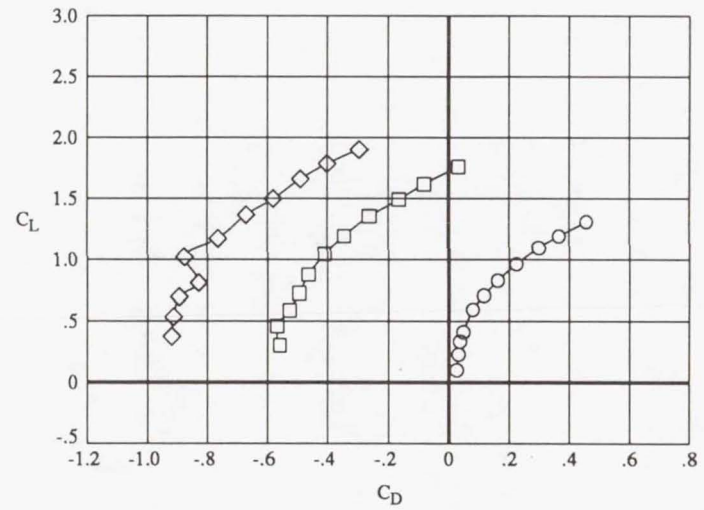
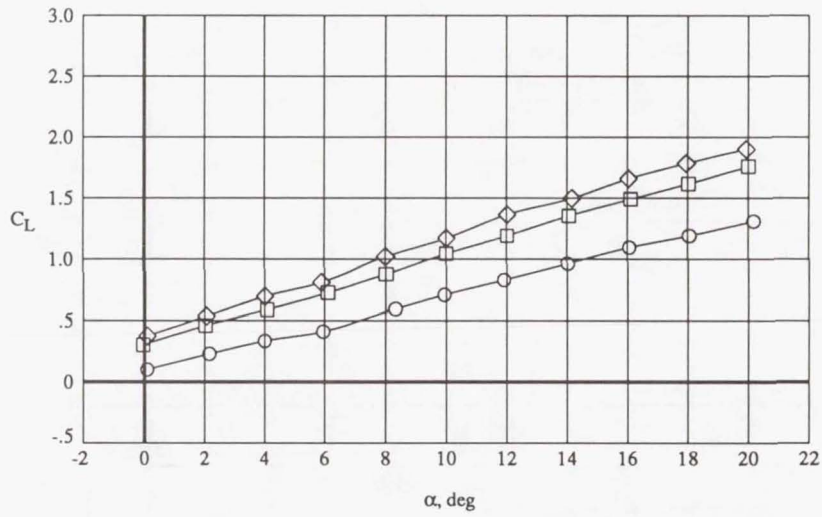
(a)  $\delta_N = 0^\circ L$ .

Figure 13. Effects of NPR on longitudinal aerodynamic characteristics of ALBEN concept with  $\delta_f = 0^\circ$ .



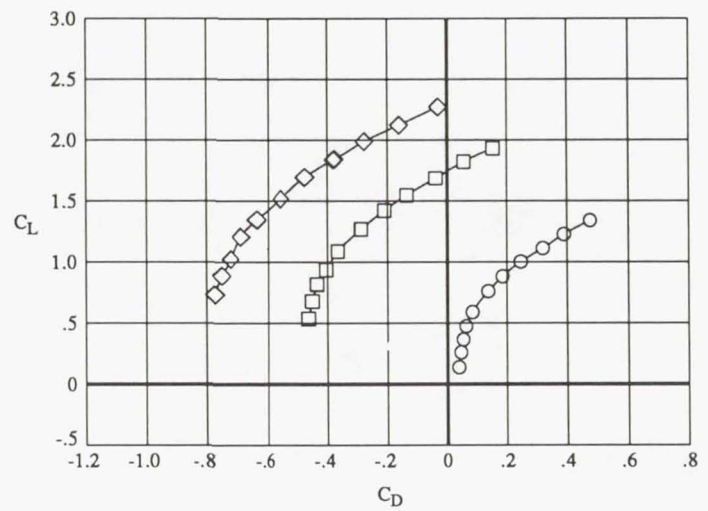
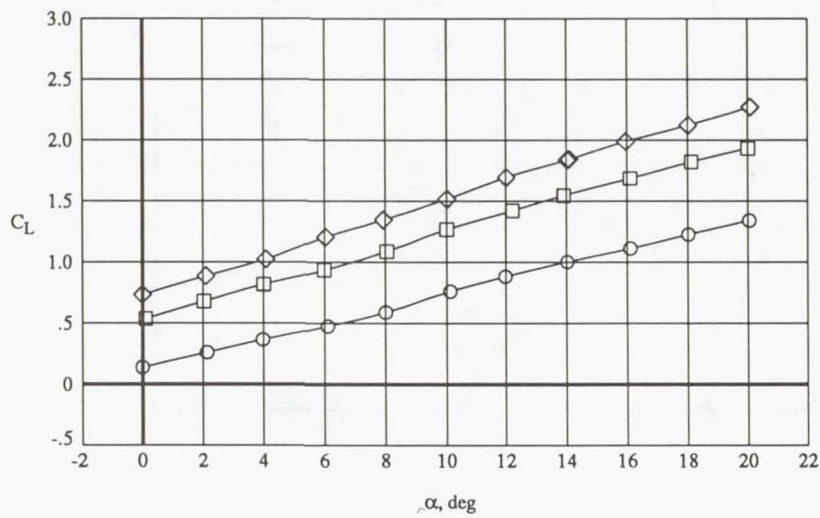
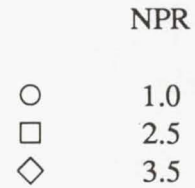
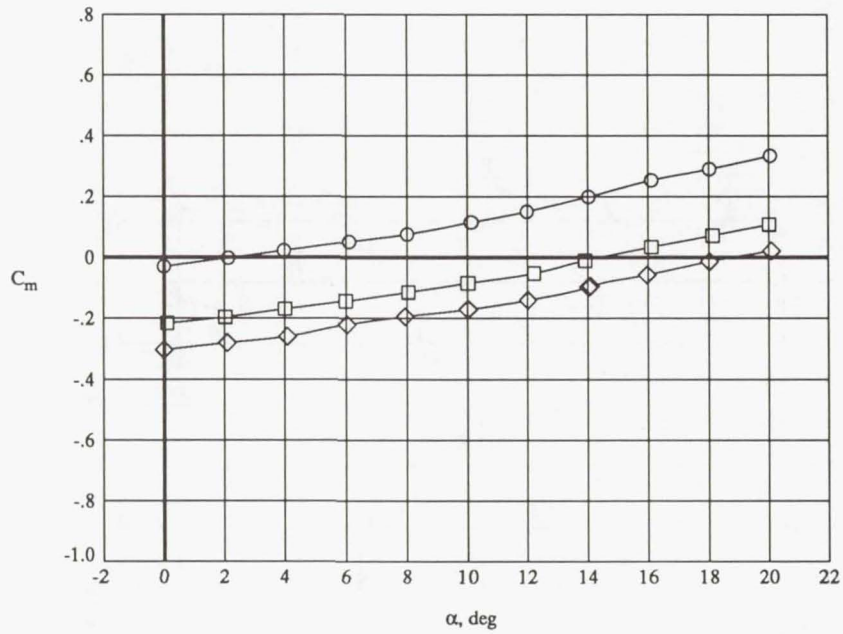
NPR

- 1.0
- 2.5
- ◇ 3.5



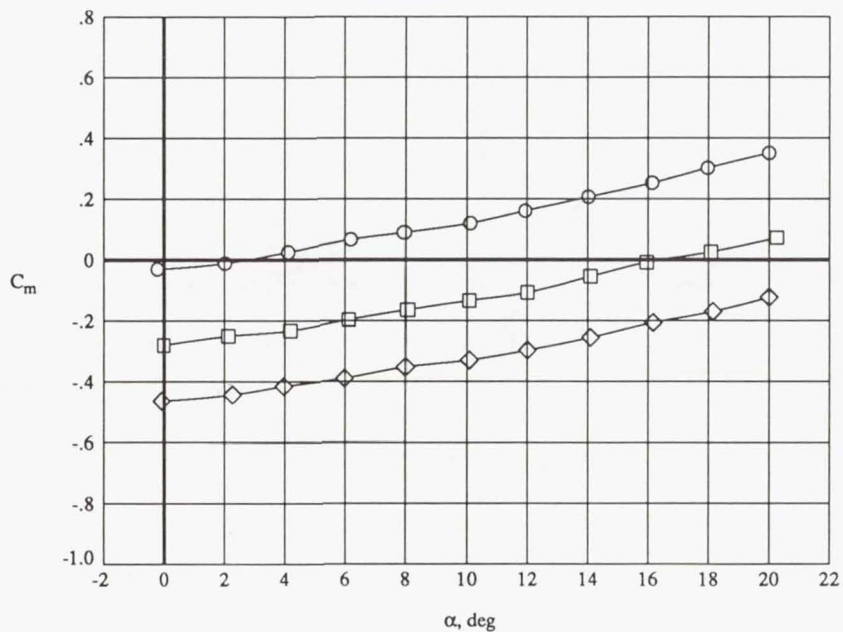
(b)  $\delta_N = 20^\circ L$ .

Figure 13. Continued.



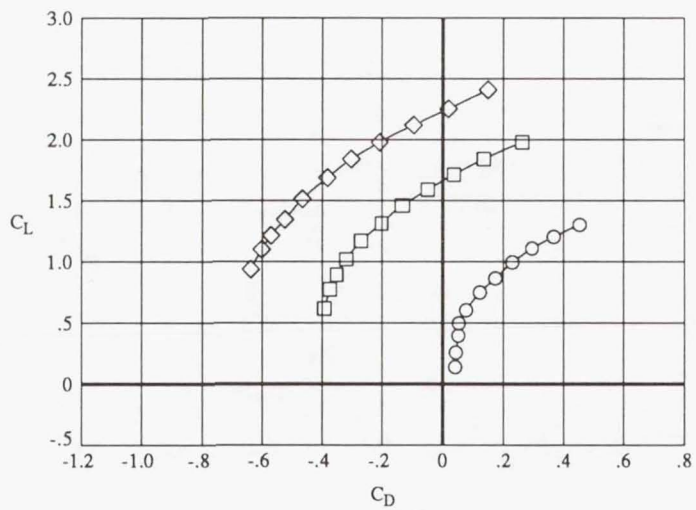
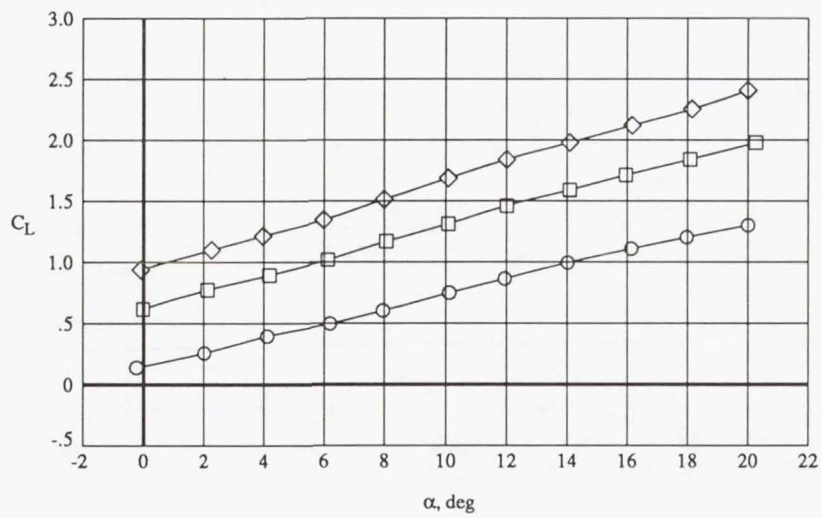
(c)  $\delta_N = 40^\circ L$ .

Figure 13. Continued.



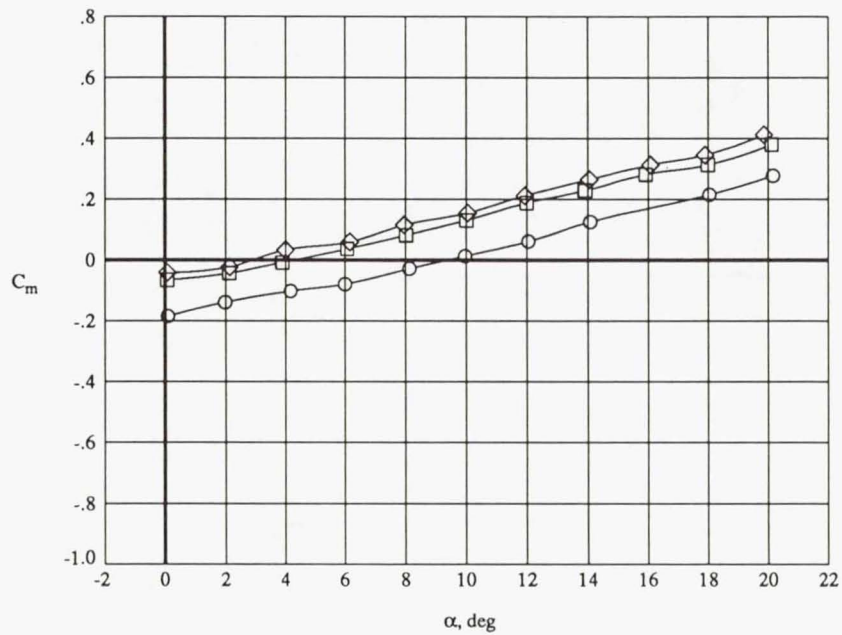
NPR

- 1.0
- 2.5
- ◇ 3.5



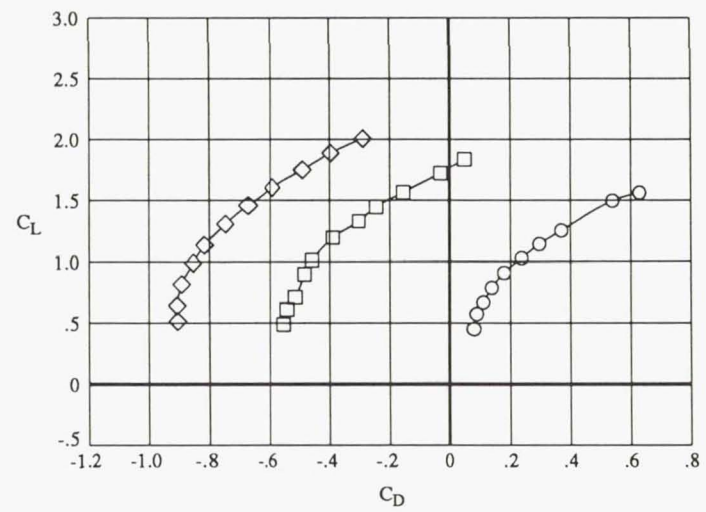
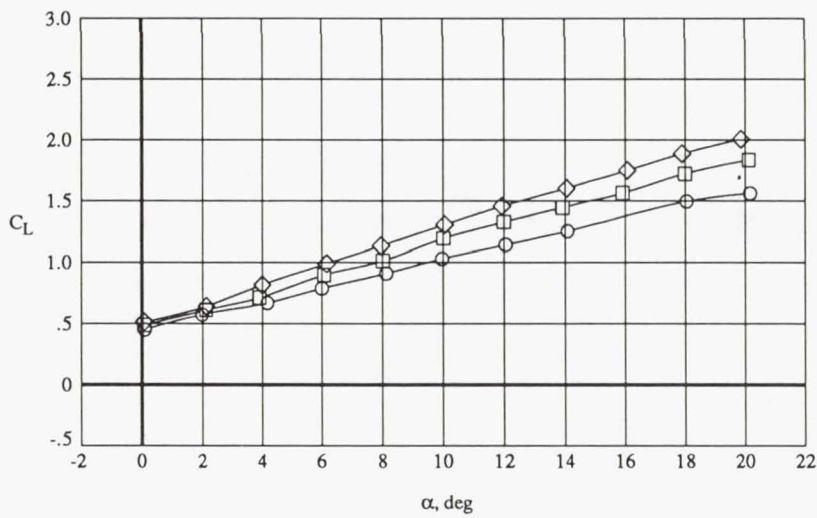
(d)  $\delta_N = 50^\circ L$ .

Figure 13. Concluded.



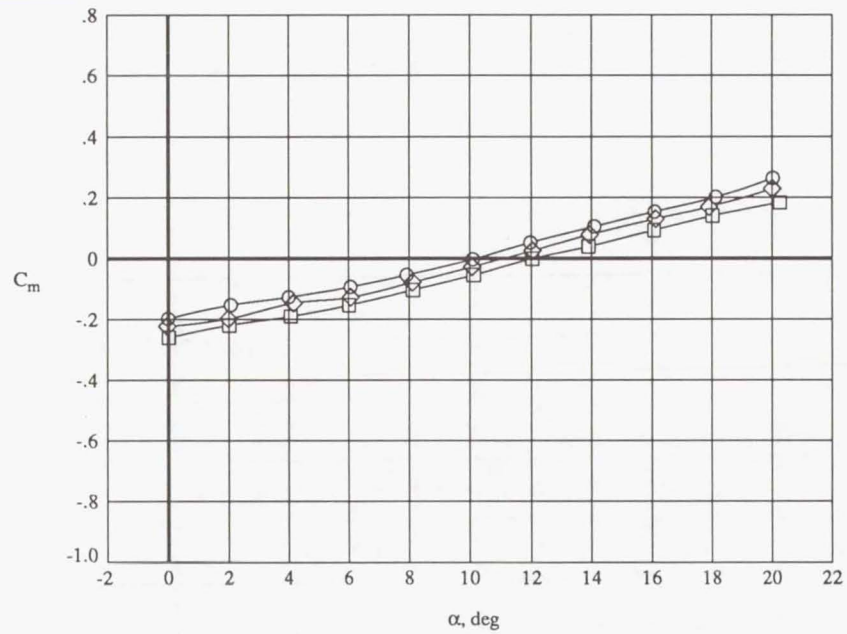
NPR

- 1.0
- 2.5
- ◇ 3.5



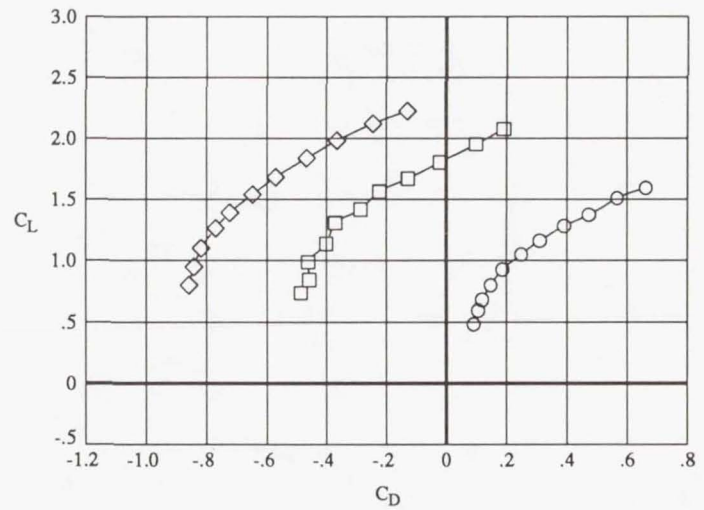
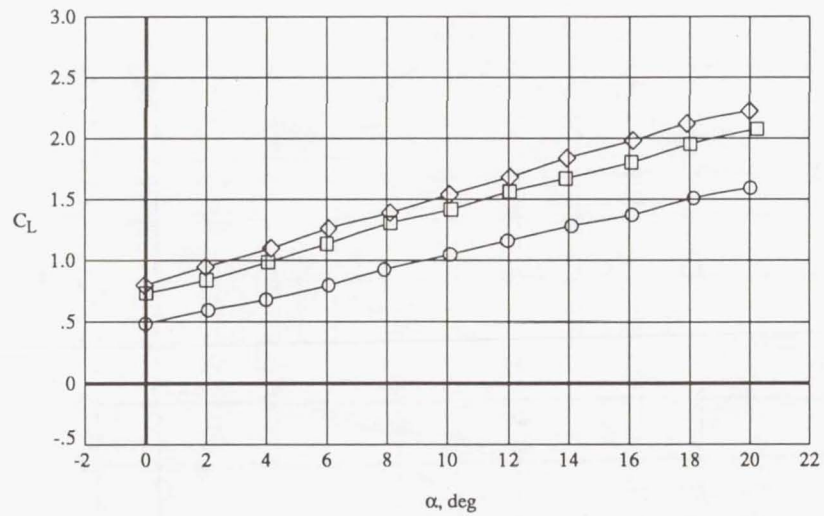
(a)  $\delta_N = 0^\circ L$ .

Figure 14. Effects of NPR on longitudinal aerodynamic characteristics of ALBEN concept with  $\delta_f = 20^\circ$ .



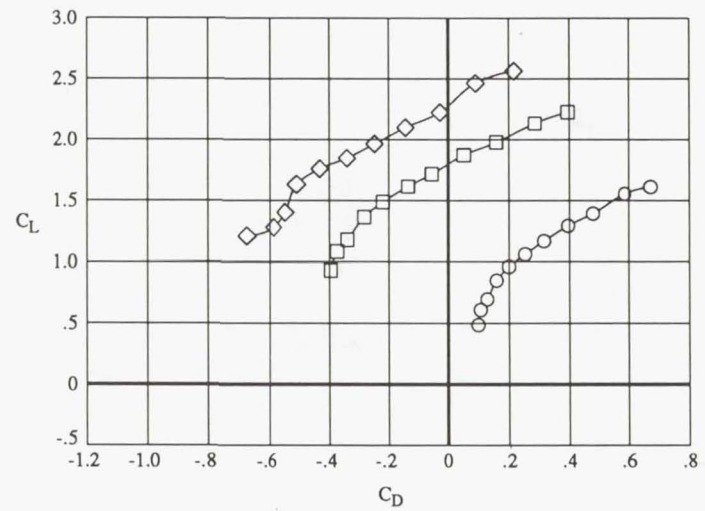
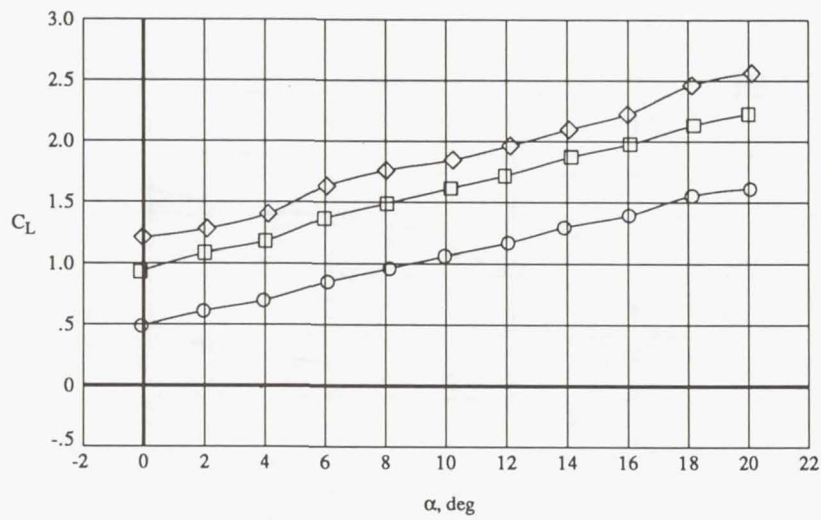
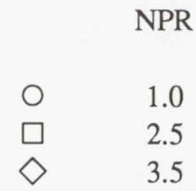
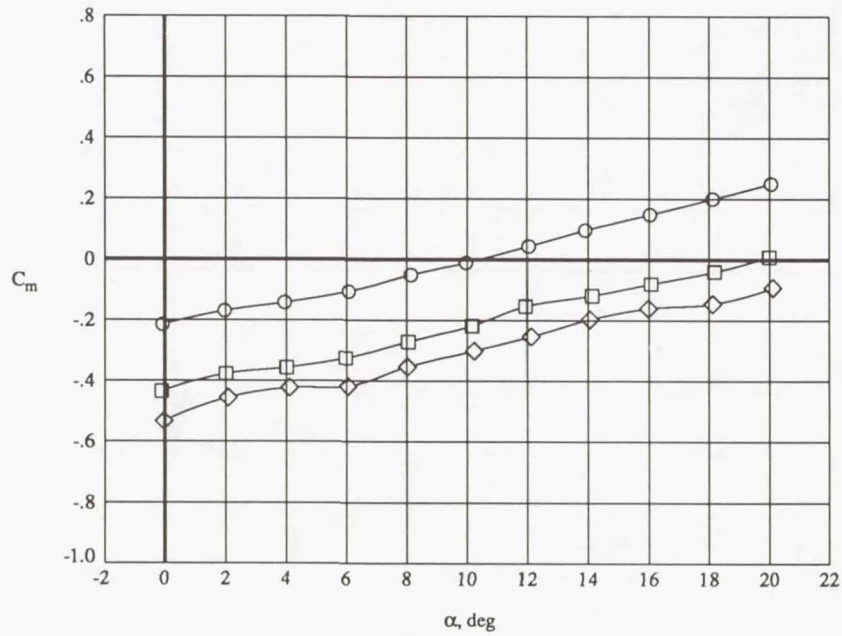
NPR

- 1.0
- 2.5
- ◇ 3.5



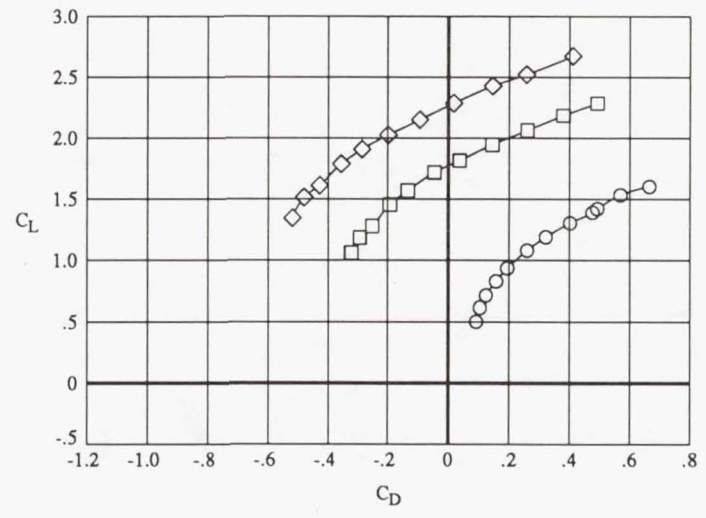
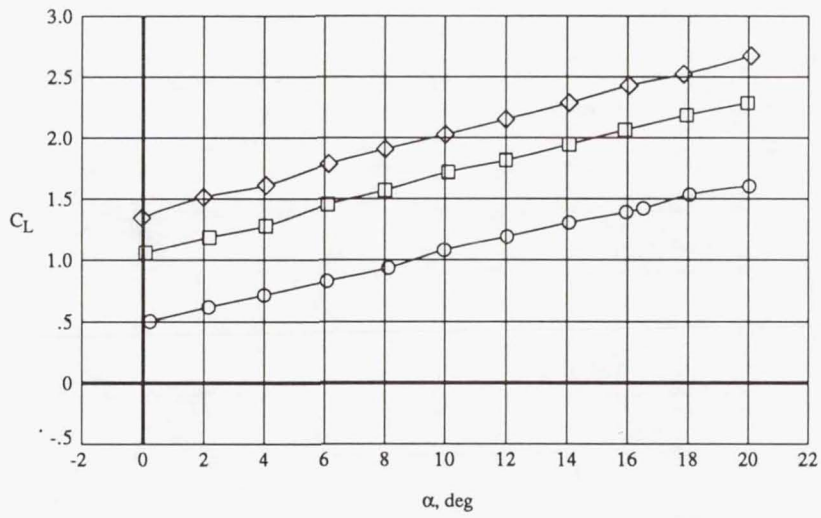
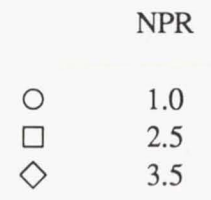
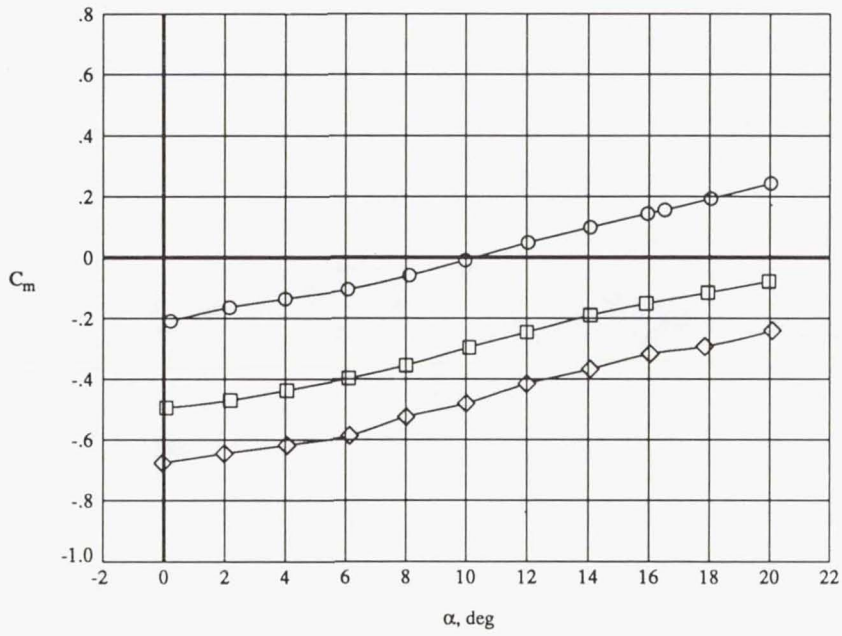
(b)  $\delta_N = 20^\circ L$ .

Figure 14. Continued.



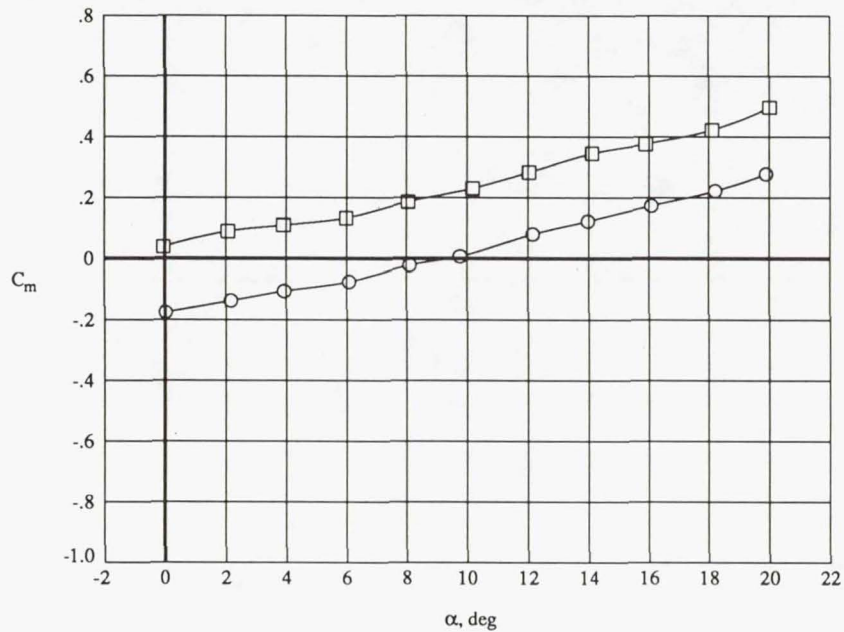
(c)  $\delta_N = 40^\circ L$ .

Figure 14. Continued.

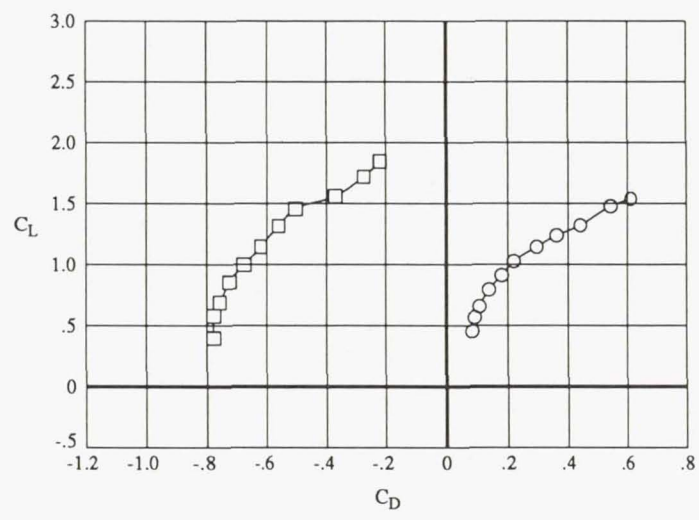
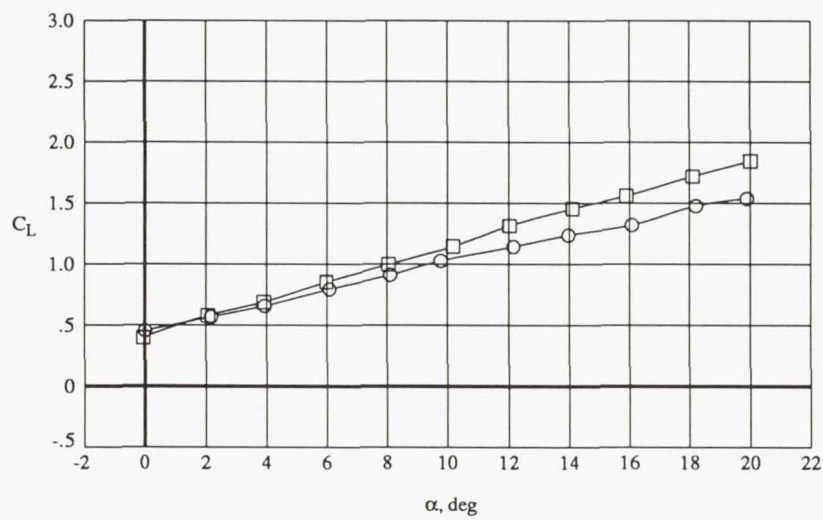


(d)  $\delta_N = 50^\circ L$ .

Figure 14. Continued.

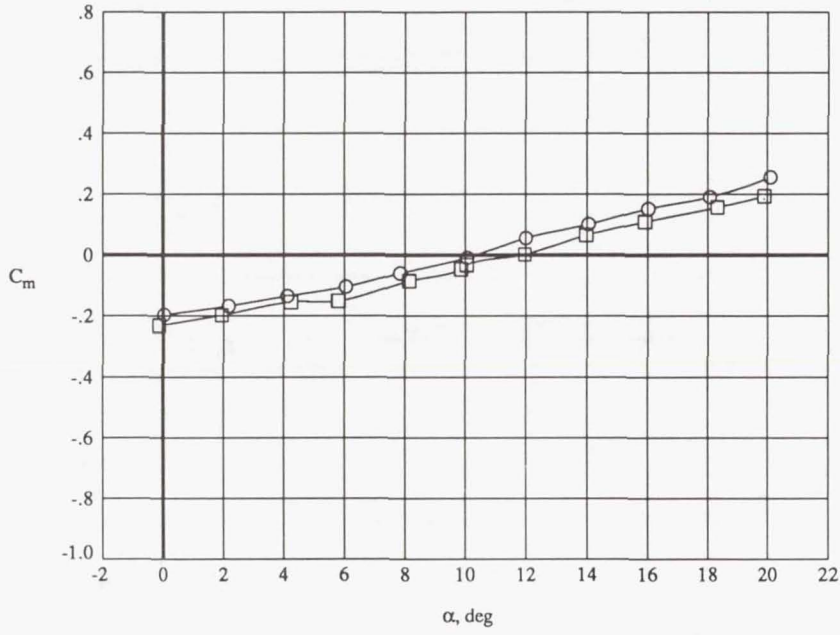


NPR  
 ○ 1.0  
 □ 2.5



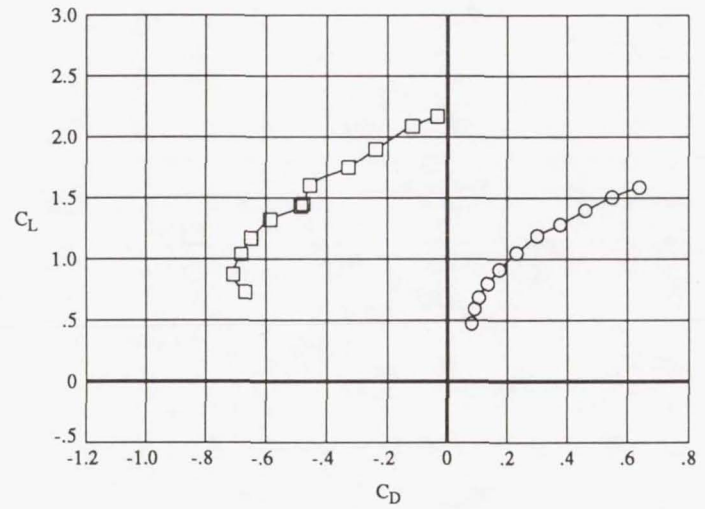
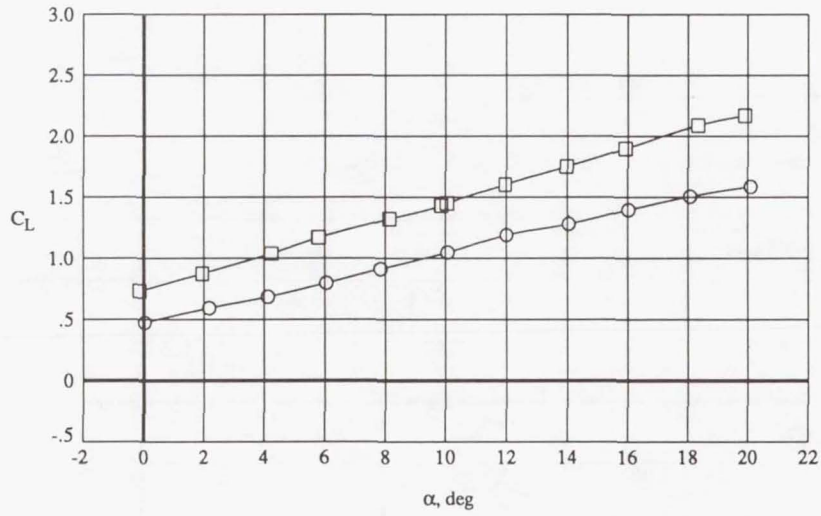
(e)  $\delta_N = 0^\circ T$ .

Figure 14. Continued.



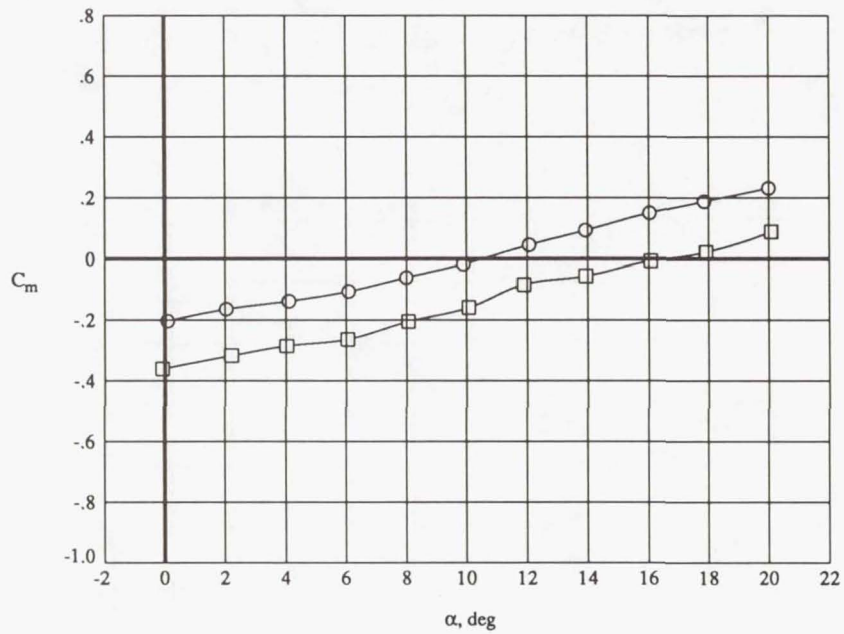
NPR

- 1.0
- 2.5



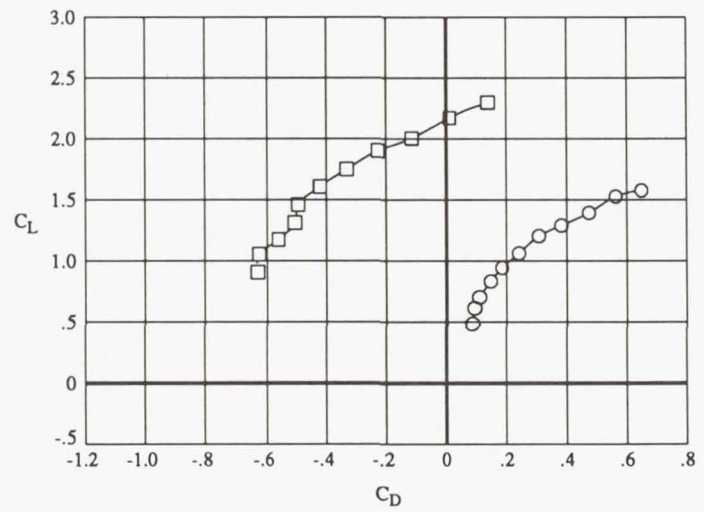
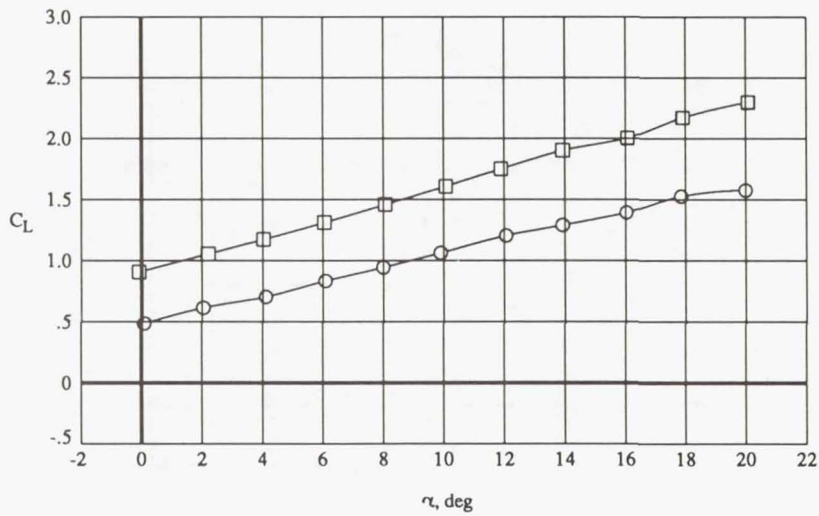
(f)  $\delta_N = 20^\circ T$ .

Figure 14. Continued.



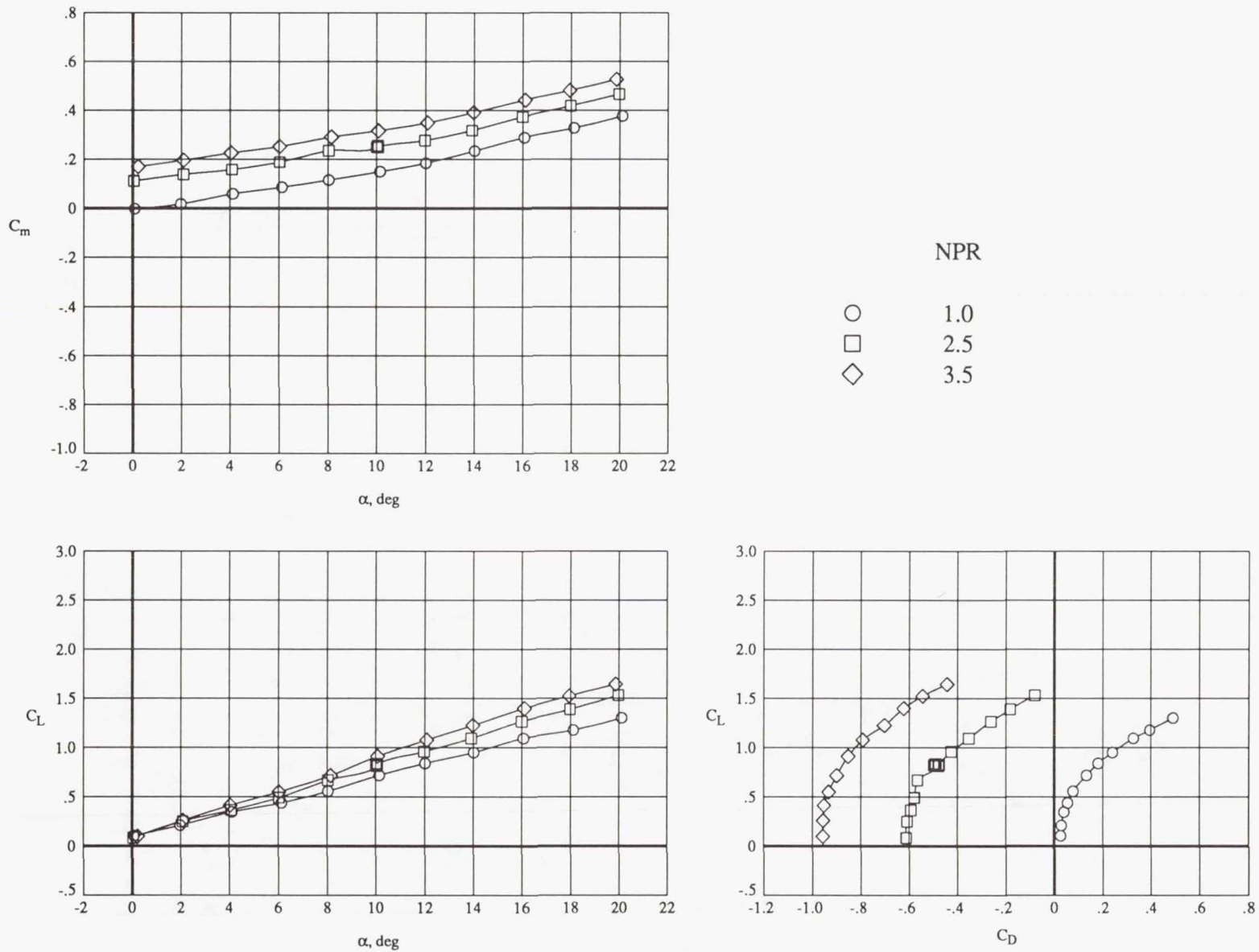
NPR

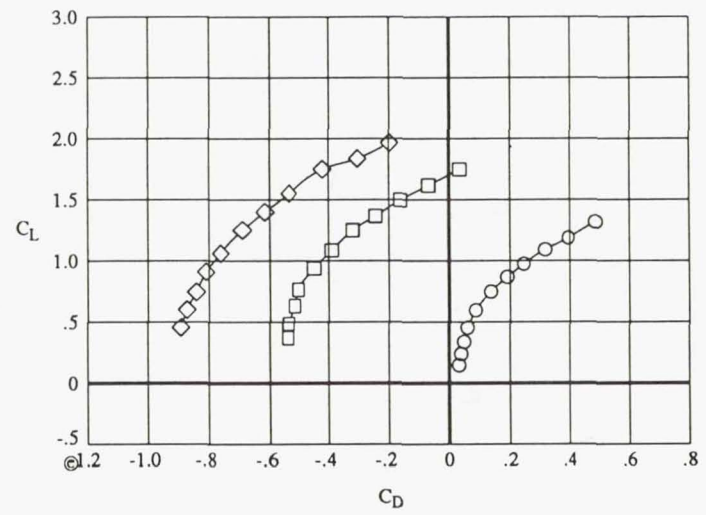
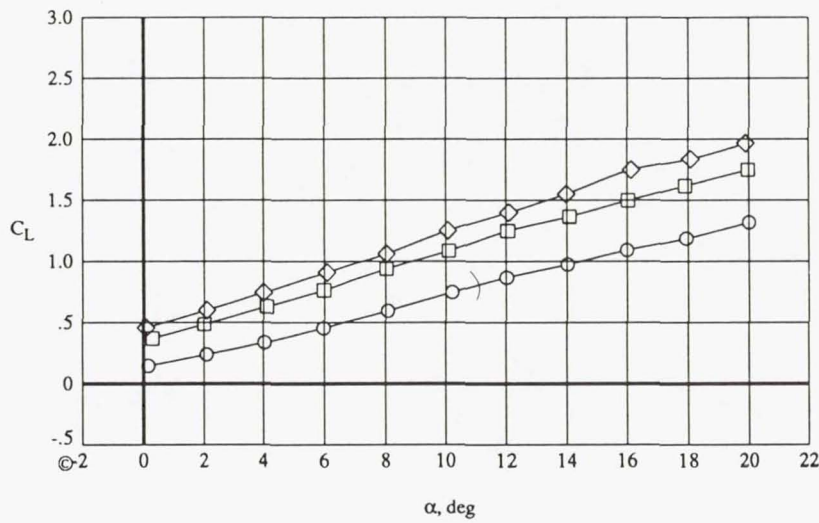
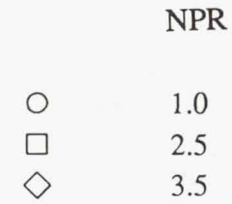
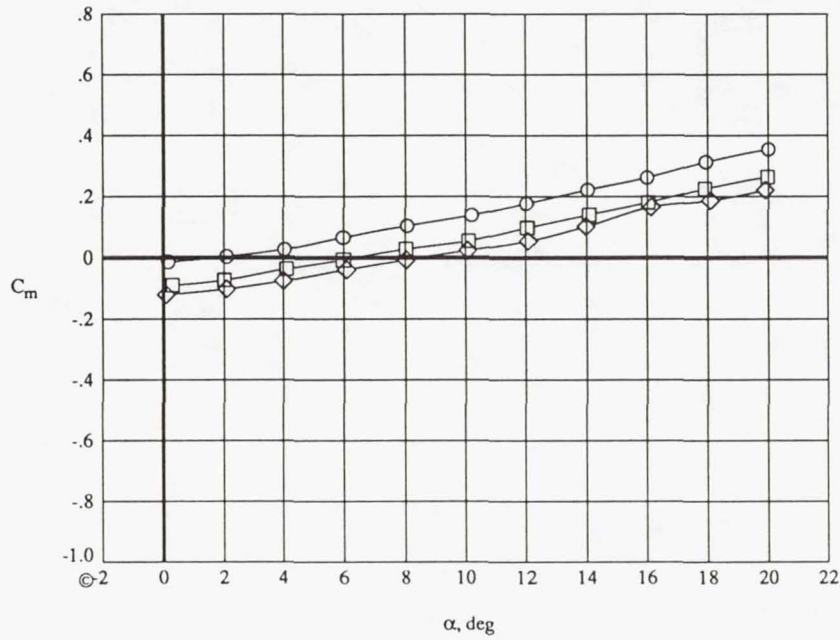
○ 1.0  
□ 2.5



(g)  $\delta_N = 30^\circ T$ .

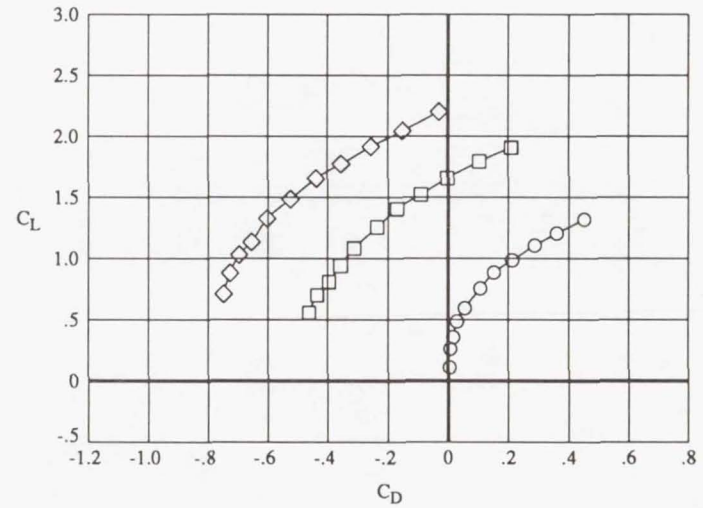
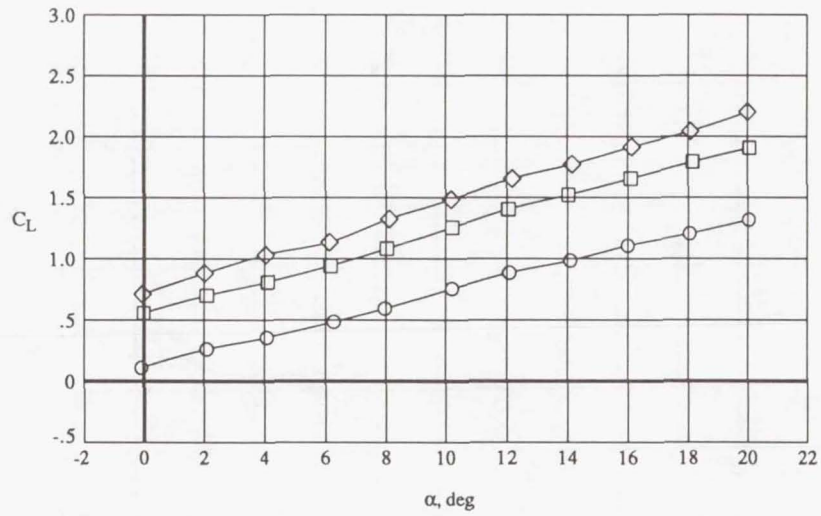
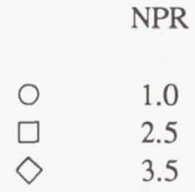
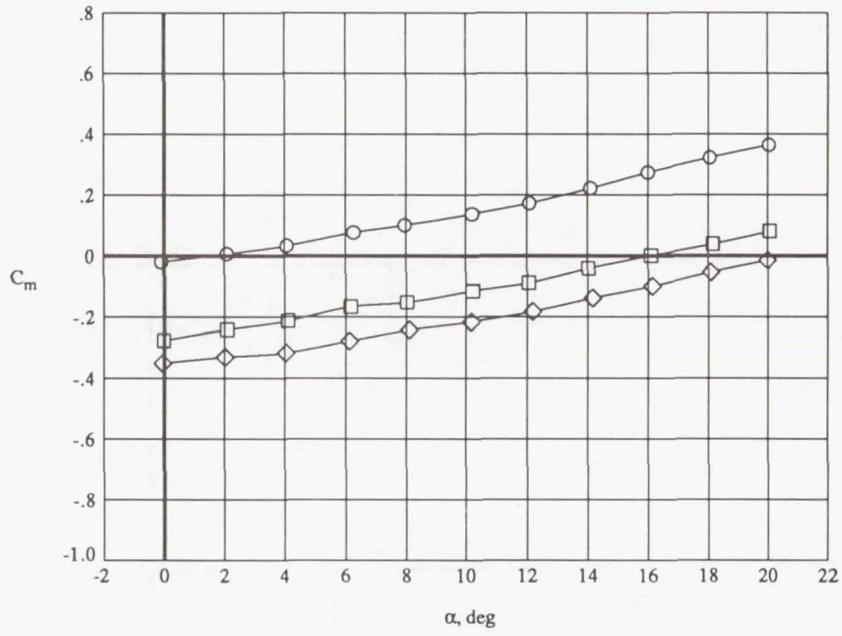
Figure 14. Concluded.

(a)  $\delta_N = 0^\circ L$ .Figure 15. Effects of NPR on longitudinal aerodynamic characteristics of LASERN concept with  $\delta_f = 0^\circ$ .



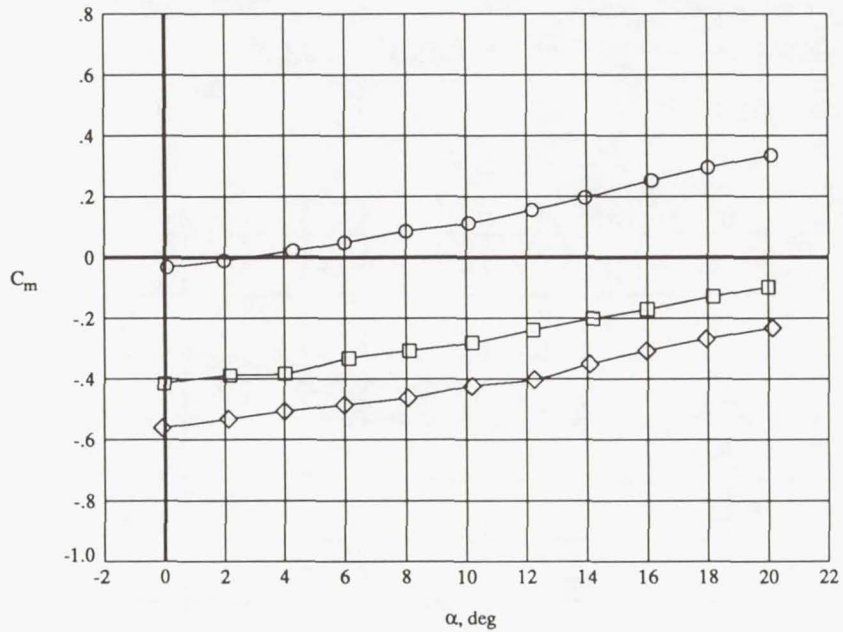
(b)  $\delta_N = 20^\circ L$ .

Figure 15. Continued.



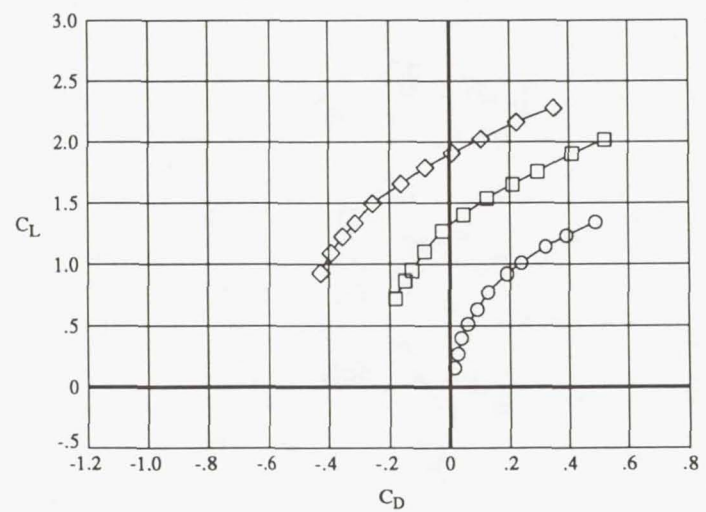
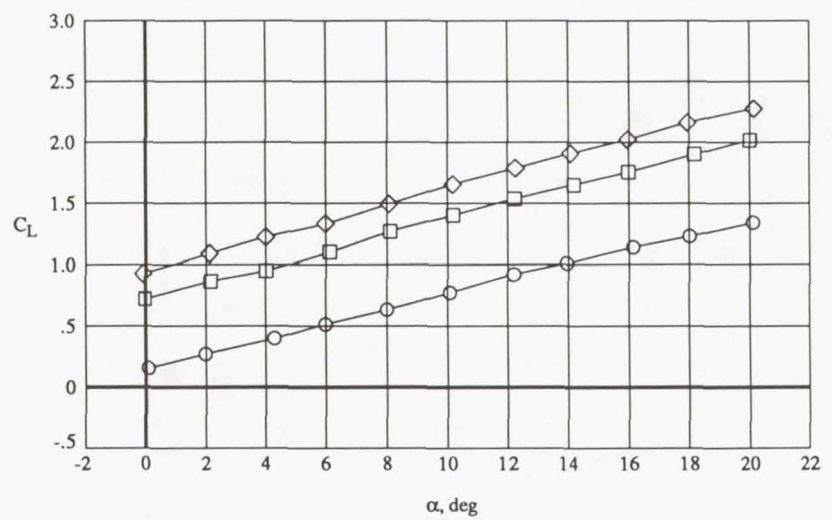
(c)  $\delta_N = 40^\circ L$ .

Figure 15. Continued.



NPR

- 1.0
- 2.5
- ◇ 3.5



(d)  $\delta_N = 60^\circ L$ .

Figure 15. Concluded.

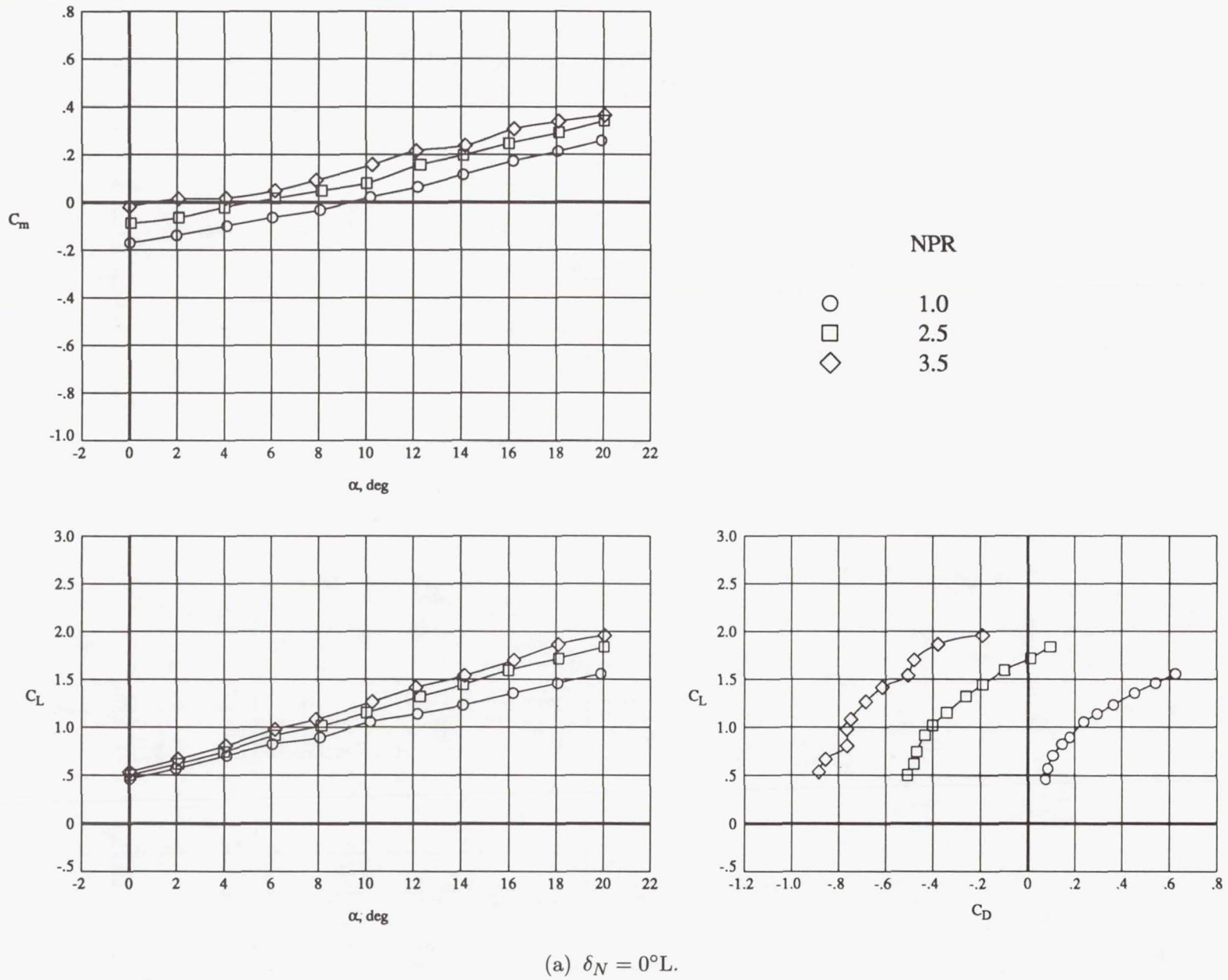
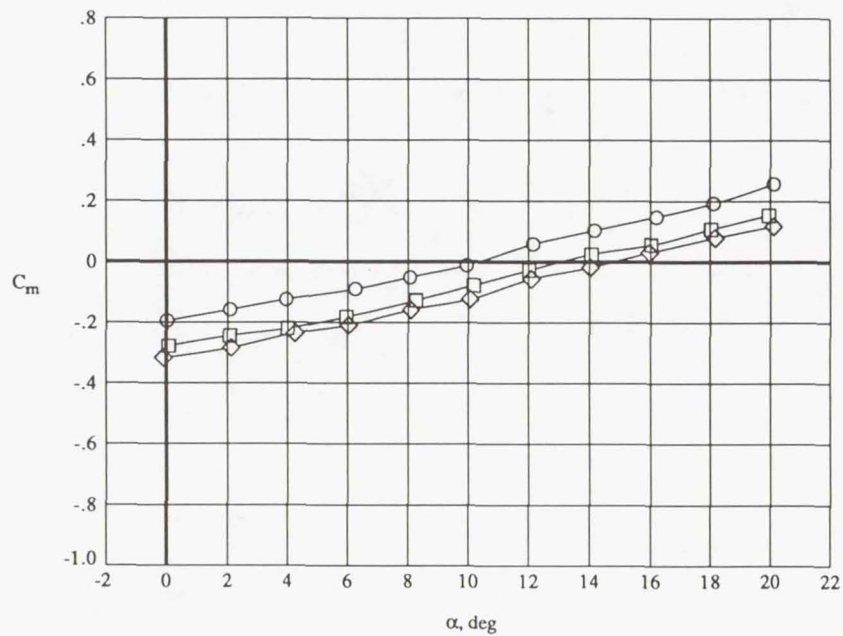
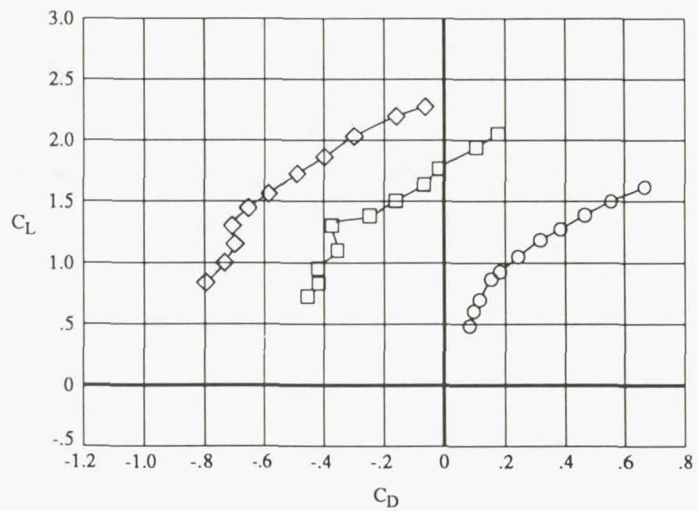
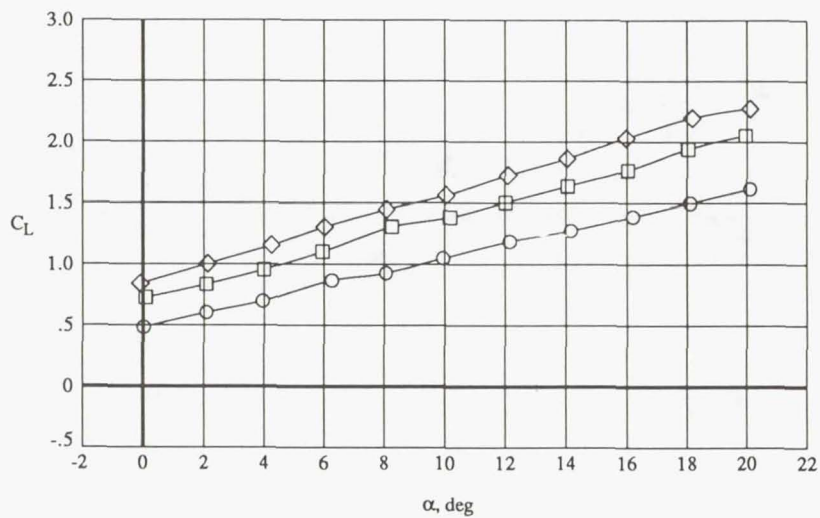


Figure 16. Effects of NPR on longitudinal aerodynamic characteristics of LASERN concept with  $\delta_f = 20^\circ$ .



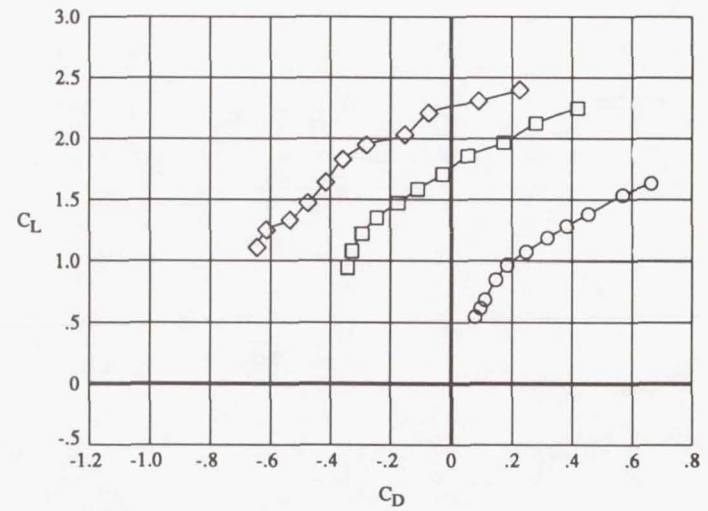
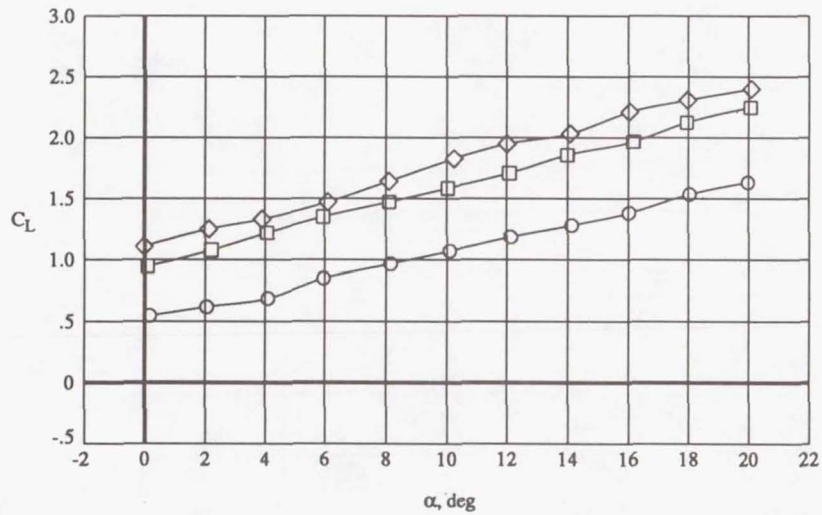
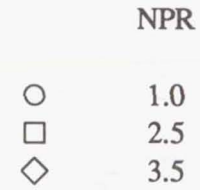
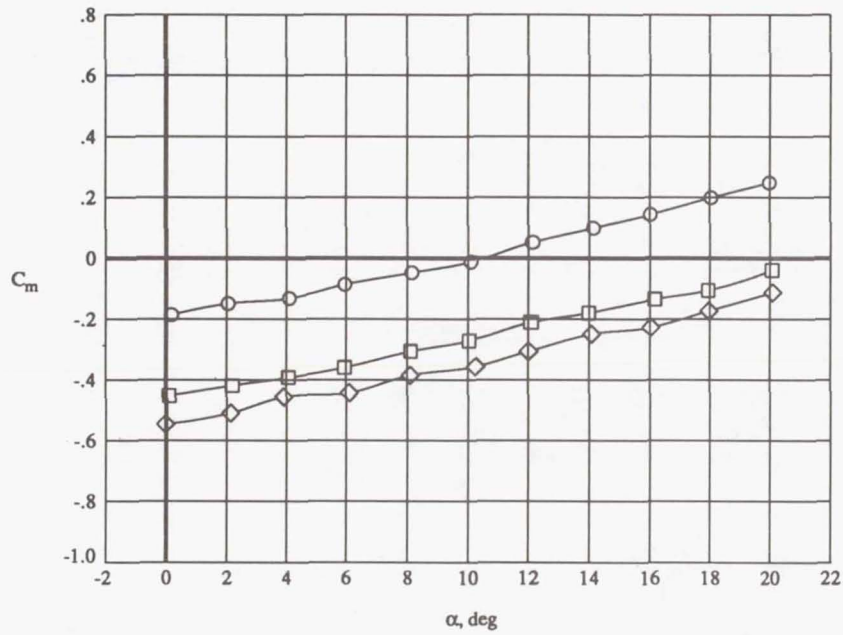
NPR

- 1.0
- 2.5
- ◇ 3.5



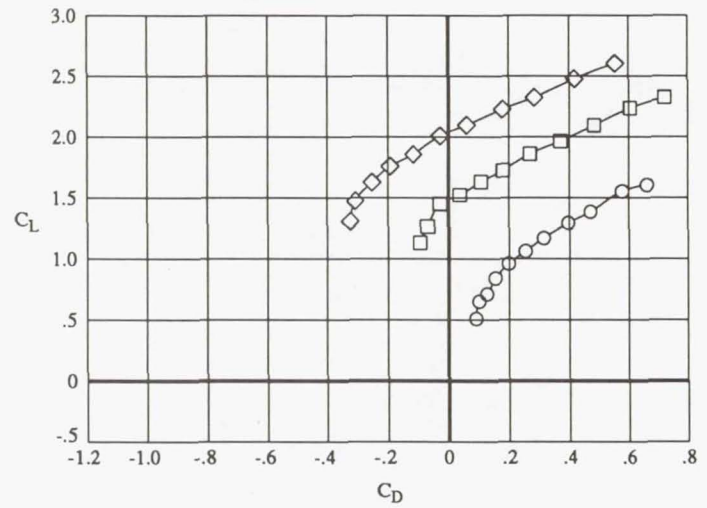
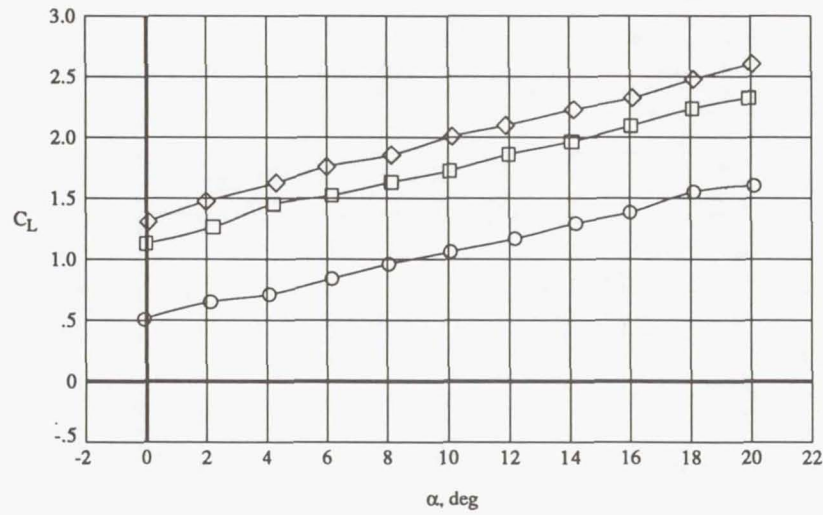
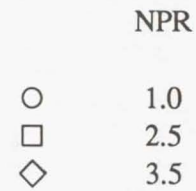
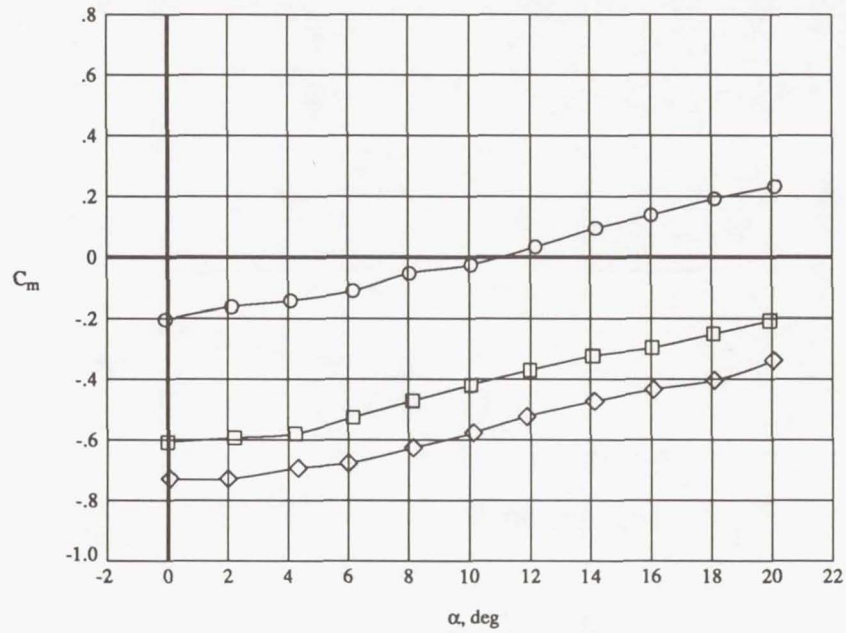
(b)  $\delta_N = 20^\circ L$ .

Figure 16. Continued.



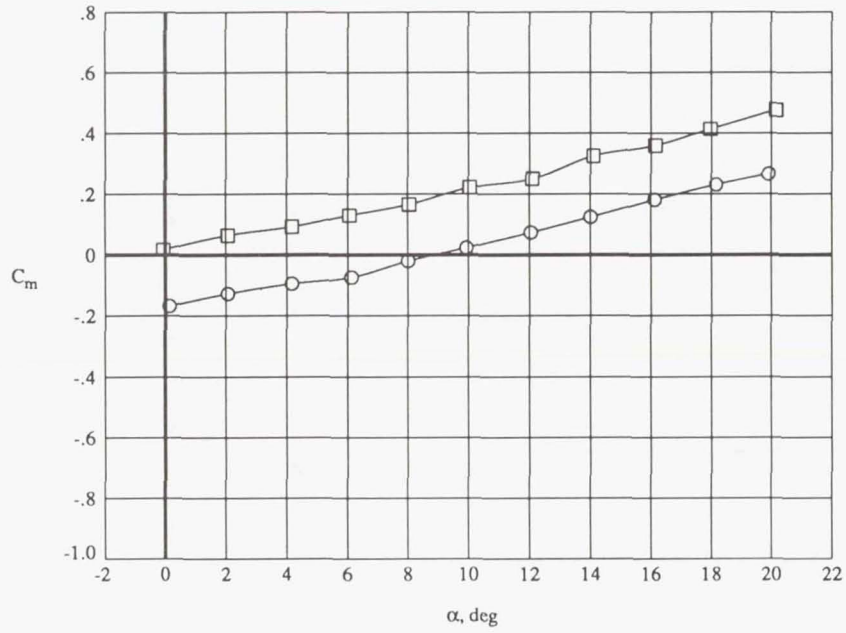
(c)  $\delta_N = 40^\circ L$ .

Figure 16. Continued.



(d)  $\delta_N = 60^\circ L$ .

Figure 16. Continued.



NPR

○ 1.0  
□ 2.5

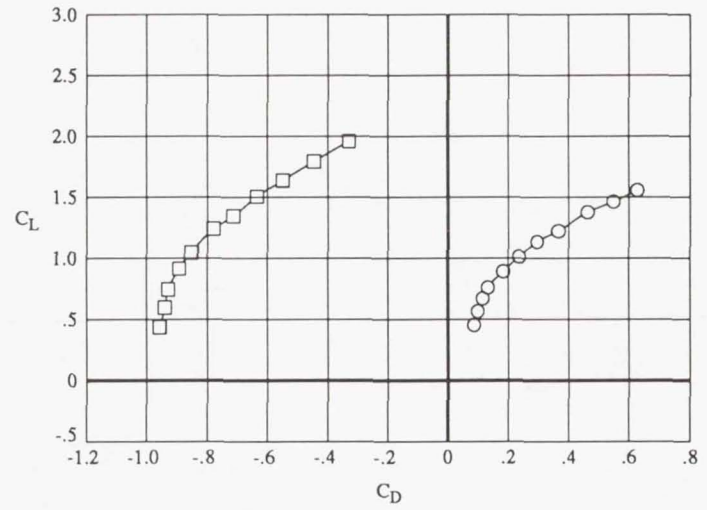
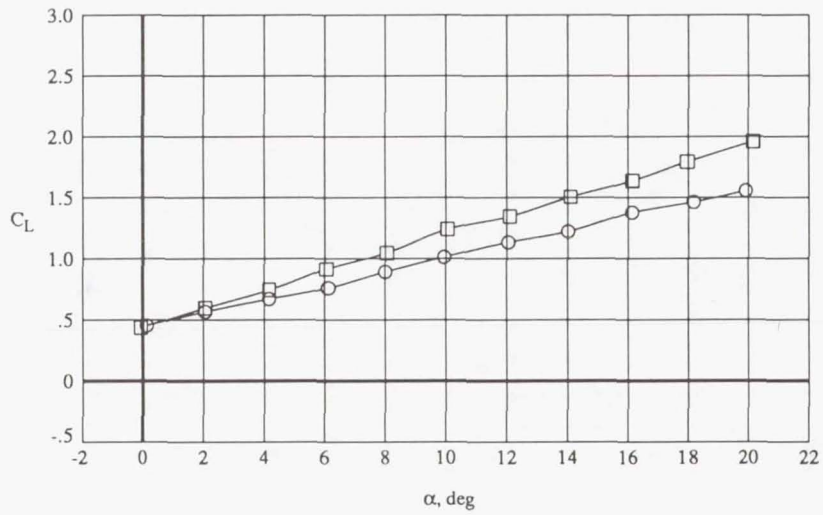
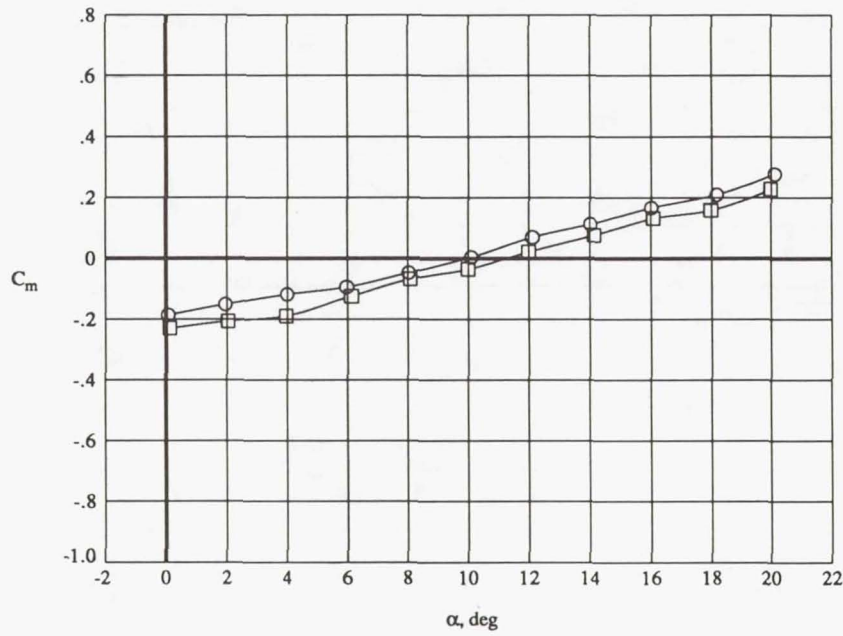
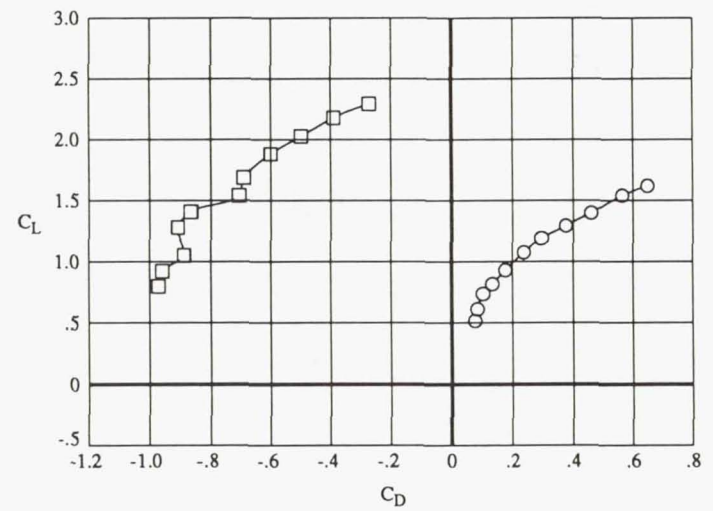
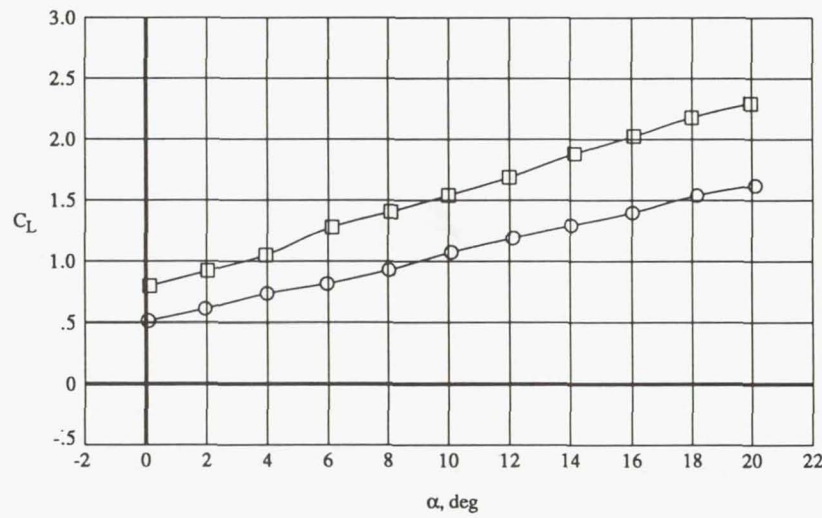
(e)  $\delta_N = 0^\circ T$ .

Figure 16. Continued.



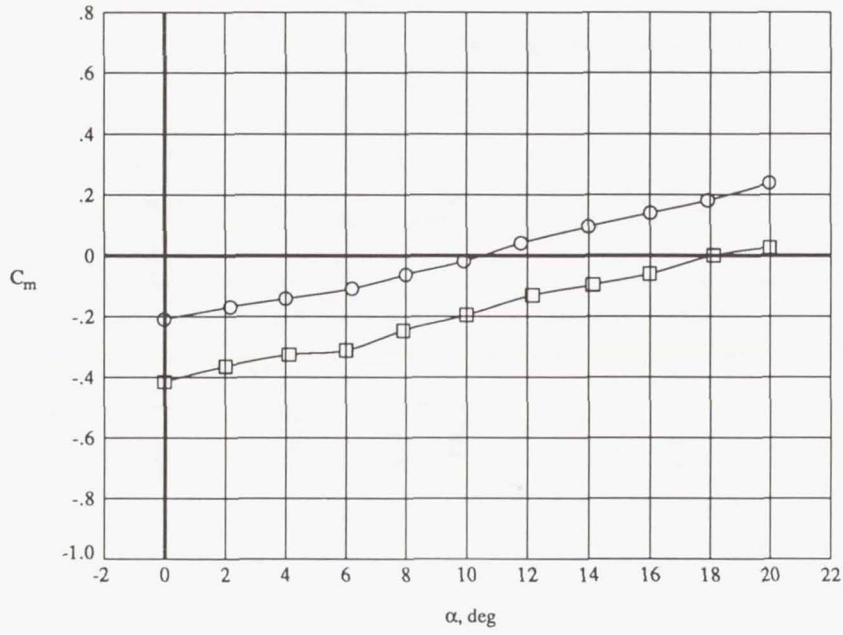
NPR

○ 1.0  
 □ 2.5

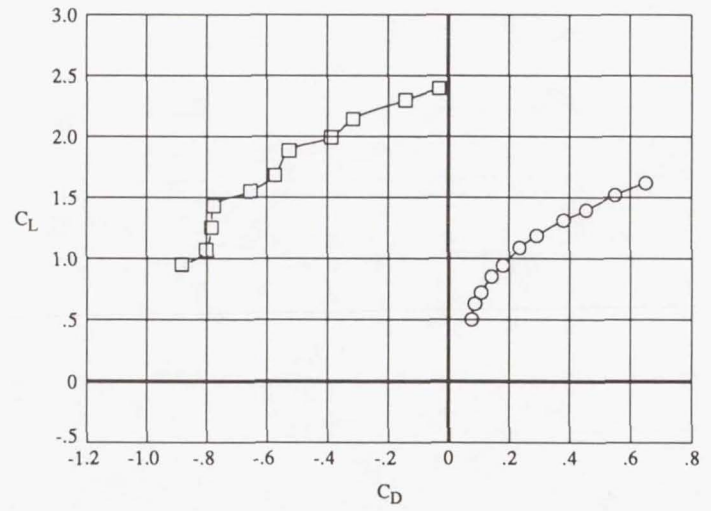
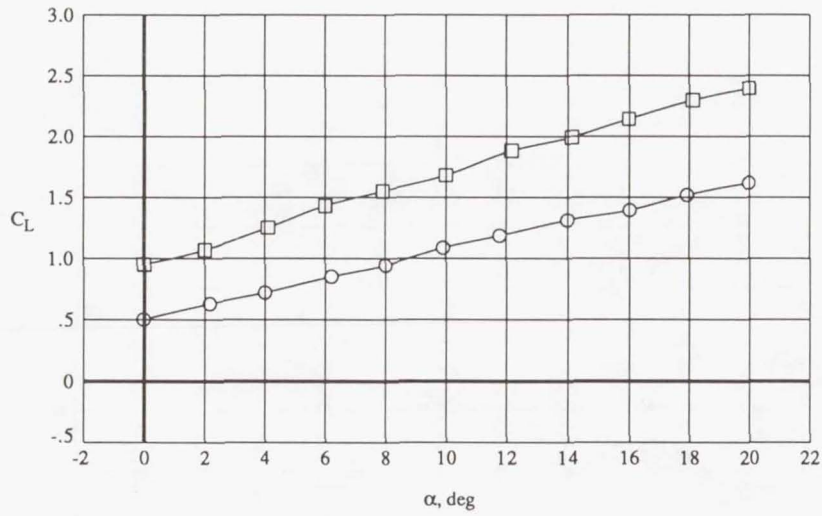


(f)  $\delta_N = 20^\circ T$ .

Figure 16. Continued.

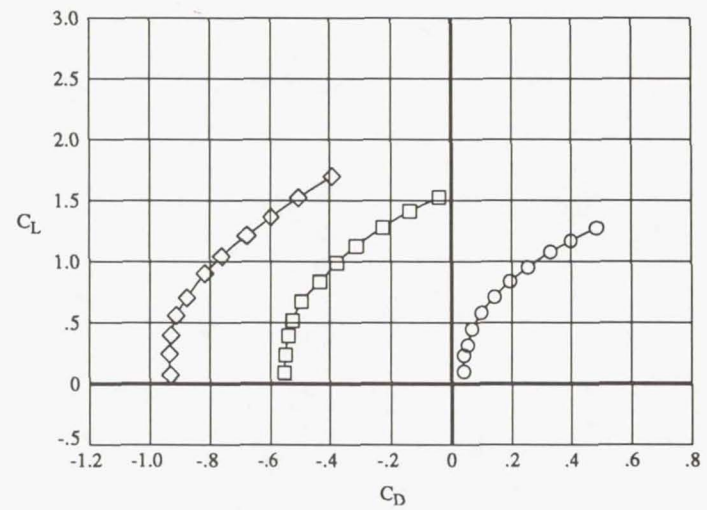
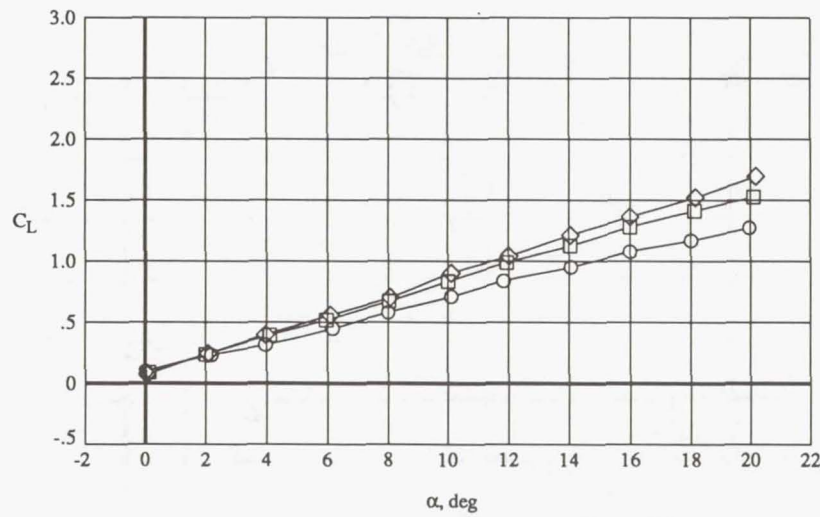
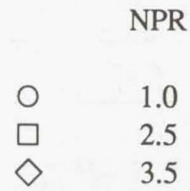
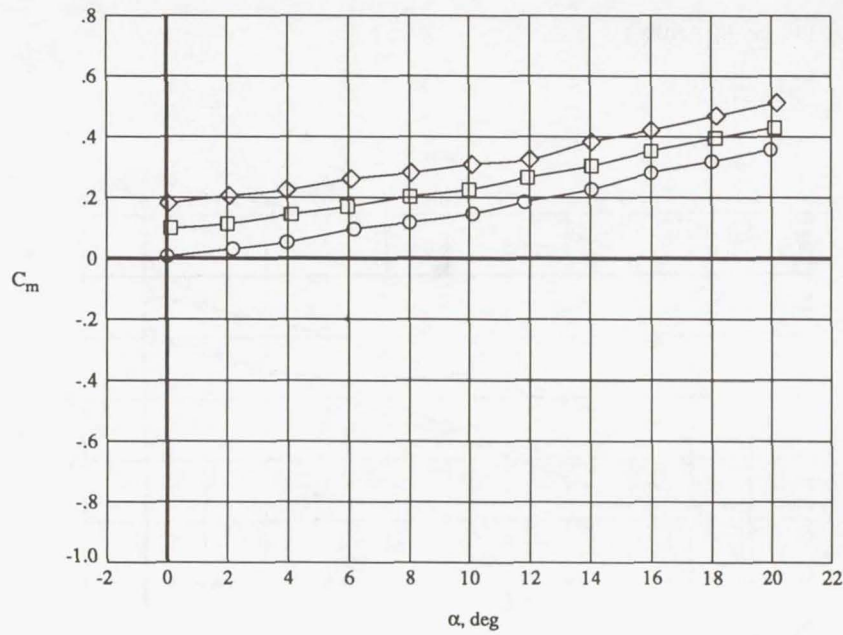


NPR  
 ○ 1.0  
 □ 2.5



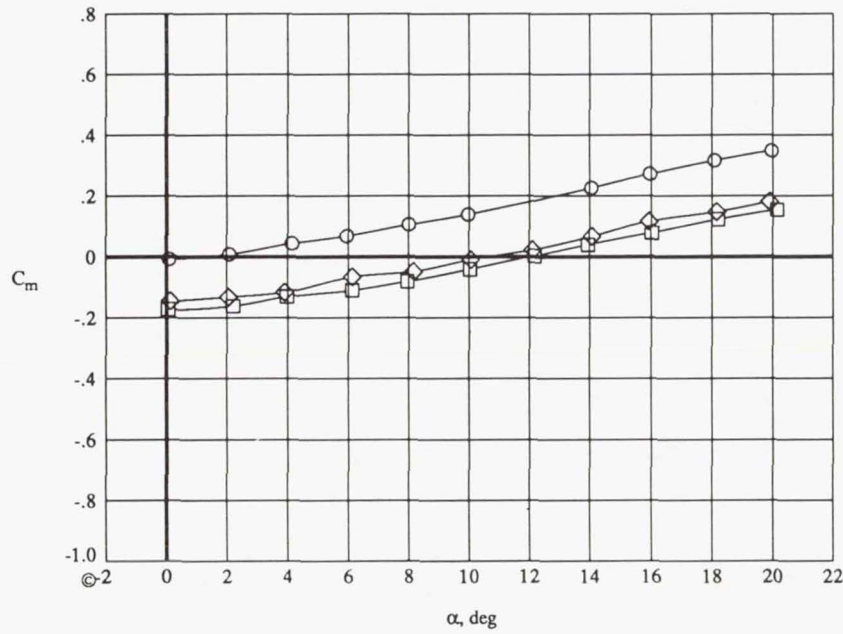
(g)  $\delta_N = 30^\circ T$ .

Figure 16. Concluded.

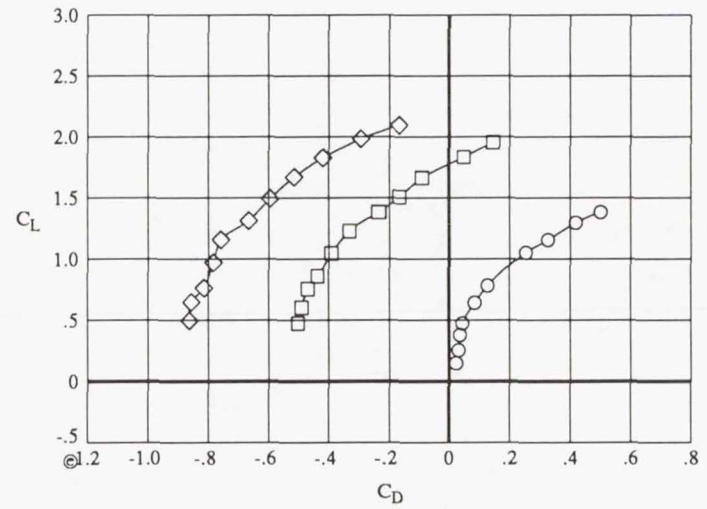
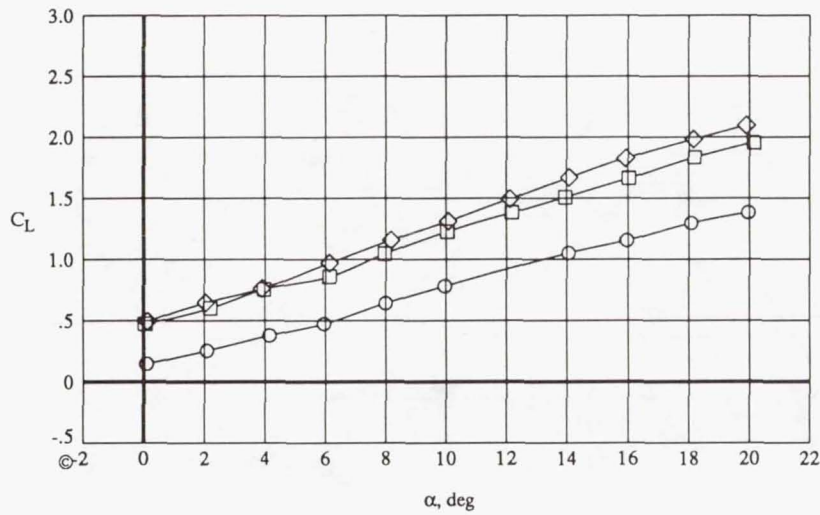


(a)  $\delta_N = 0^\circ L$ .

Figure 17. Effects of NPR on longitudinal aerodynamic characteristics of HASERN concept with  $\delta_f = 0^\circ$ .

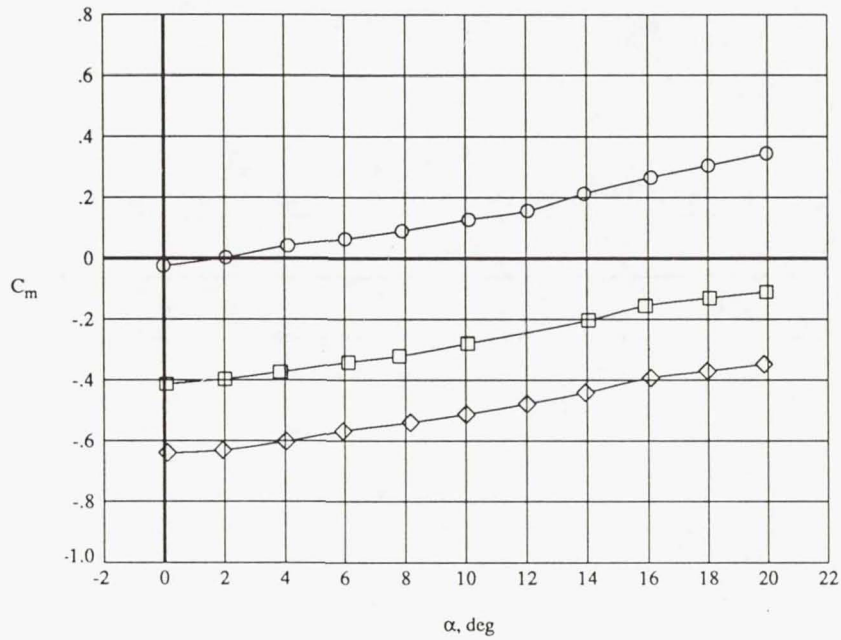


NPR  
 ○ 1.0  
 □ 2.5  
 ◇ 3.5



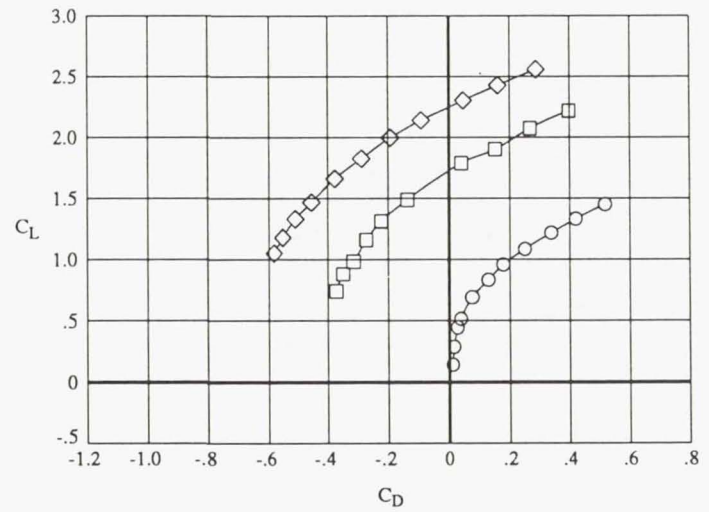
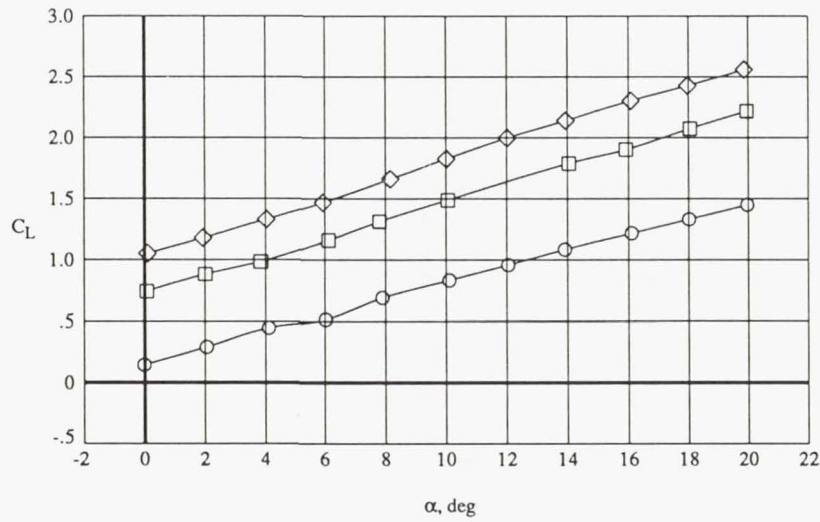
(b)  $\delta_N = 20^\circ L$ .

Figure 17. Continued.



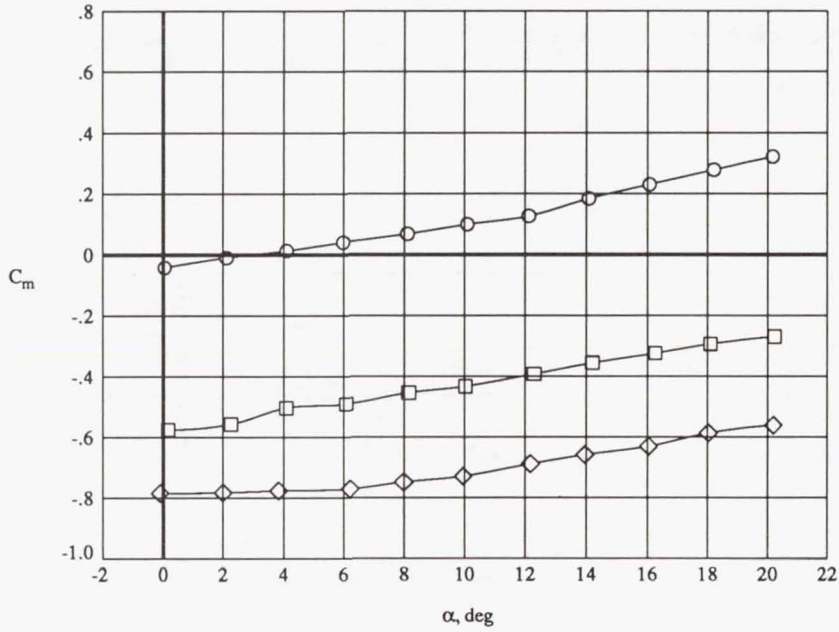
NPR

- 1.0
- 2.5
- ◇ 3.5

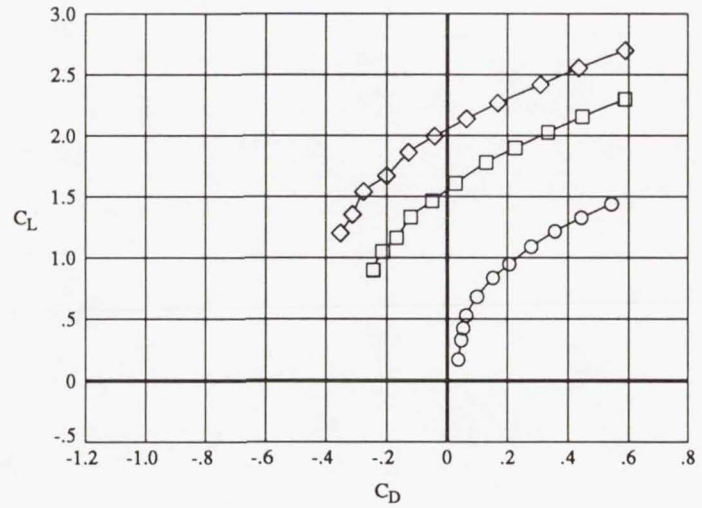
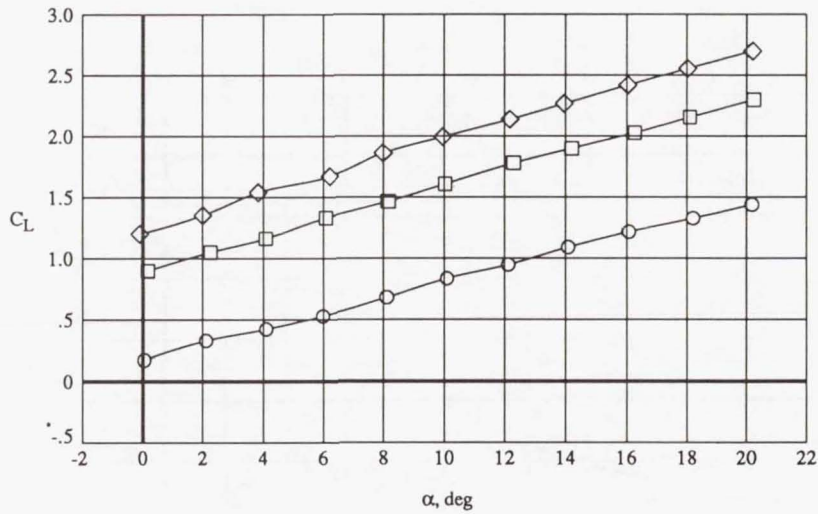


(c)  $\delta_N = 40^\circ L$ .

Figure 17. Continued.

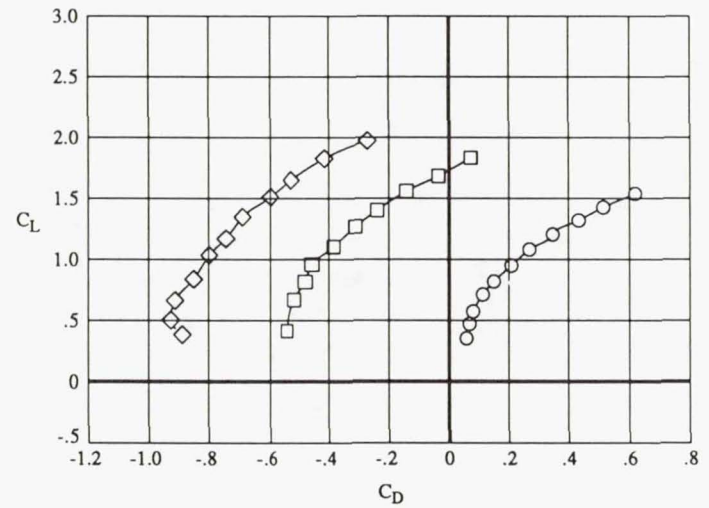
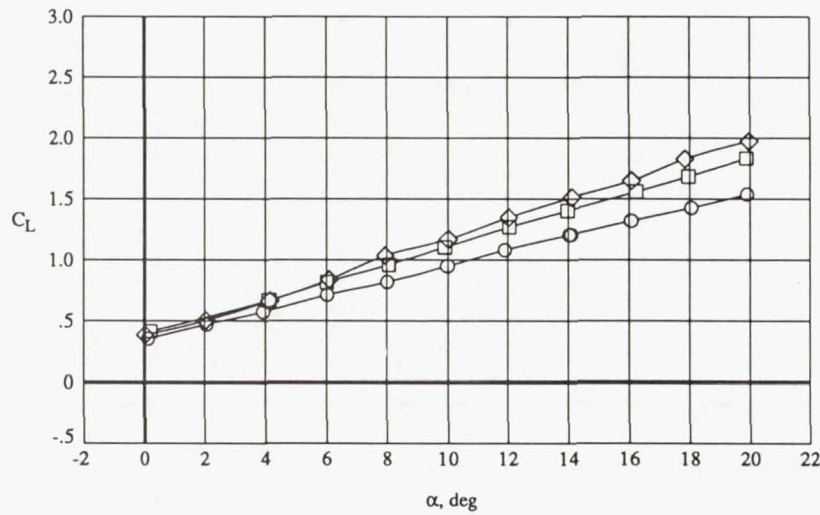
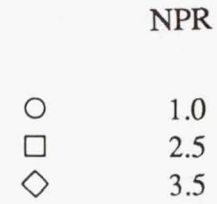
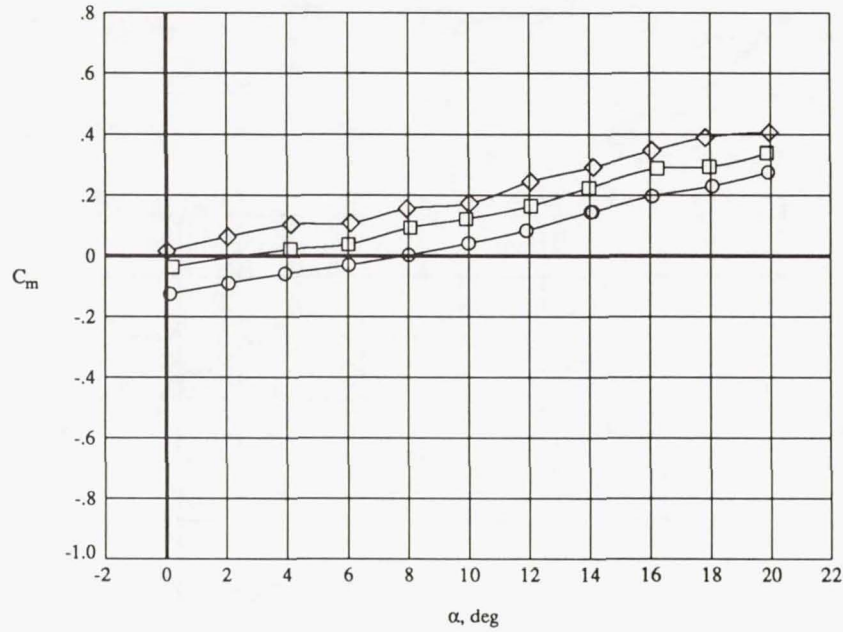


NPR  
 ○ 1.0  
 □ 2.5  
 ◇ 3.5



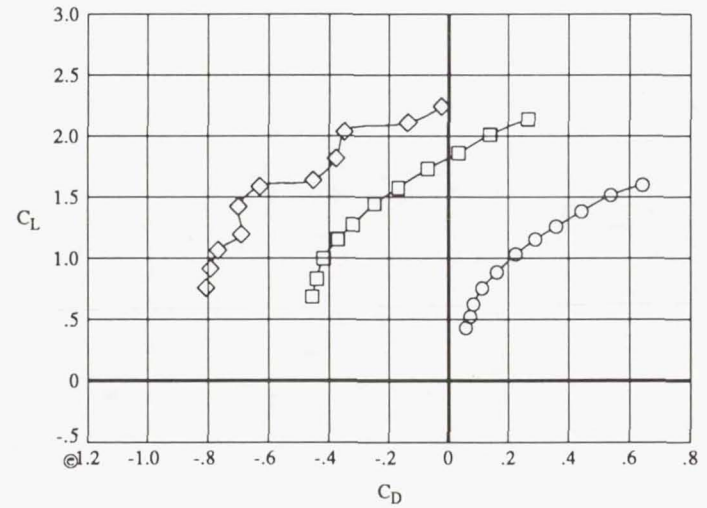
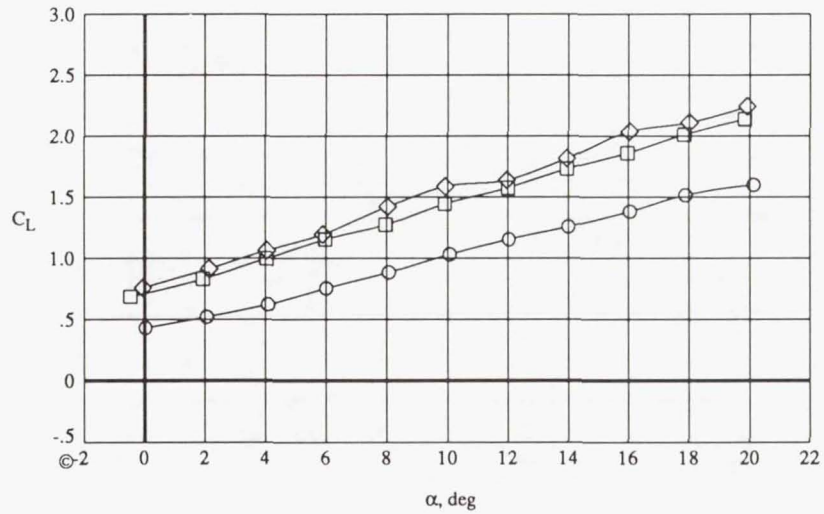
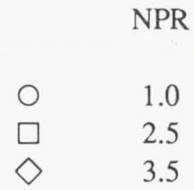
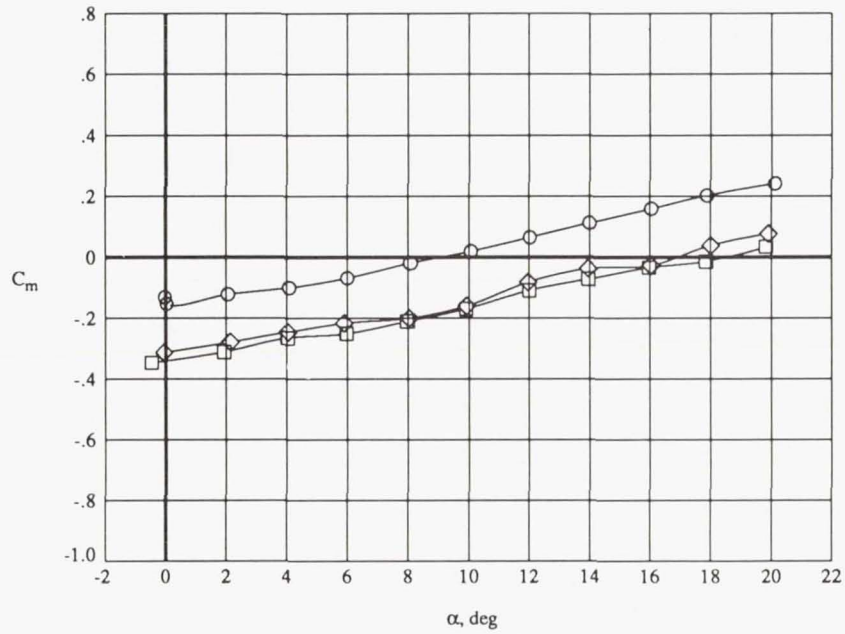
(d)  $\delta_N = 50^\circ L$ .

Figure 17. Concluded.



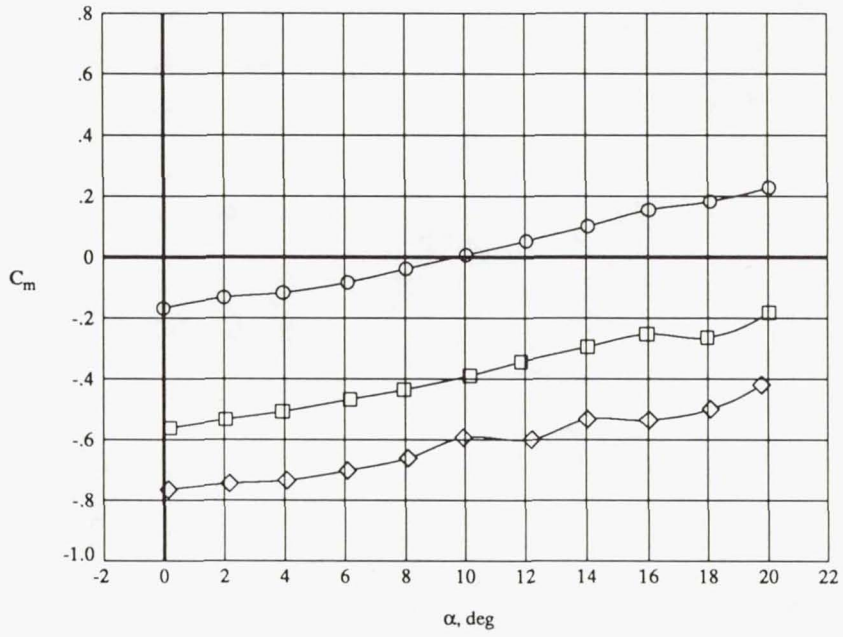
(a)  $\delta_N = 0^\circ L$ .

Figure 18. Effects of NPR on longitudinal aerodynamic characteristics of HASERN concept with  $\delta_f = 20^\circ$ .

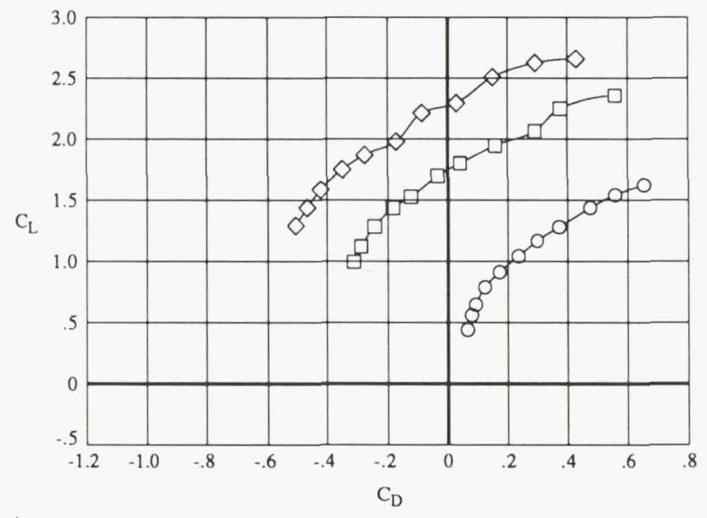
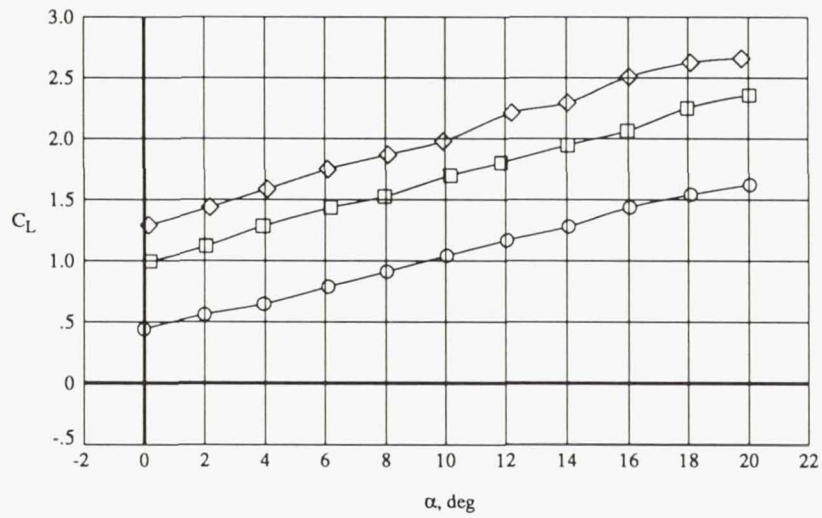


(b)  $\delta_N = 20^\circ L$ .

Figure 18. Continued.

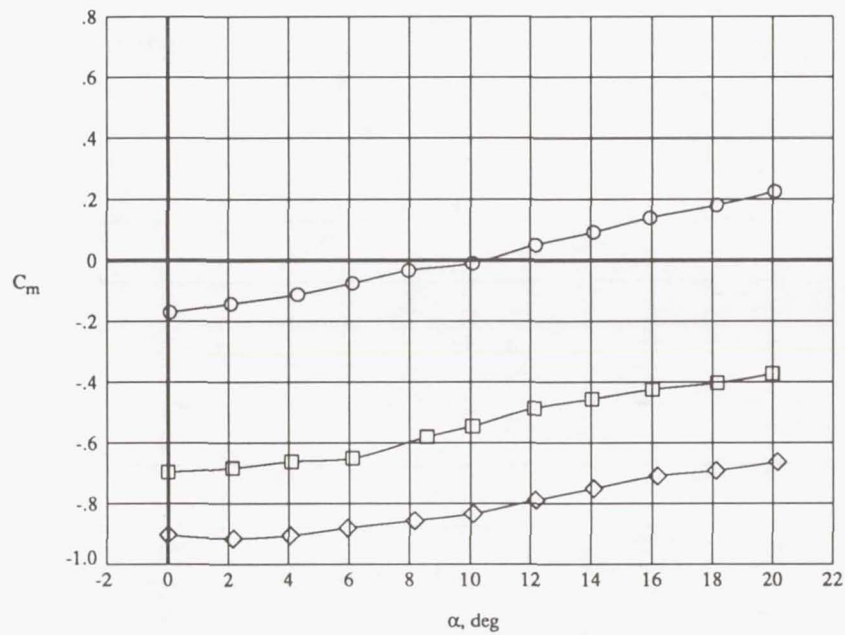


NPR  
 ○ 1.0  
 □ 2.5  
 ◇ 3.5



(c)  $\delta_N = 40^\circ L$ .

Figure 18. Continued.



NPR

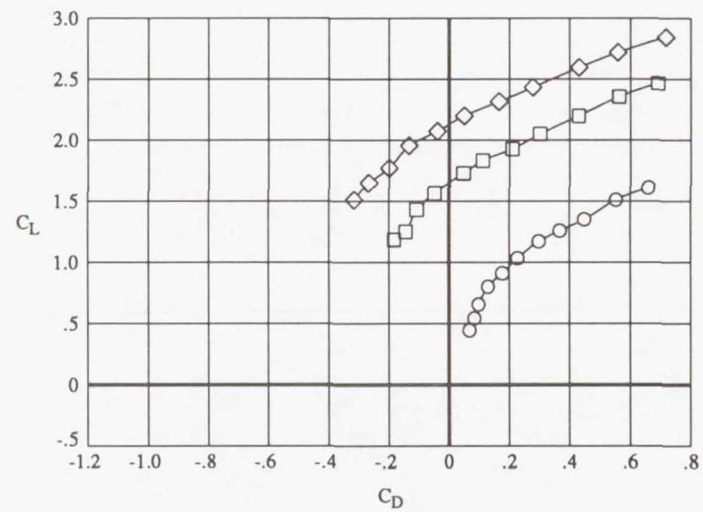
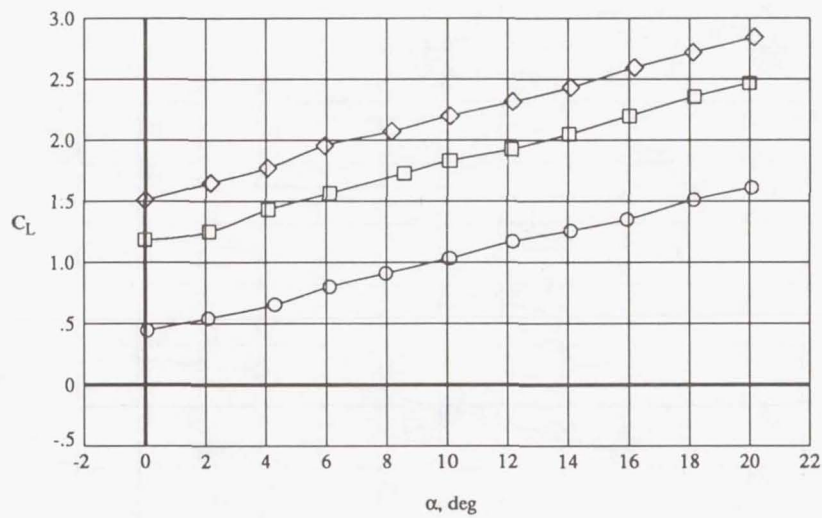
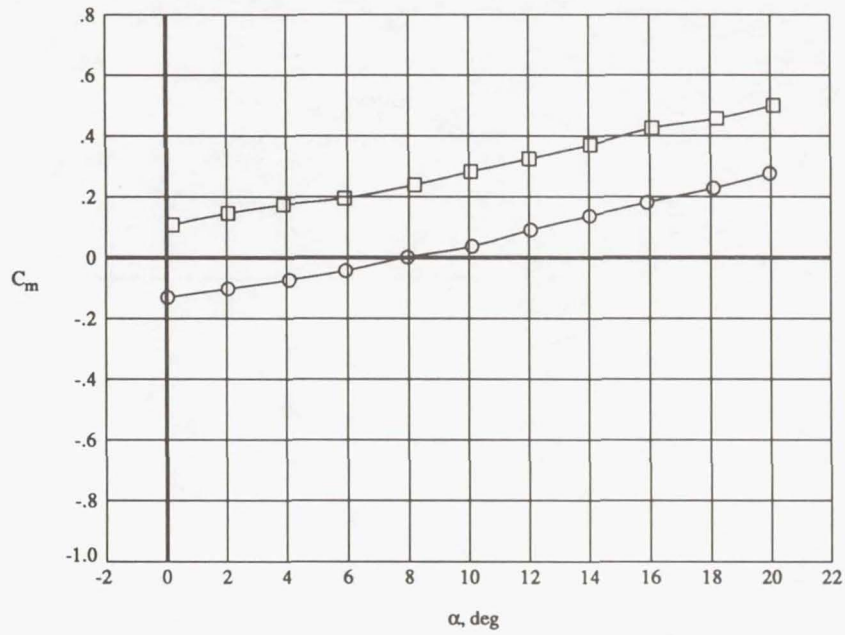
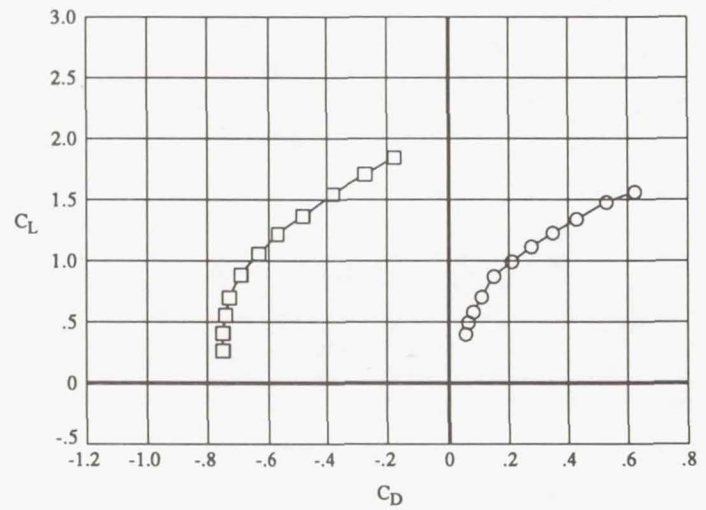
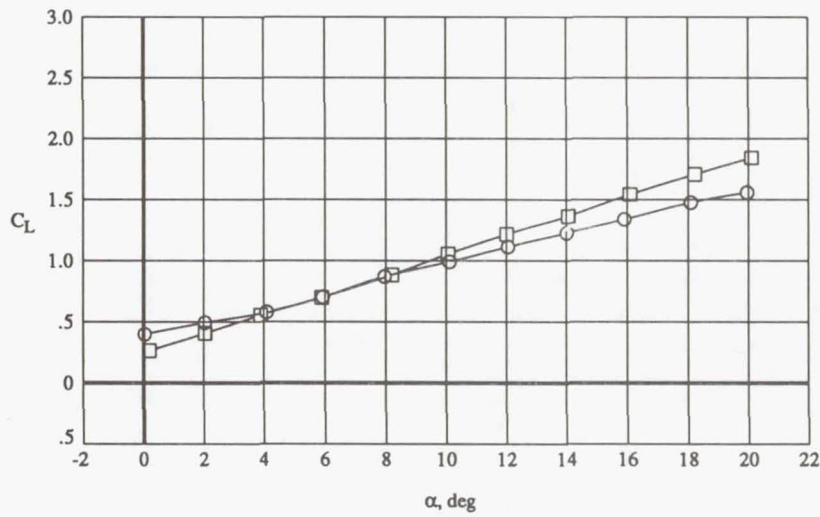
(d)  $\delta_N = 50^\circ L$ .

Figure 18. Continued.

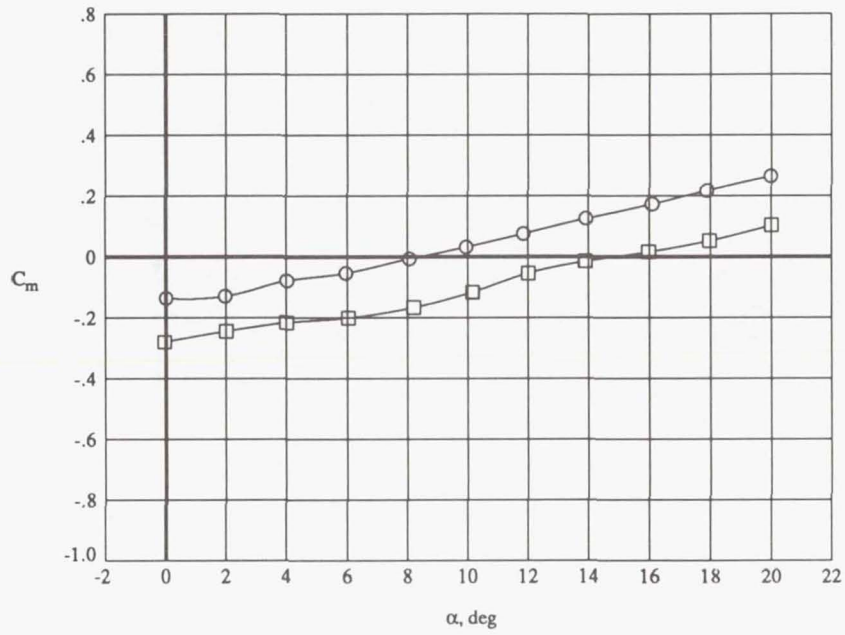


NPR  
 ○ 1.0  
 □ 2.5



(e)  $\delta_N = 0^\circ T$ .

Figure 18. Continued.



NPR

○ 1.0  
 □ 2.5

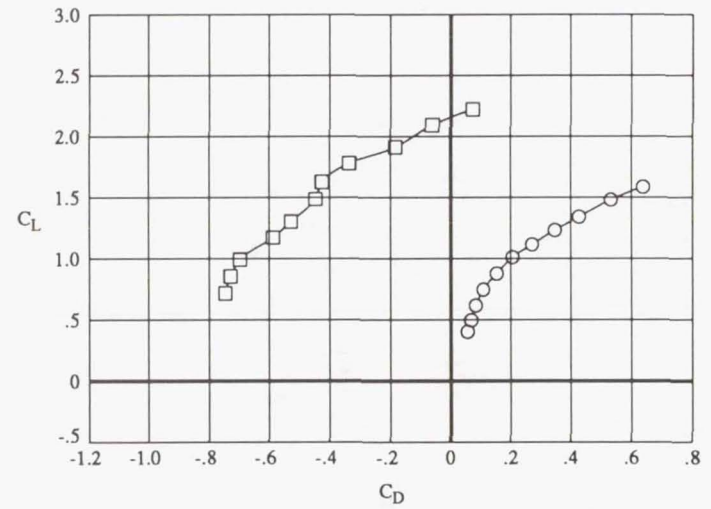
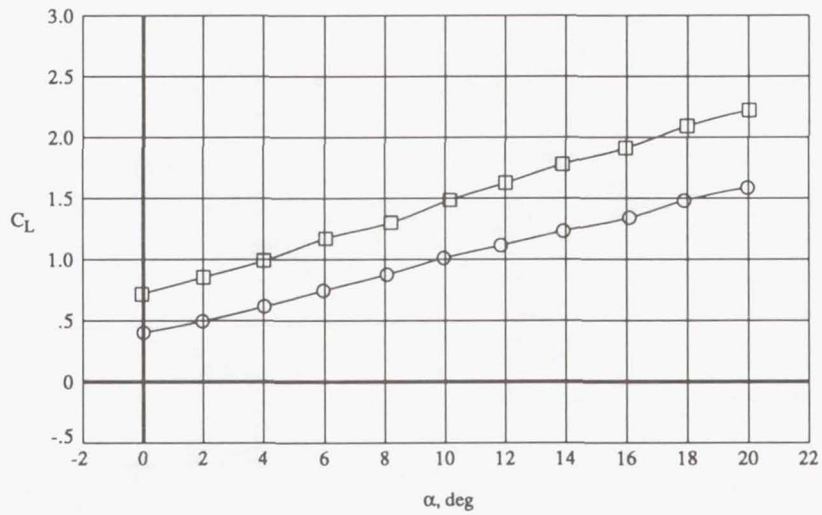
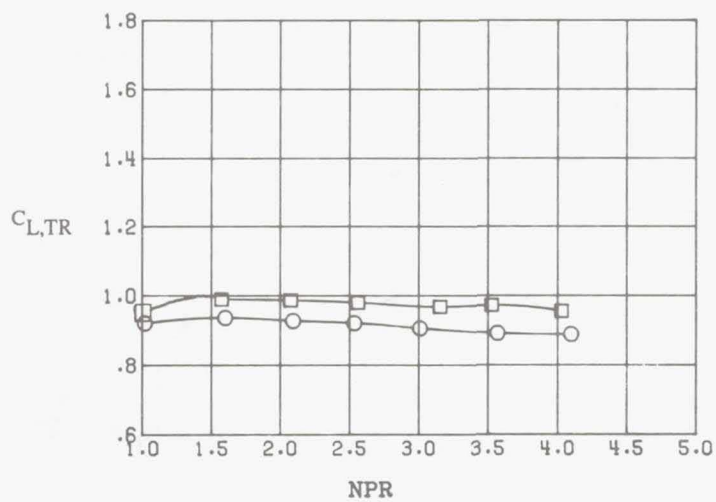
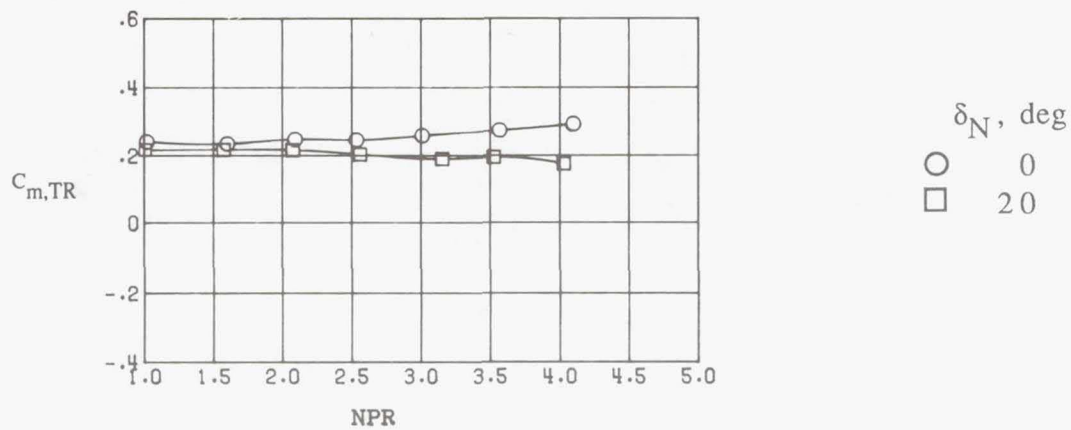
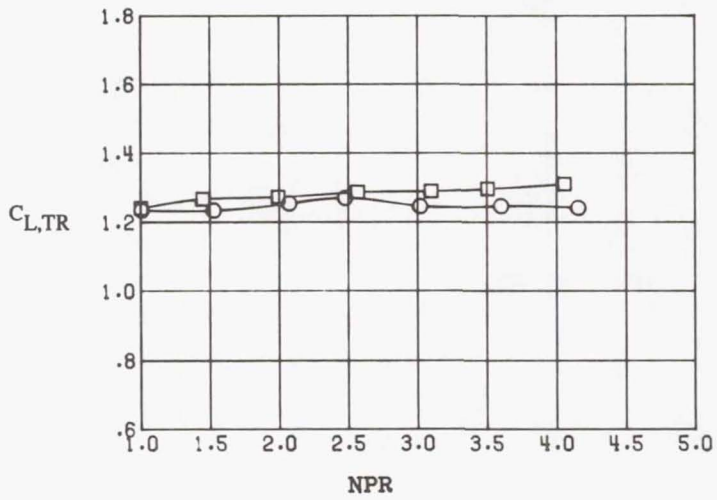
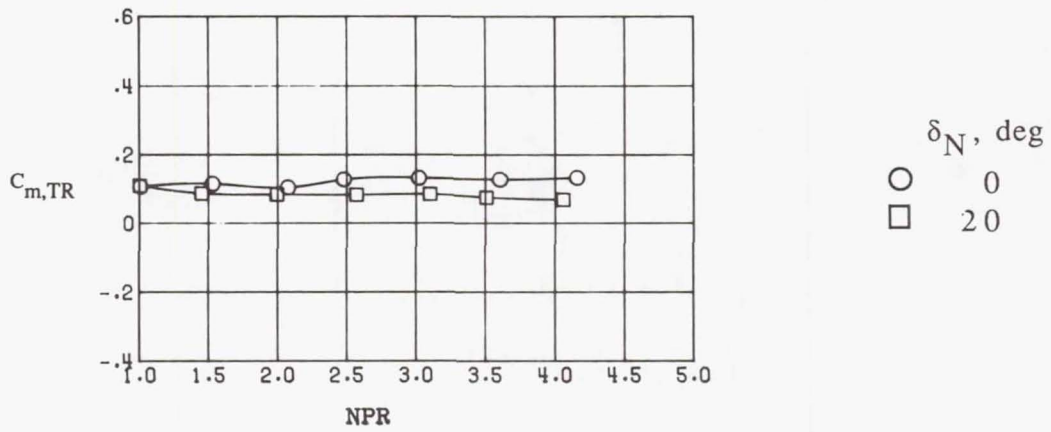
(f)  $\delta_N = 20^\circ T$ .

Figure 18. Concluded.



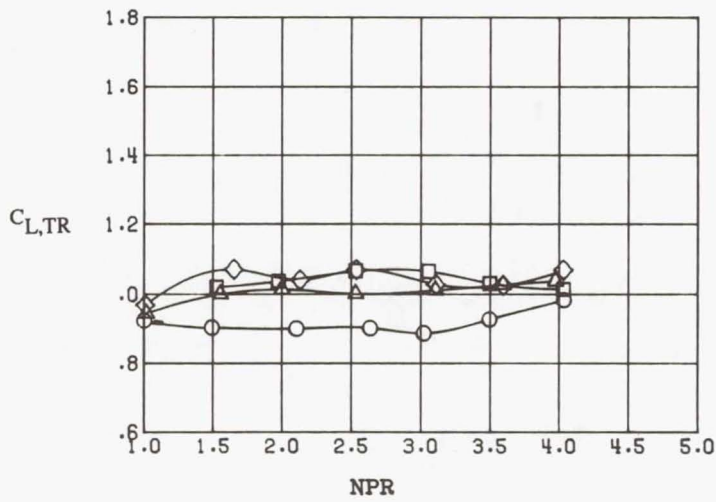
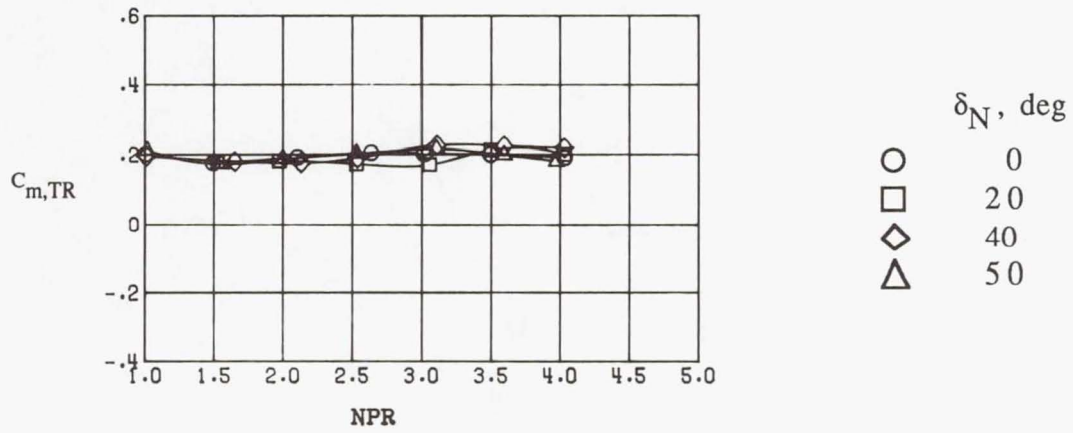
(a)  $\delta_f = 0^\circ$ .

Figure 19. Thrust-removed longitudinal aerodynamic characteristics at  $\alpha = 14^\circ$  for nozzle deflections as a function of NPR for AXI nozzle concept.



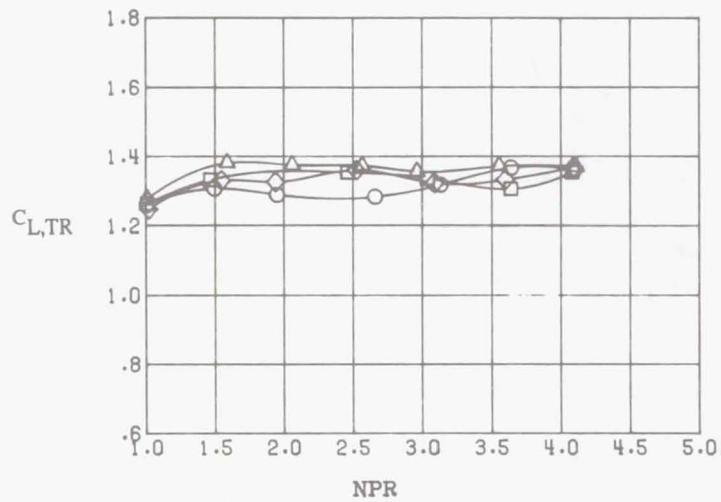
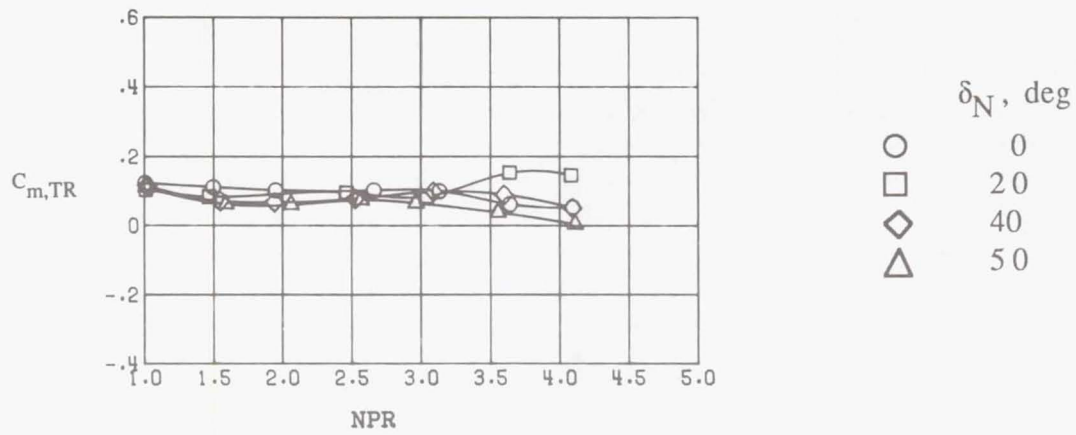
(b)  $\delta_f = 20^\circ$ .

Figure 19. Concluded.



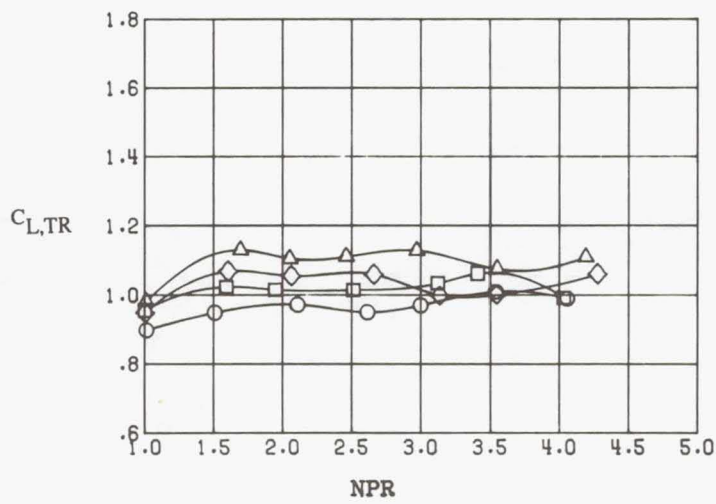
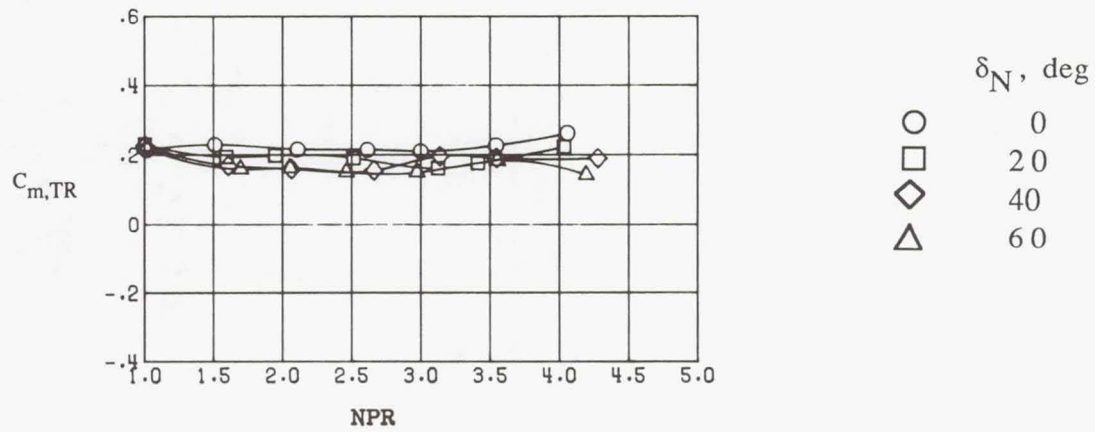
(a)  $\delta_f = 0^\circ$ .

Figure 20. Thrust-removed longitudinal aerodynamic characteristics at  $\alpha = 14^\circ$  for nozzle deflections as a function of NPR for ALBEN concept.



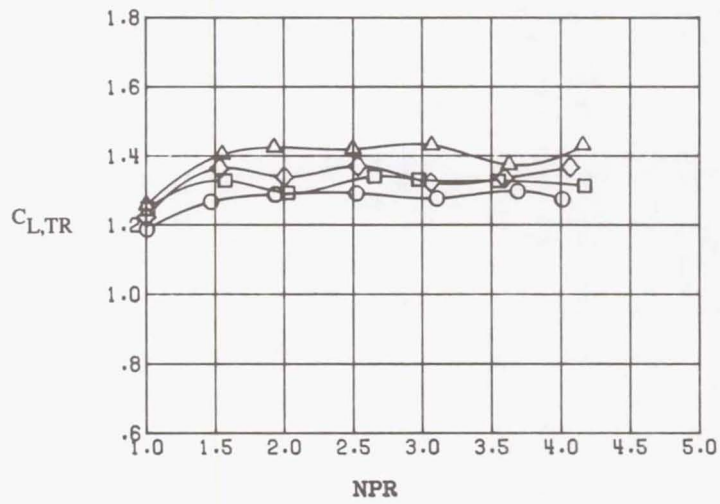
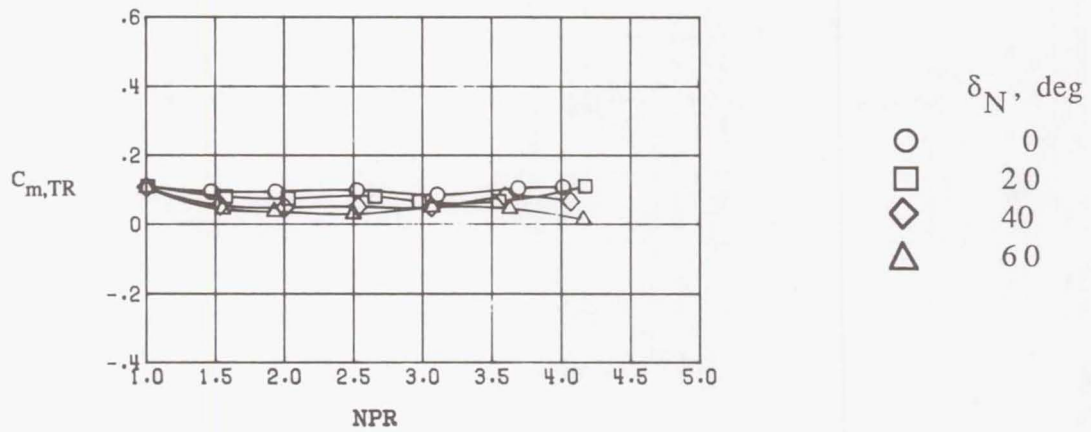
(b)  $\delta_f = 20^\circ$ .

Figure 20. Concluded.



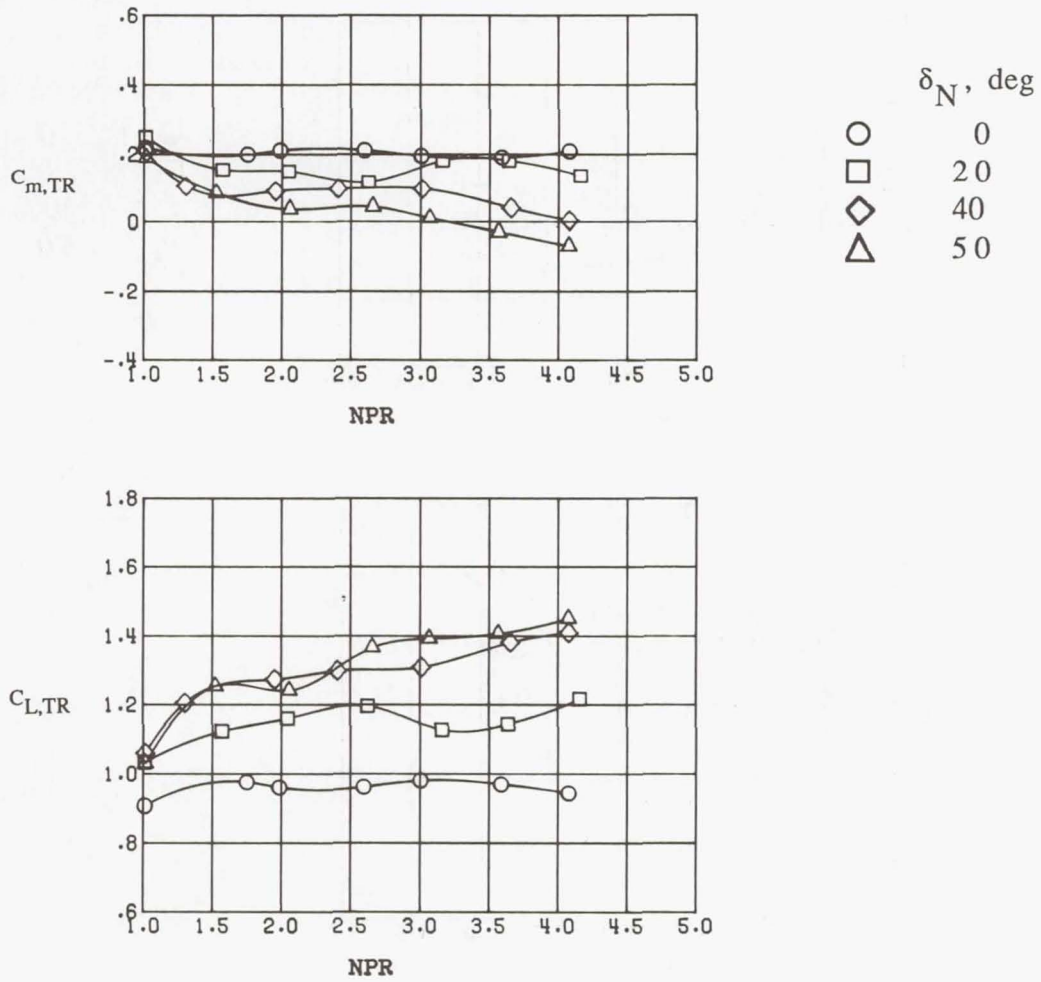
(a)  $\delta_f = 0^\circ$ .

Figure 21. Thrust-removed longitudinal aerodynamic characteristics at  $\alpha = 14^\circ$  for nozzle deflections as a function of NPR for LASERN concept.



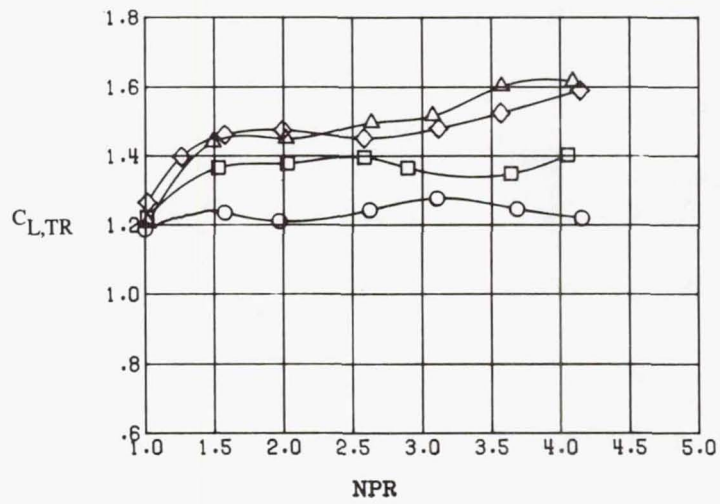
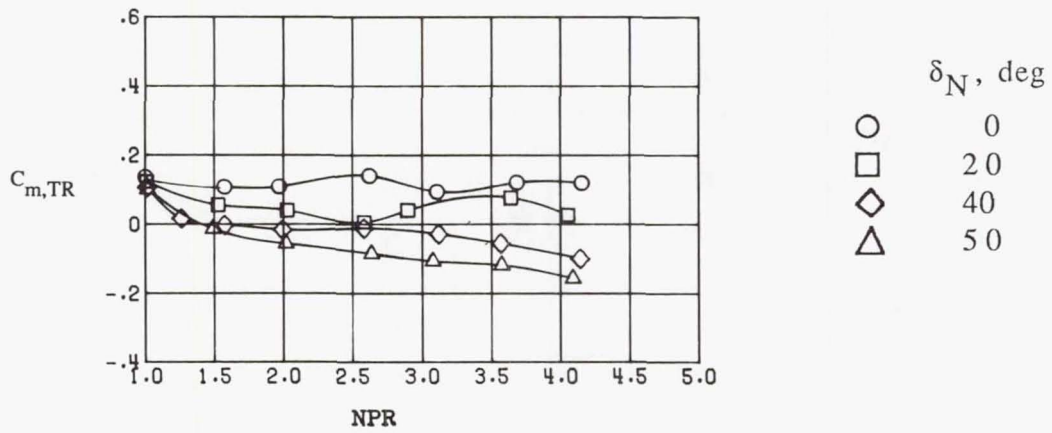
(b)  $\delta_f = 20^\circ$ .

Figure 21. Concluded.



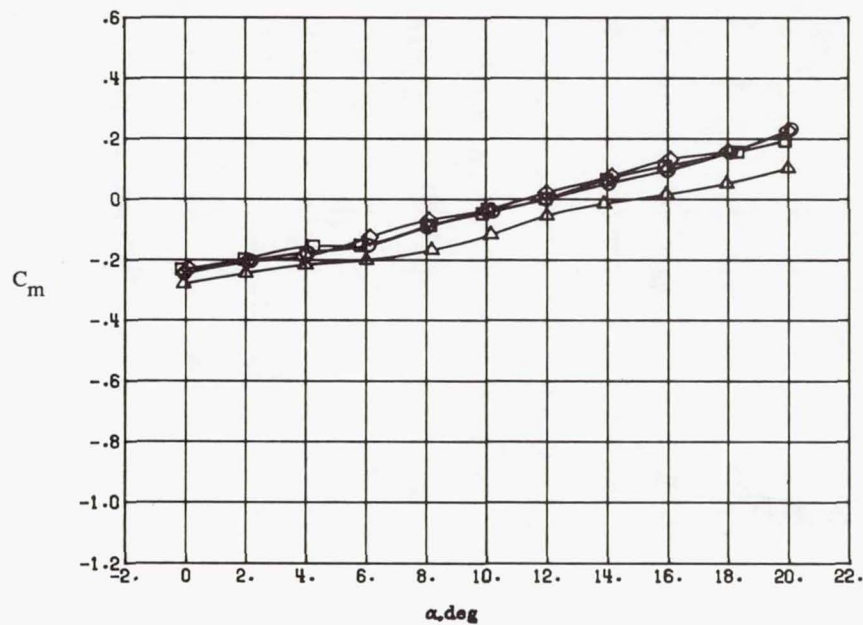
(a)  $\delta_f = 0^\circ$ .

Figure 22. Thrust-removed longitudinal aerodynamic characteristics at  $\alpha = 14^\circ$  for nozzle deflections as a function of NPR for HASERN concept.



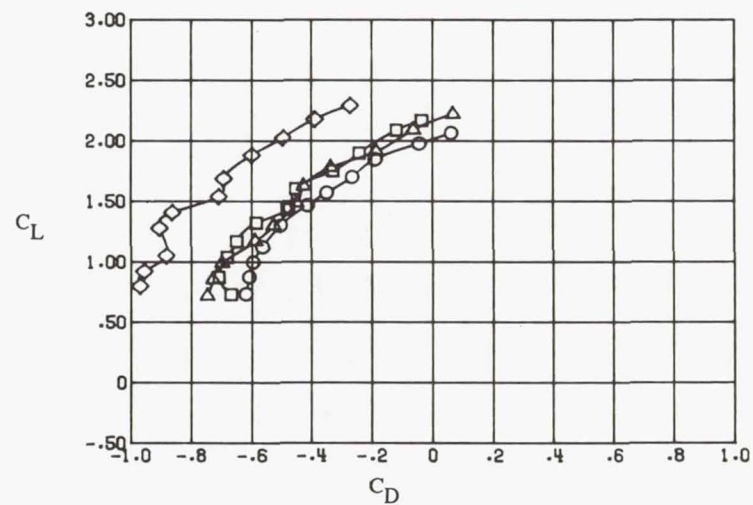
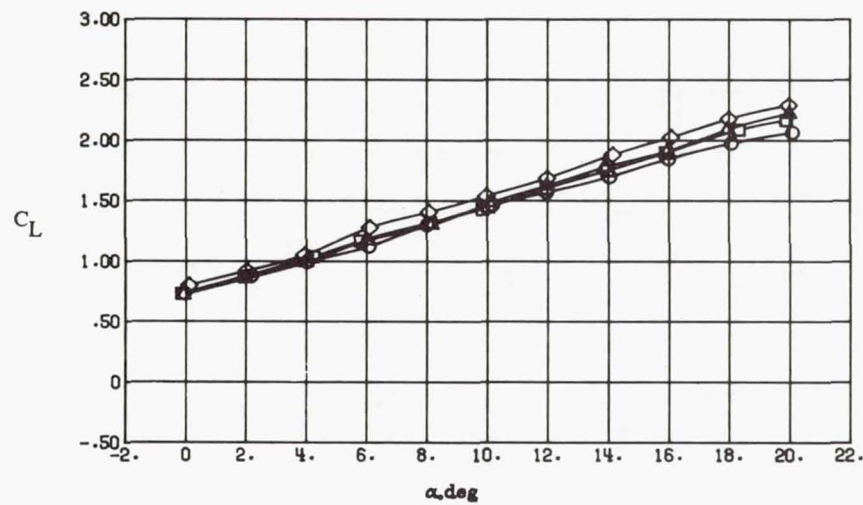
(b)  $\delta_f = 20^\circ$ .

Figure 22. Concluded.



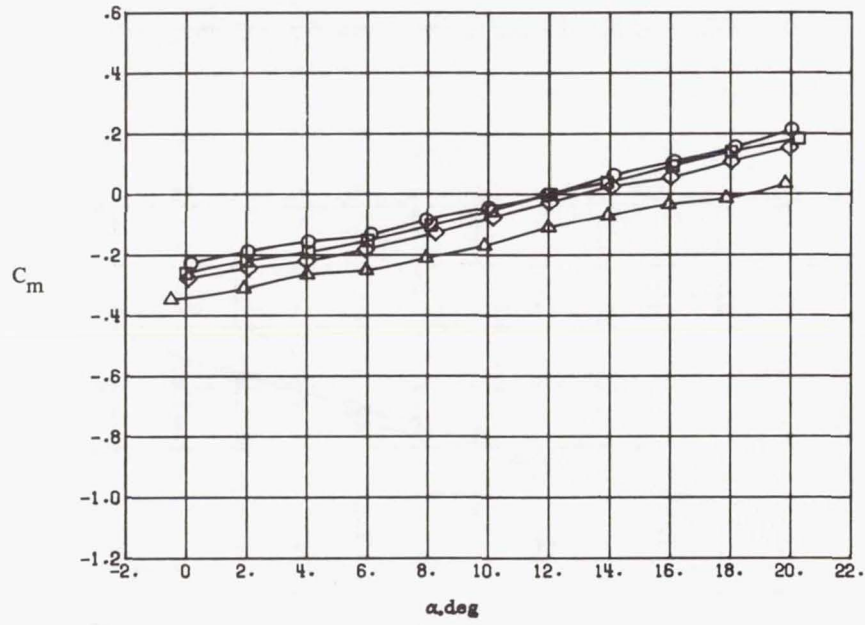
Nozzle Concept

- AXI
- ALBEN
- ◇ LASERN
- △ HASERN



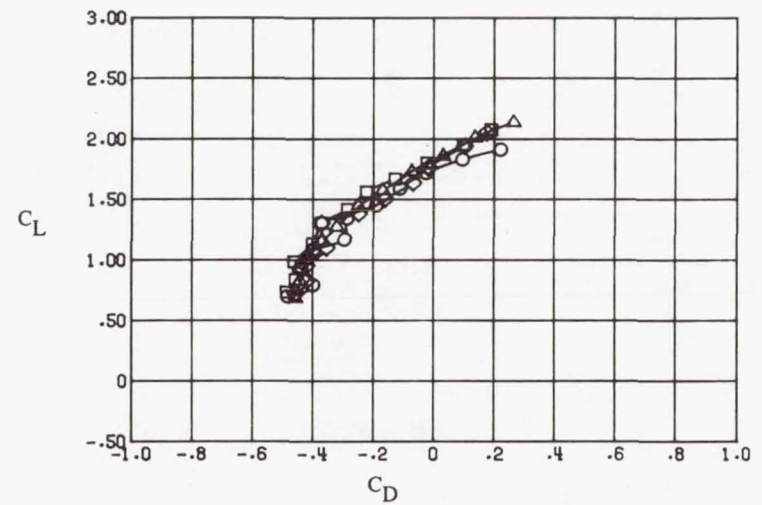
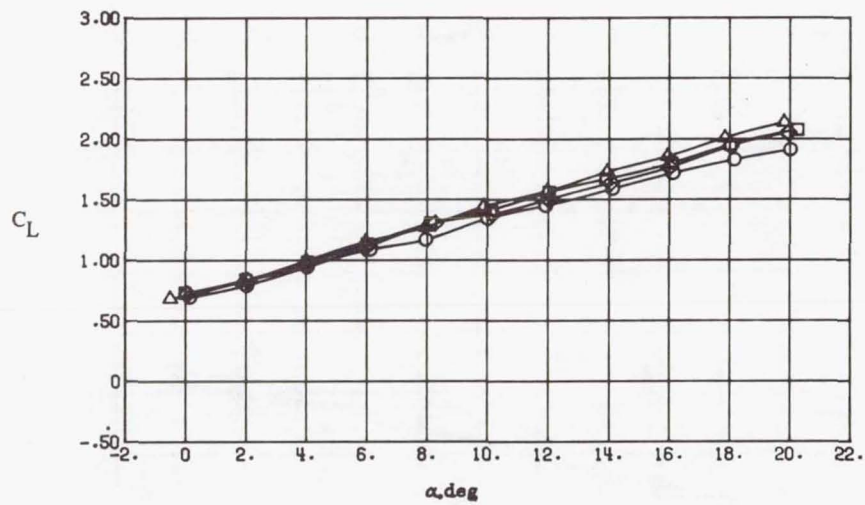
(a) Takeoff power setting.

Figure 23. Effects of nozzle vector concepts on longitudinal aerodynamic characteristics. NPR = 2.5;  $\delta_N = 20^\circ L$ ;  $\delta_f = 20^\circ$ .



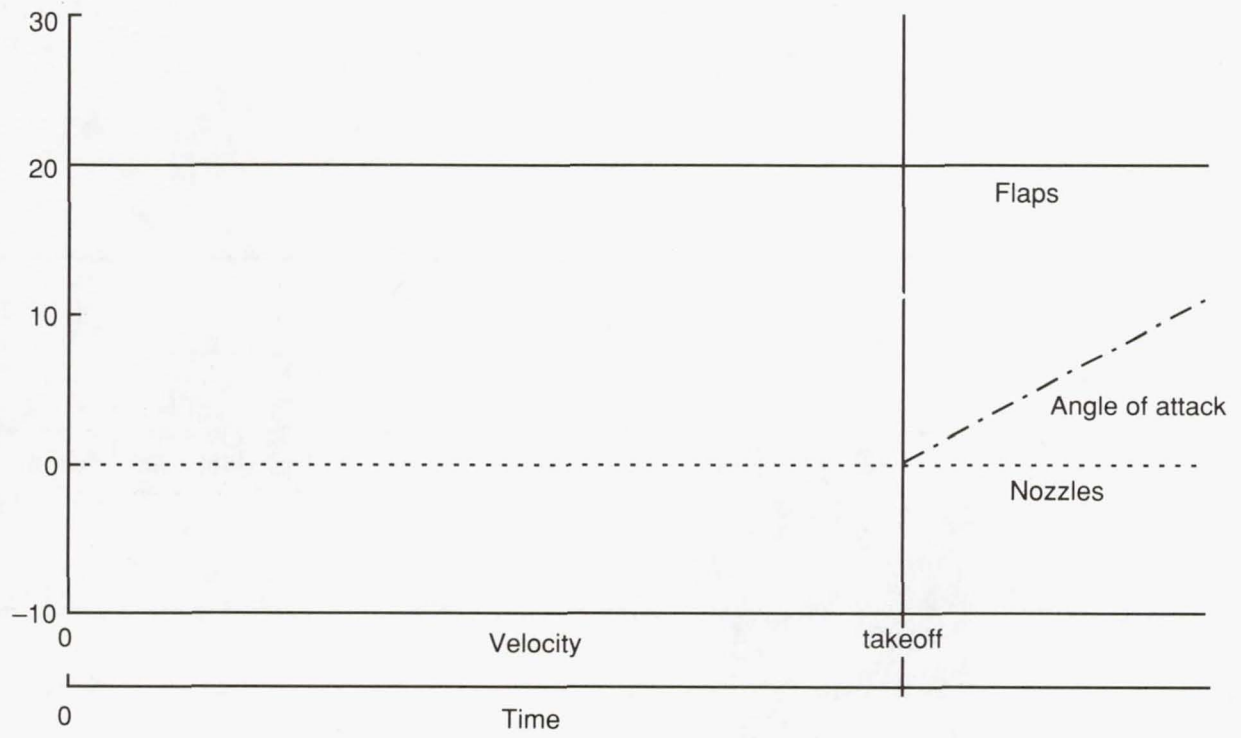
Nozzle Concept

- AXI
- ALBEN
- ◇ LASERN
- △ HASERN

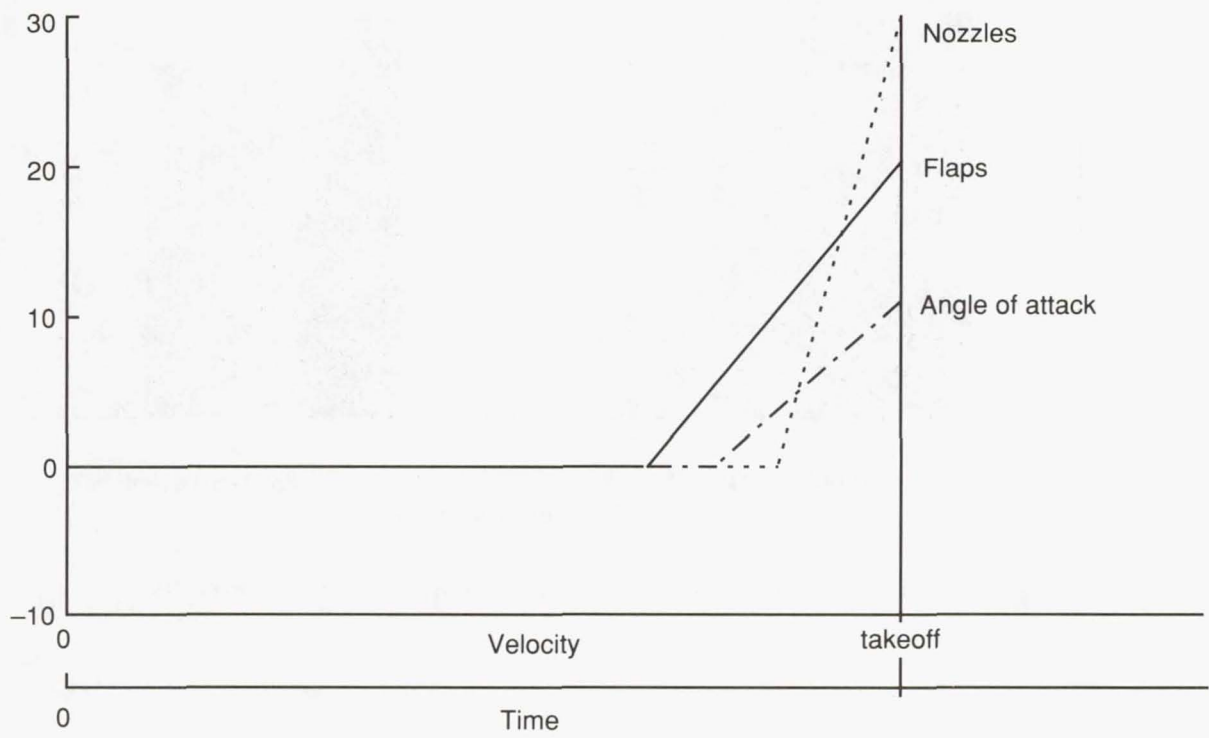


(b) Landing power setting.

Figure 23. Concluded.



(a) Conventional takeoff profile.



(b) Optimized takeoff profile.

Figure 24. Typical profiles for conventional and optimized takeoffs.

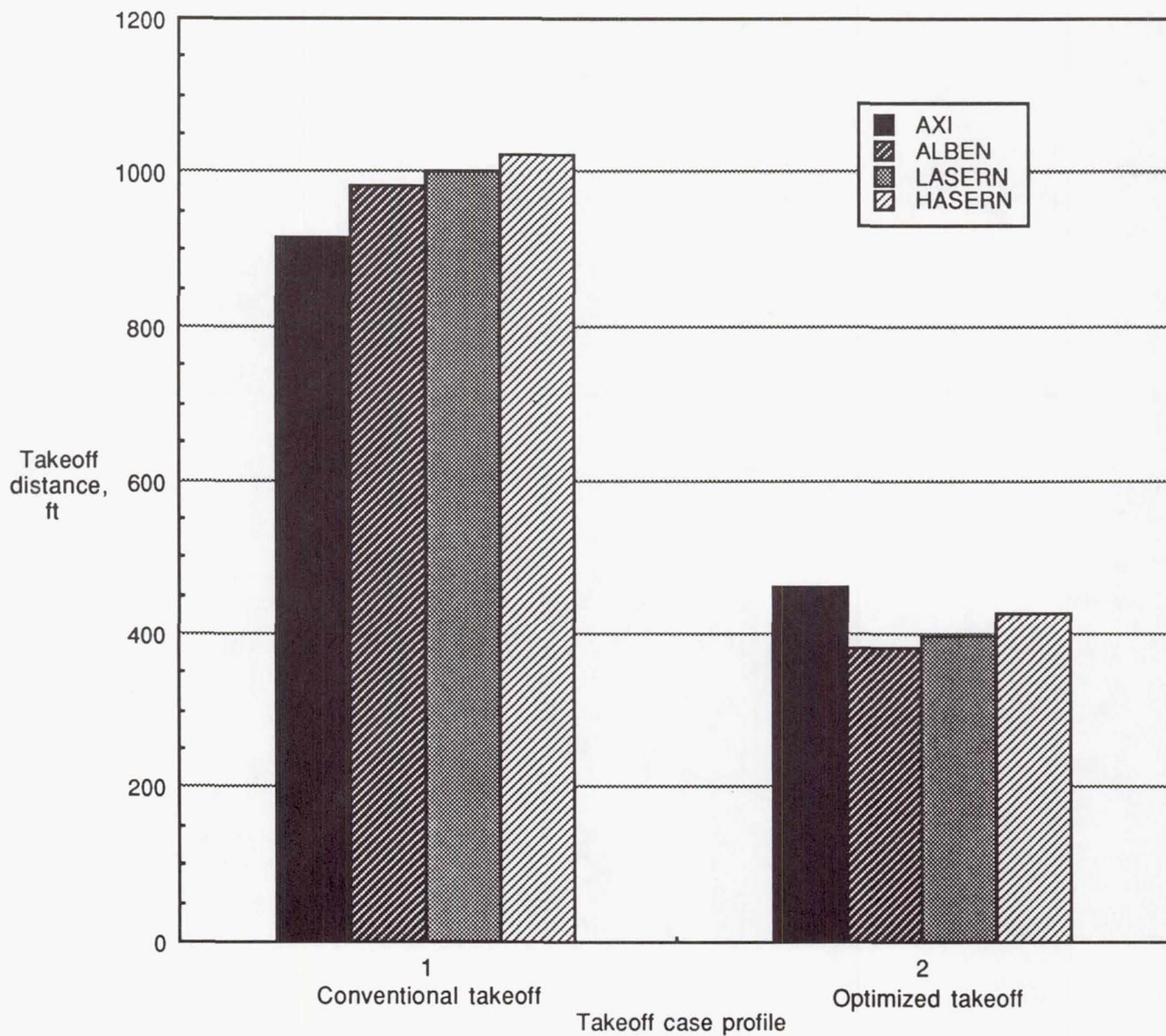


Figure 25. Takeoff distance for four nozzle concepts for 34 200-lb aircraft.

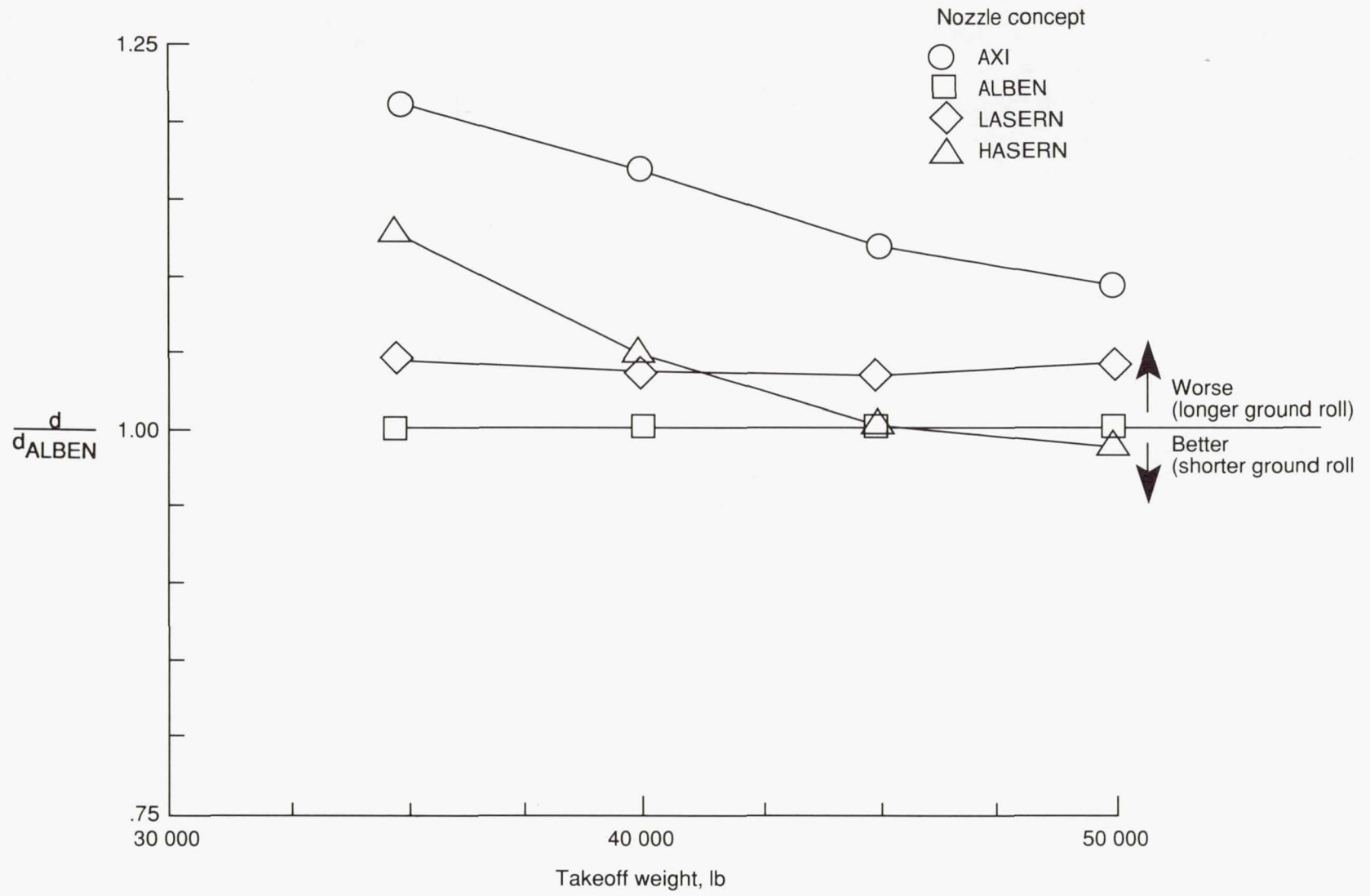
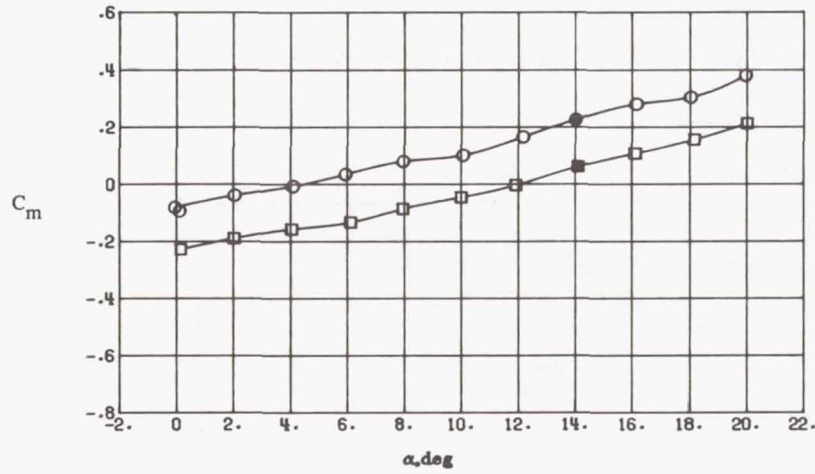


Figure 26. Takeoff distance for optimized profile at overweight conditions with ALBEN concept as reference.



$\delta_N$ , deg  
 ○ 0  
 □ 20

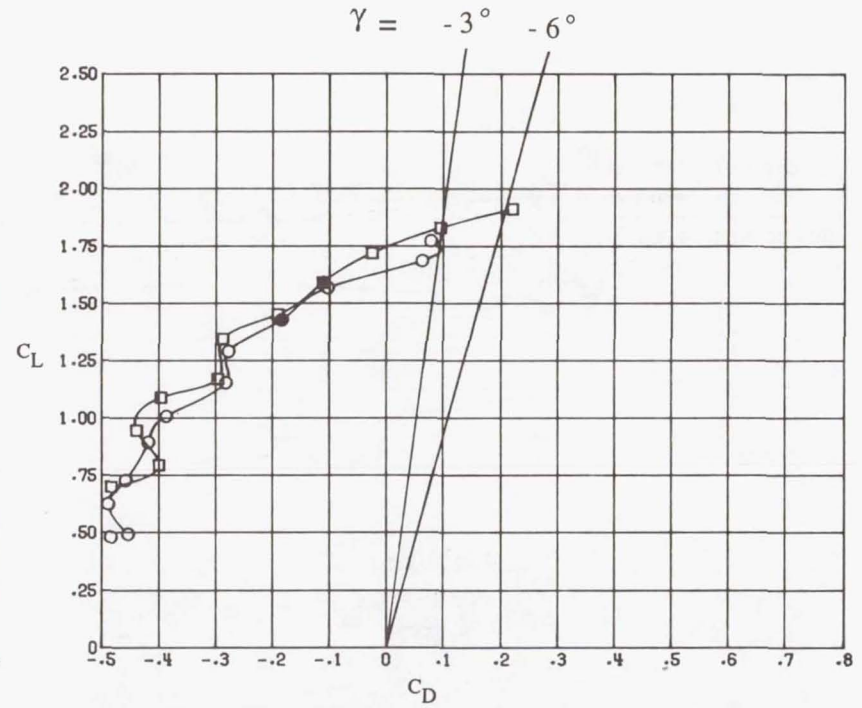
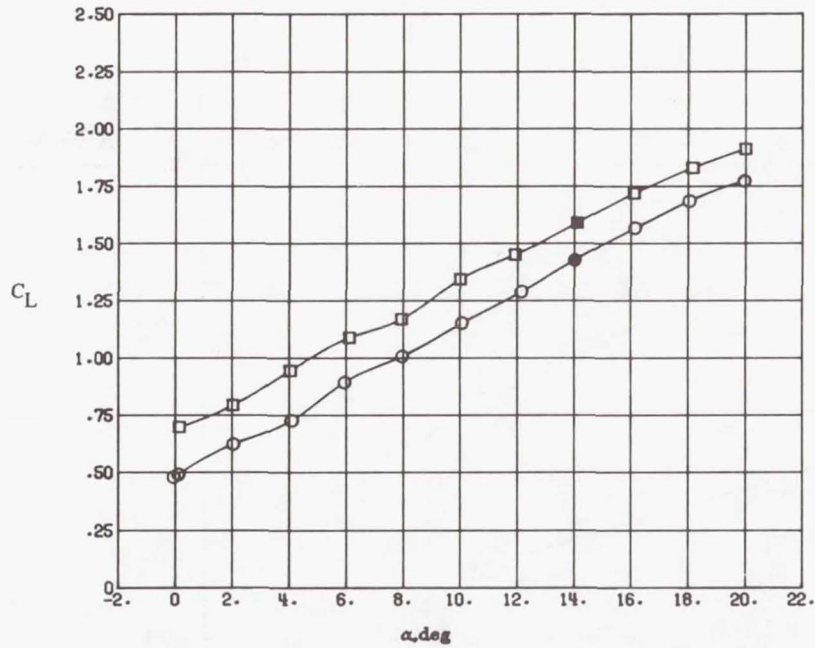


Figure 27. Suitable STOL approach candidates for AXI nozzle concept at  $\delta_f = 20^\circ$ .

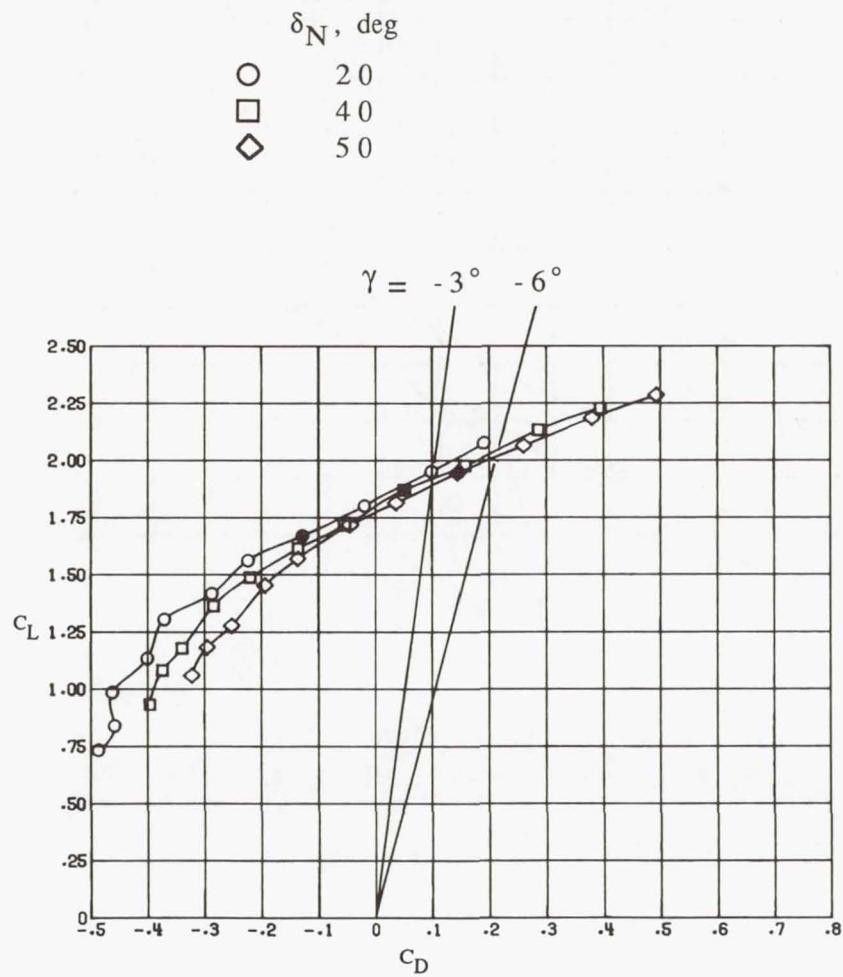
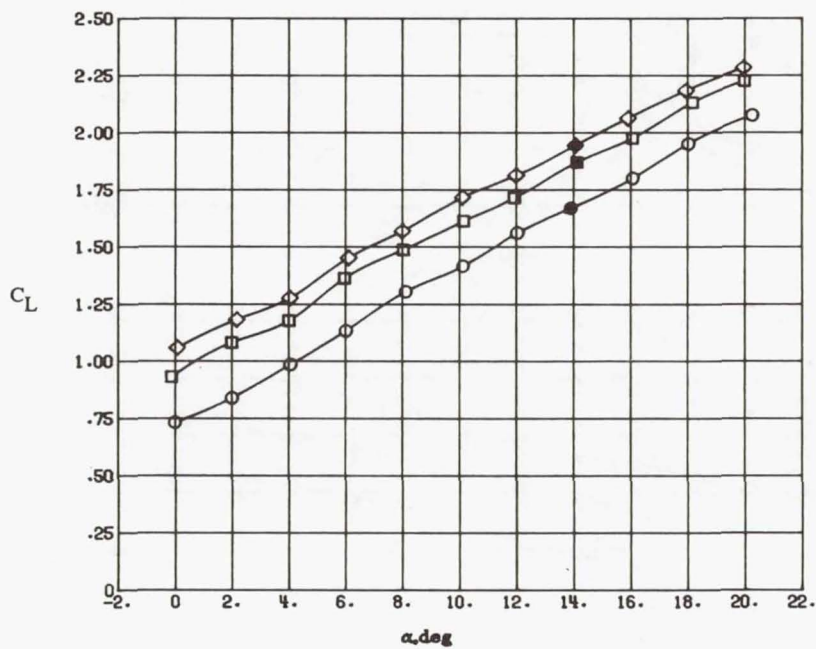
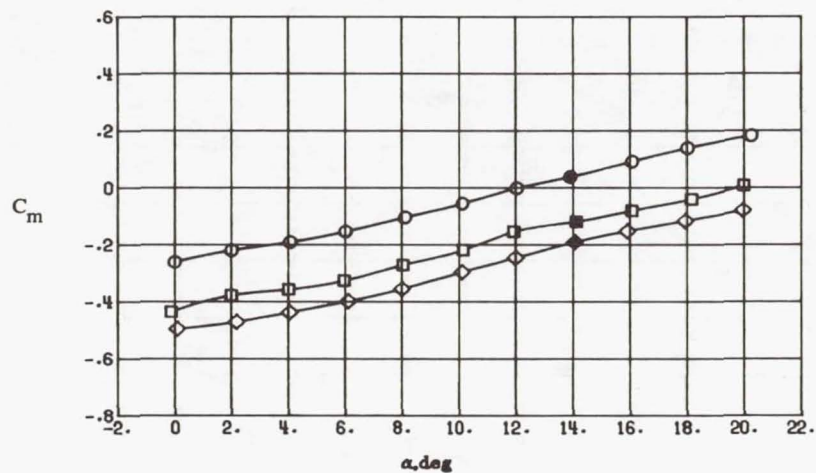
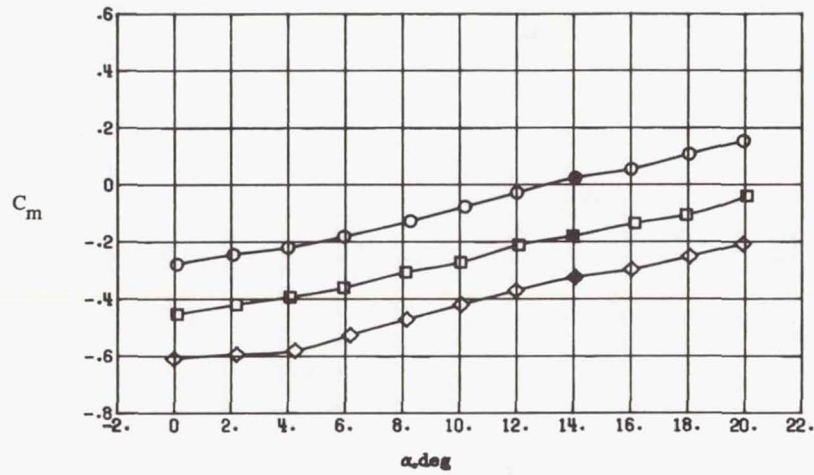


Figure 28. Suitable STOL approach candidates for ALBEN concept at  $\delta_f = 20^\circ$ .



$\delta_N$ , deg

○ 20  
 □ 40  
 ◇ 60

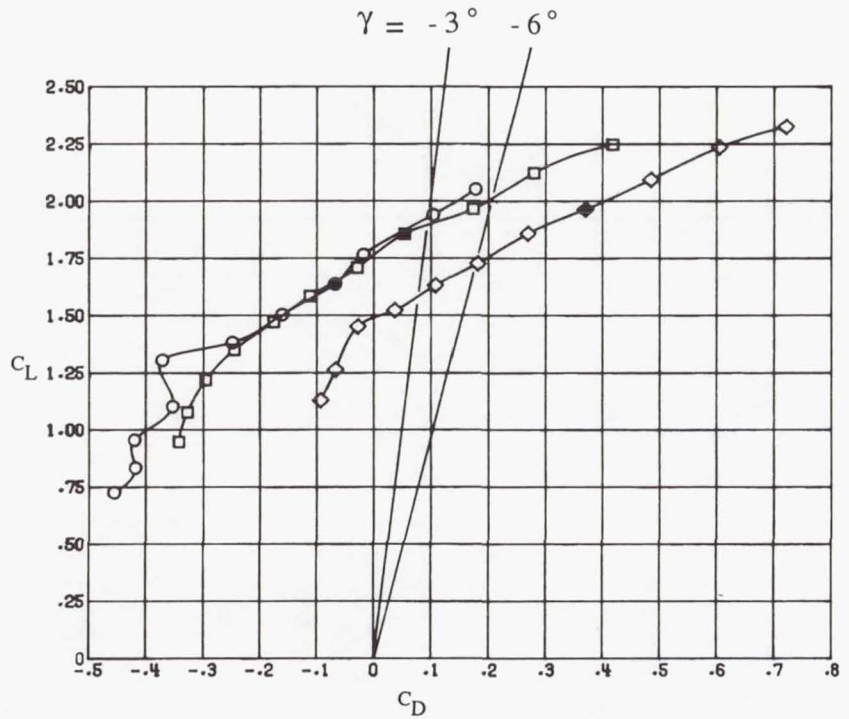
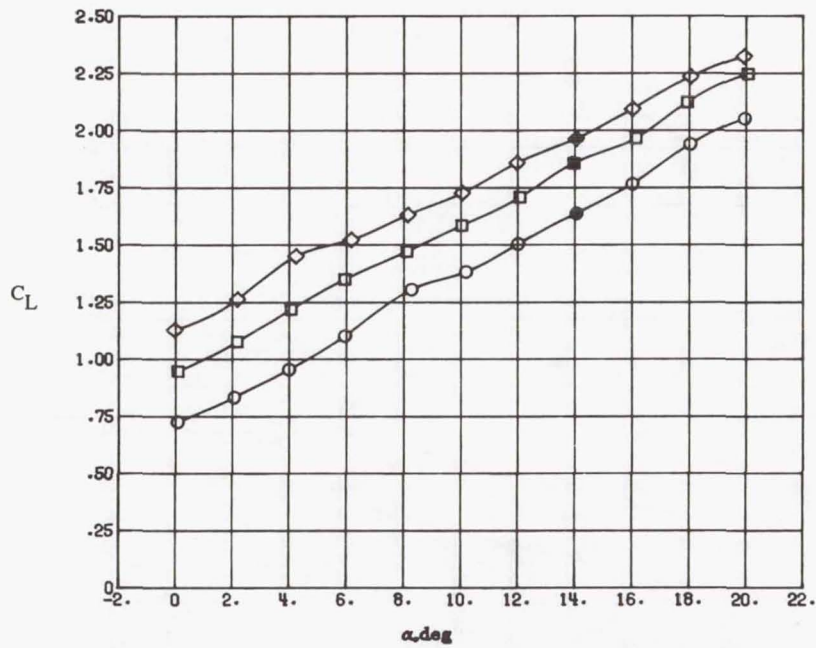
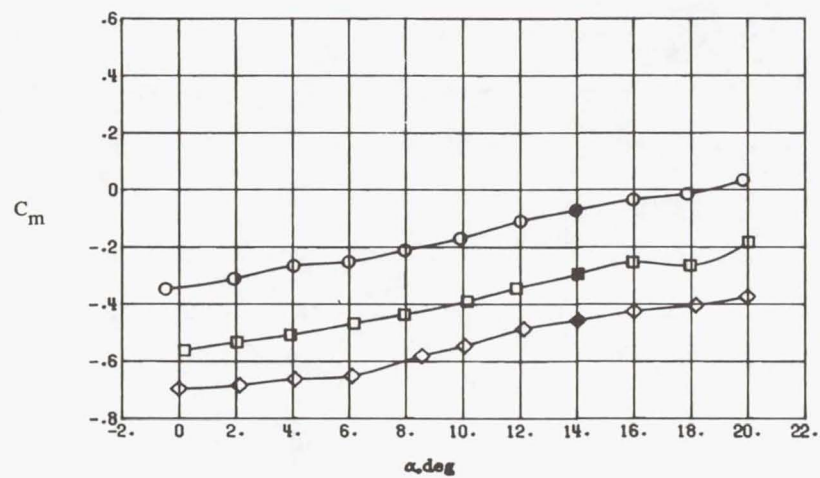


Figure 29. Suitable STOL approach candidates for LASERN concept at  $\delta_f = 20^\circ$ .



$\delta_N$ , deg

- 20
- 40
- ◇ 50

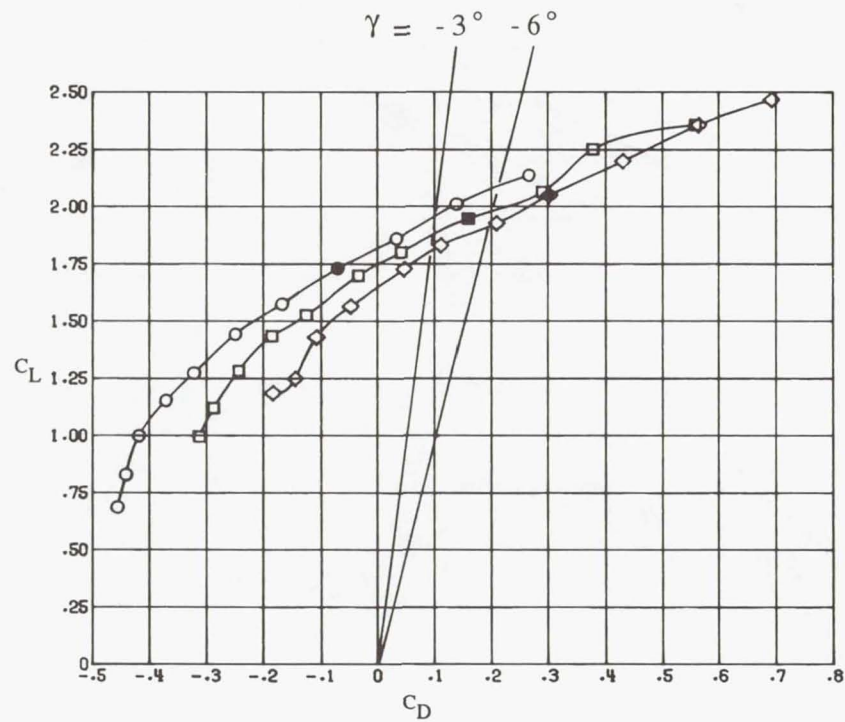
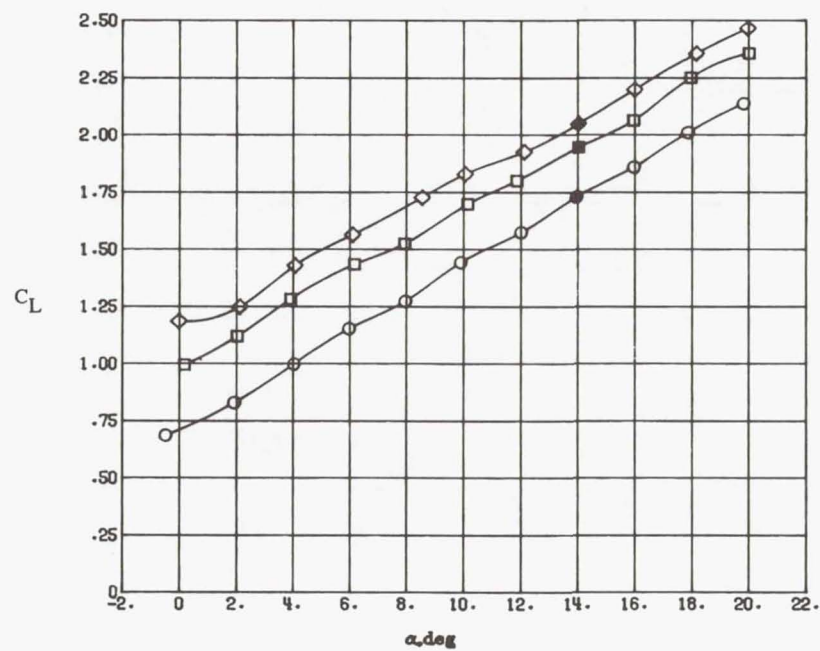
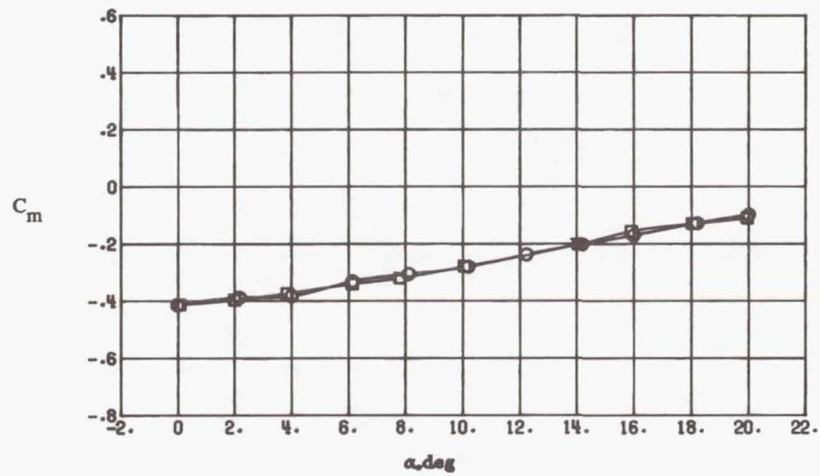


Figure 30. Suitable STOL approach candidates for HASERN concept at  $\delta_f = 20^\circ$ .



Nozzle Concept  $\delta_N$ , deg

○ LASERN	60
□ HASERN	40

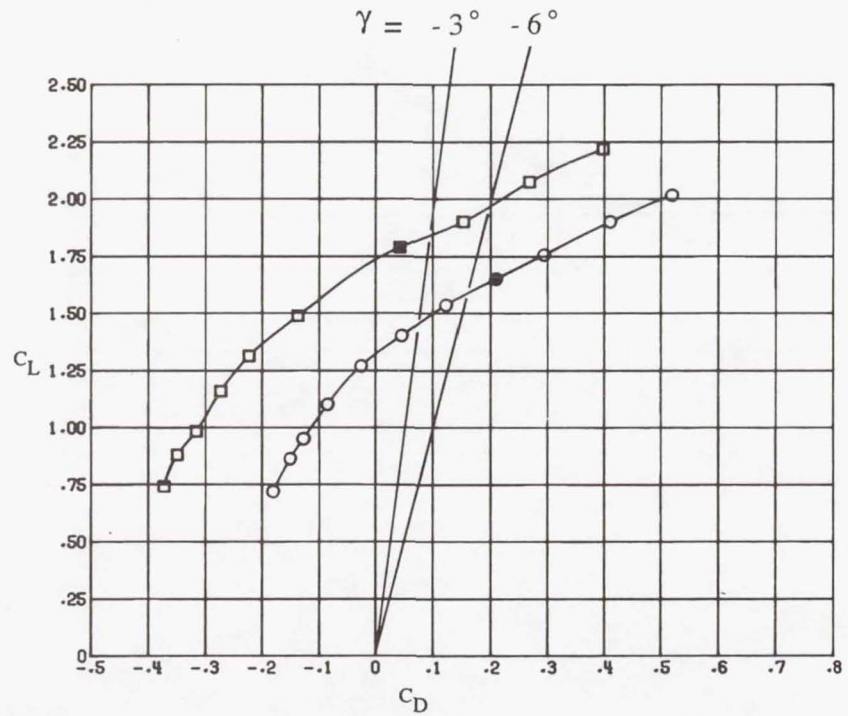
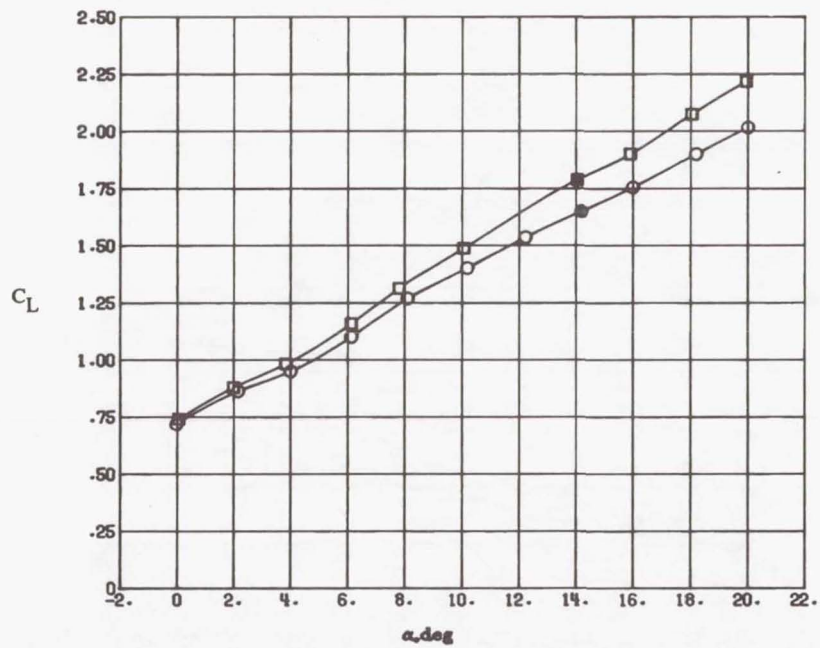
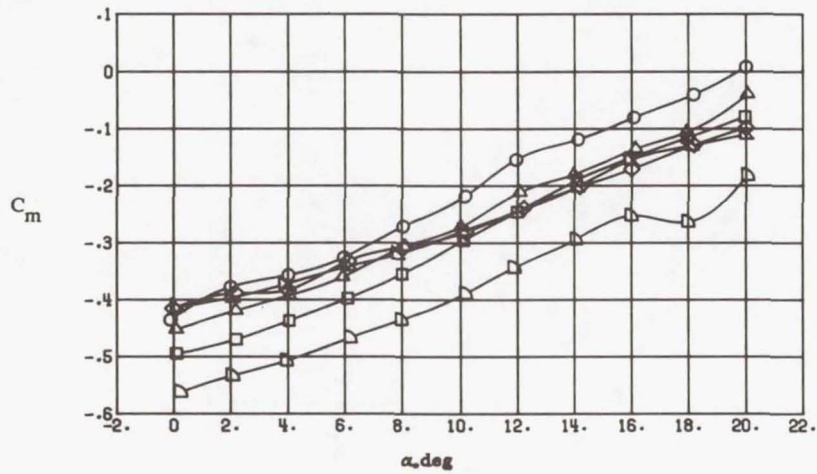


Figure 31. Suitable STOL approach nozzle candidates at  $\delta_f = 0^\circ$ .



	$\delta_N$ , deg	$\delta_f$ , deg	Nozzle Concept
○	40	20	ALBEN
□	50	20	ALBEN
◇	60	0	LASERN
△	40	20	LASERN
▽	40	0	HASERN
▷	40	20	HASERN

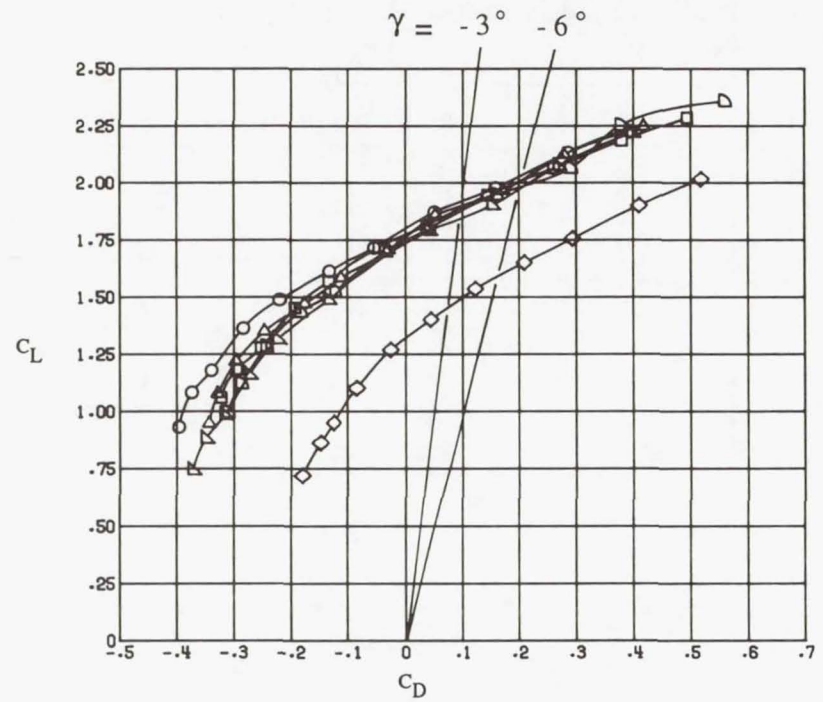
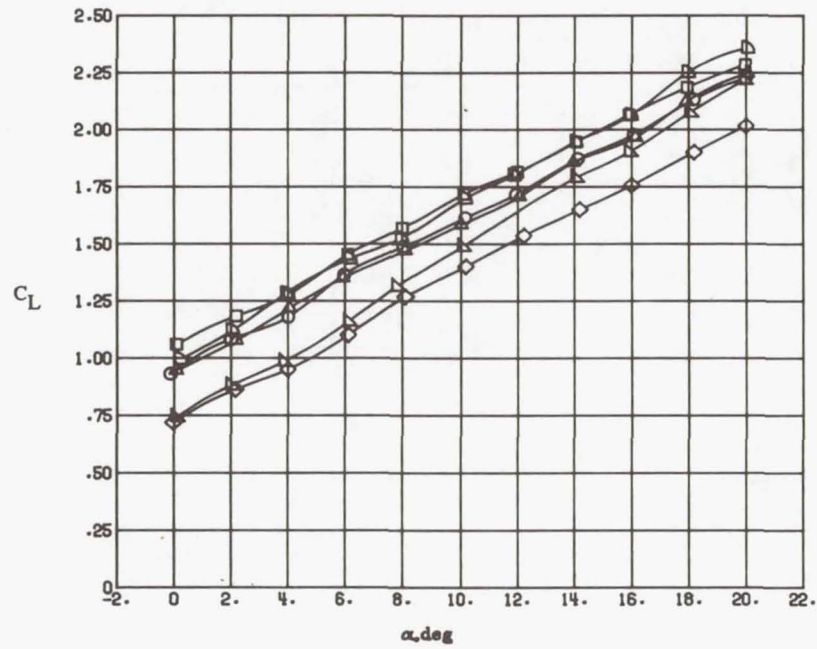


Figure 32. Best STOL approach nozzle candidates.

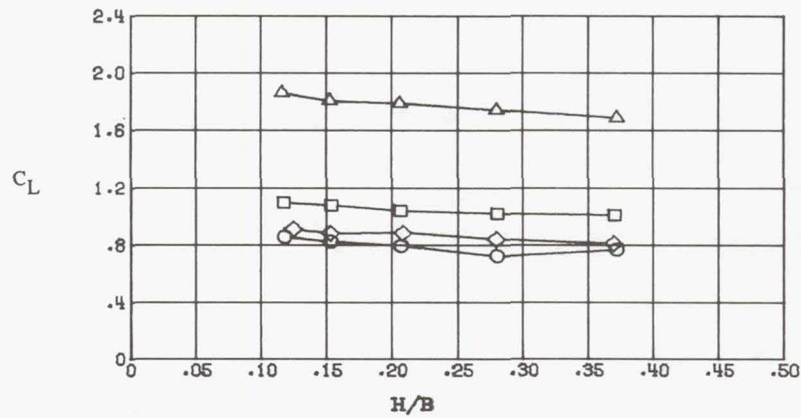
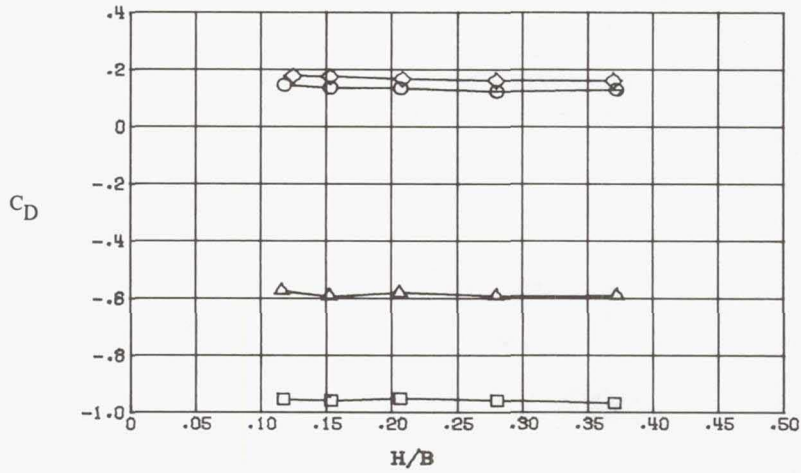
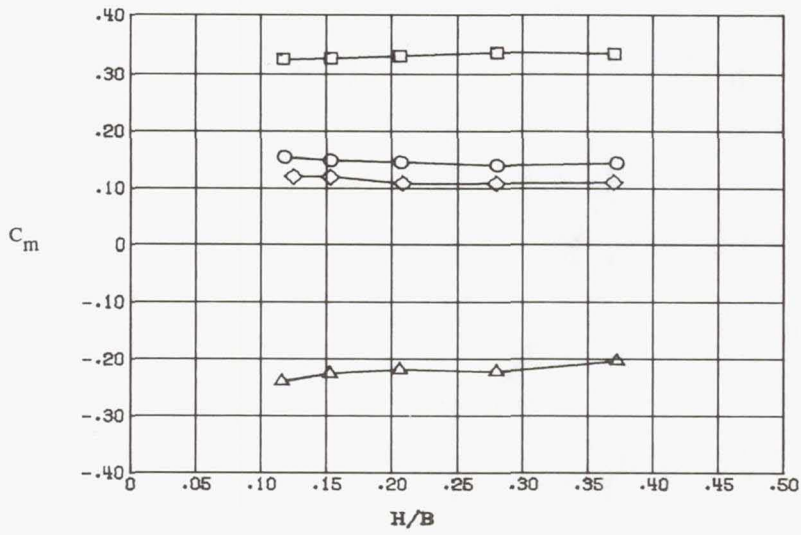


Figure 33. Ground-effect longitudinal aerodynamic characteristics of ALBEN concept at NPR = 1.0 and 3.5;  $\delta_N = 0^\circ$  and  $40^\circ$  at  $\delta_f = 0^\circ$ .

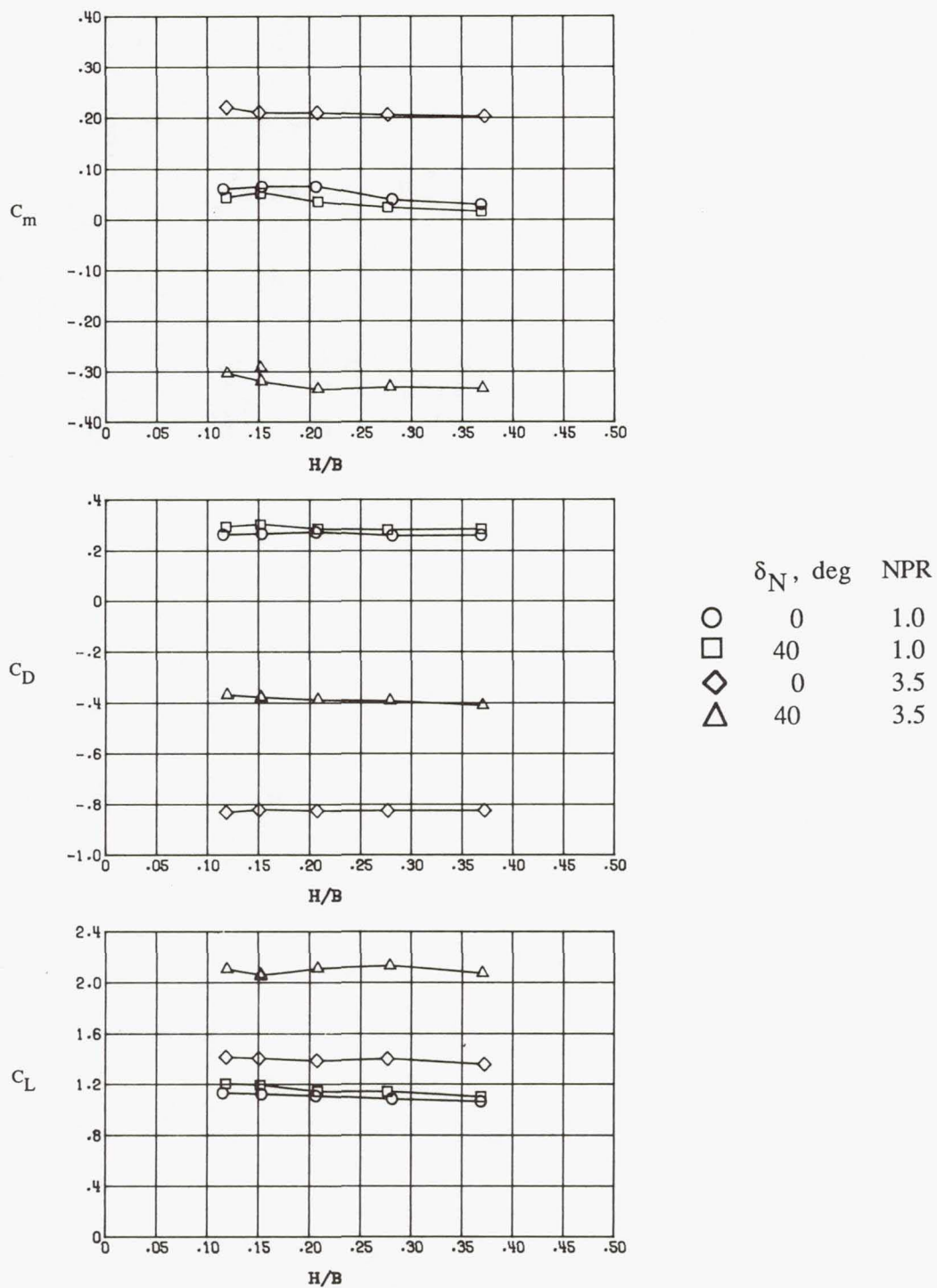


Figure 34. Ground-effect longitudinal aerodynamic characteristics of ALBEN concept at NPR = 1.0 and 3.5;  $\delta_N = 0^\circ L$  and  $40^\circ L$  at  $\delta_f = 20^\circ$ .

REPORT DOCUMENTATION PAGE			Form Approved OMB No. 0704-0188	
Public reporting burden for this collection of information is estimated to average 1 hour per response, including the time for reviewing instructions, searching existing data sources, gathering and maintaining the data needed, and completing and reviewing the collection of information. Send comments regarding this burden estimate or any other aspect of this collection of information, including suggestions for reducing this burden, to Washington Headquarters Services, Directorate for Information Operations and Reports, 1215 Jefferson Davis Highway, Suite 1204, Arlington, VA 22202-4302, and to the Office of Management and Budget, Paperwork Reduction Project (0704-0188), Washington, DC 20503.				
1. AGENCY USE ONLY(Leave blank)	2. REPORT DATE June 1993	3. REPORT TYPE AND DATES COVERED Technical Paper		
4. TITLE AND SUBTITLE Evaluation of Four Advanced Nozzle Concepts for Short Takeoff and Landing Performance			5. FUNDING NUMBERS WU 505-59-30-02	
6. AUTHOR(S) P. Frank Quinto, Guy T. Kemmerly, and John W. Paulson, Jr.				
7. PERFORMING ORGANIZATION NAME(S) AND ADDRESS(ES) NASA Langley Research Center Hampton, VA 23681-0001			8. PERFORMING ORGANIZATION REPORT NUMBER L-16998	
9. SPONSORING/MONITORING AGENCY NAME(S) AND ADDRESS(ES) National Aeronautics and Space Administration Washington, DC 20546-0001			10. SPONSORING/MONITORING AGENCY REPORT NUMBER NASA TP-3314	
11. SUPPLEMENTARY NOTES				
12a. DISTRIBUTION/AVAILABILITY STATEMENT Unclassified-Unlimited Subject Category 02			12b. DISTRIBUTION CODE	
13. ABSTRACT (Maximum 200 words) Four advanced nozzle concepts were tested on a canard-wing fighter in the Langley 14- by 22-Foot Subsonic Tunnel. The four vectoring-nozzle concepts were (1) an axisymmetric nozzle (AXI), (2) an asymmetric, load-balanced exhaust nozzle (ALBEN), (3) a low aspect ratio, single expansion ramp nozzle (LASERN), and (4) a high aspect ratio, single expansion ramp nozzle (HASERN). The investigation was conducted to determine the most suitable nozzle concept for short takeoff and landing (STOL) performance. The criterion for the best STOL performance was a takeoff ground roll of less than 1000 ft. At approach, the criteria were high lift and sufficient drag to maintain a glide slope of $-3^\circ$ to $-6^\circ$ with enough pitching-moment control from the canards. The test was performed at a dynamic pressure of 45 lb/ft <sup>2</sup> and an angle-of-attack range of $0^\circ$ to $20^\circ$ . The nozzle pressure ratio was varied from 1.0 to 4.3 at both dry power and afterburning nozzle configurations with nozzle vectoring to $60^\circ$ . In addition, the model was tested in and out of ground effects. The ALBEN concept was the best of the four nozzle concepts tested for STOL performance.				
14. SUBJECT TERMS Thrust vectoring; Short takeoff and landing (STOL) aircraft; Approach; Takeoff			15. NUMBER OF PAGES 96	
			16. PRICE CODE A05	
17. SECURITY CLASSIFICATION OF REPORT Unclassified	18. SECURITY CLASSIFICATION OF THIS PAGE Unclassified	19. SECURITY CLASSIFICATION OF ABSTRACT	20. LIMITATION OF ABSTRACT	